Development of advanced Transmission Electron Microscopy techniques for nanoscale mapping

Raghda Makarem

To cite this version:

Raghda Makarem. Development of advanced Transmission Electron Microscopy techniques for nanoscale mapping. Physics [physics]. Université Paul Sabatier - Toulouse III, 2019. English. NNT : 2019TOU30304 . tel-03123974

HAL Id: tel-03123974
https://theses.hal.science/tel-03123974

Submitted on 28 Jan 2021

THÈSE

En vue de l’obtention du

DOCTORAT DE L’UNIVERSITÉ DE TOULOUSE

Délivré par l'Université Toulouse 3 - Paul Sabatier

Présentée et soutenue par

Raghda MAKAREM

Le 21 novembre 2019

Développement de techniques avancées de Microscopie Electronique à Transmission pour la cartographie à l'échelle nanométrique.

Ecole doctorale : **SDM - SCIENCES DE LA MATIERE - Toulouse**

Spécialité : **Nanophysique**

Unité de recherche :
LPCNO-IRSAMC - Laboratoire de Physique et Chimie des Nano-Objets

Thèse dirigée par
Pier Francesco FAZZINI et Marc RESPAUD

Jury
Mme Marie-France BEAUFORT, Rapporteure
M. Alain PORTAVOCE, Rapporteur
Mme Caroline BONAFOS, Examinatrice
M. Etienne TALBOT, Examinateur
M. Fuccio CRISTIANO, Examinateur
M. Pier Francesco FAZZINI, Directeur de thèse

Contents

Acronyms

ALD	Atomic Layer Deposition
BF	Bright Field
BF-STEM	Bright Field STEM
BSE	Back-scattered Electrons
C-L	Cliff-Lorimer
EBID	Electron Beam-Induced Deposition
ECs	Electrochemical Capacitors
EDX	Energy Dispersive X-ray
EELS	Electron Energy Loss Spectroscopy
ESS	Energy Storage Sources
FEG	Field Emission Gun
FFT	Fast Fourier Transform
FIB	Focused Ion Beam
FWHM	Full Width at Half Maximum
GO	Graphite Oxide
HAADF	High Angle Annular Dark Field Detector
HRTEM	High Resolution Transmission Electron Microscopy
IAS	Ideal Amorphous Solids
IBID	Ion Beam-Induced Deposition
ICs	Integrated Circuits
IoT	Internet of Things

LIG	Laser-Induced Graphene
LSG	Laser-Scribed Graphene
MOSFET	Metal-Oxide-Semiconductor Field-Effect Transistor
NLA	Ultra Violet Nanosecond Laser Annealing
PCVD	Pressure Chemical Vapor Deposition
PI	Polyimide
RBS	Rutherford backscattering spectroscopy
RTP	Rapid Thermal Processes
SDD	Silicon Drift Detector
SE	Secondary Electrons
SEM	Scanning Electron Microscope
SIMS	Secondary Ion Mass Spectroscopy
SNR	Signal To Noise Ratio
SOI	Silicon On Insulator
SRIM	Stopping and Range of Ions in Matter
STEM	Scanning Transmission Electron Microscope
TEM	Transmission Electron Microscope
THF	Tetrahydrofurane
TRR	Time-Resolved Reflectivity

Introduction

Since the invention of the semiconductor bipolar transistor by William Shockley, Walter Brattain, and John Bardeen in 1947, followed by that of the unipolar Metal-Oxide-Semiconductor Field-Effect Transistor (MOSFET) by Atalla and Kahng in 1959, the microelectronic industry has revolutionized our society thanks to the continuous production of innovative and evermore performant applications with a direct impact on our everyday's life. Indeed, thanks to its much lower power consumption and higher density than bipolar junction transistors, MOSFET has made it possible to build high-density integrated circuits (ICs) allowing the integration of a continuously increasing number of transistors in a single PC (from few thousands in the 1970s to more than one billion in today's microprocessors). Today, semiconductor-based Integrated Circuits (ICs) are present in a large amount of applications: data processing (personal computers, laptops, servers and tablets), communications (mobile phones, smartphones…), consumer electronics (television sets, music players, gaming consoles…), automotive, industrial (transport…), military in addition to spatial and medical applications. Besides, a further step in the electronics revolution is expected with the development of the Internet of Things (IoT), where a new range of low-power devices will be able to directly interact and communicate through the internet.

In all cases, in order to answer miniaturization and diversification challenges, the physical properties of the materials being used in nowadays devices must be known and controlled at the nanometre scale, calling for the development of more and more sophisticated characterization techniques. For instance, one of the key issues for the miniaturization of 3D semiconductor nanodevices is the precise control of their doping which determines the device electrical properties. Today, the spatial distribution of the doping concentration must be controlled with a precision higher than 1 nm while atomic concentrations below 1 at.% have to be measured. Moreover, the electrical properties can also be improved by modifying the material structure as in the case of SiGe alloys, which combine the advantages of Germanium (high carrier mobility) with those of Silicon (high-quality Si oxide insulator). Again, the precise control of the alloy stoichiometry is crucial for the successful implementation of this material.

Several characterization techniques exist for the measurement of both dopant concentration and alloy stoichiometry. Over the years, Secondary Ion Mass Spectroscopy (SIMS) has established as the most reliable technique. It is based on the sputtering of the sample surface with a focused primary ion beam and the concomitant collection and analysis of the ejected secondary ions. The mass/charge ratios of these secondary ions are measured with a mass spectrometer to determine the elemental, isotopic, or molecular composition. One of the main advantages of SIMS is its particularly low detection limit (which is around 1 x10^{14} atoms/cm3 for most impurity elements in Silicon). However, the SIMS quantification technique is relevant only on one-dimensional devices and requires large analysis areas (~30 m x 30 m) to achieve significant result. For this reason, alternative techniques must be developed to ensure the localized measurements in the most advanced 2D and 3D devices being developed in the semiconductor industry.

The work presented in this thesis is based on the use of Scanning Transmission Electron Microscopy (STEM) associated with Energy Dispersive X-ray spectroscopy (EDX), which is an excellent candidate due to its versatility (almost all elements of the periodic table can be mapped) and its high spatial resolution. In particular, the availability of probe spherical aberration correction, high brightness sources, and high angle silicon drift detectors (SDD) make this technique even more attractive since a high signal to noise ratio can be obtained with the characteristic resolution of STEM imaging techniques. In practice, the quantification of EDX spectra is achieved thanks to commercial softwares in which the different physical phenomena occurring between the X-ray emission in the TEM specimen and the X-ray detection are taken into account, so to avoid any impacts of experimental and theoretical artifacts on the final result.

Artifacts can be divided in two categories: artifacts related to the X-ray detector (peaks deconvolution, shelf, sum peak, etc...) whose impact is correctly taken into account in most commercial softwares; and artifacts related to the interaction between X-rays emitted in the analyzed specimen and the specimen itself, especially the X-ray absorption effect which depends on the mass absorption coefficient of each element in the sample as well as the specimen thickness and density. The most critical issue in the calculation of the absorption correction is that the mass absorption coefficient and the specimen density depend both on the specimen composition, which is the parameter to be measured. Consequently, iterative methods must be implemented for this calculation. In addition, when the exact relation between the specimen density and composition is not known, the reliability of the quantification results strongly depends on the approximation, which is used to describe it.

Optimized methods for the calculation of the X-ray absorption effect are finally implemented in the data treatment procedure leading from raw EDX spectra to quantified elemental maps. The two most common quantification procedures are the "ξ -factor method" and the "Cliff-Lorimer method". The ξ -factor method is based on the principle that the intensity of an X-ray is proportional to the mass-thickness and composition of the specimen. However, the disadvantage of this method is that an in-situ measurement of the beam current is required which is not measurable in the microscope setup used in this work. In contrast, the Cliff-Lorimer method that we have used in this thesis is based on the principle that the ratio of the X-ray intensity of two elements is proportional to the ratio of the corresponding mass fractions, with the proportionality factors called the Cliff-Lorimer (C-L) factors. In this method, the measurement of the beam current is not needed. However, its reliability relies on the precise knowledge of the C-L factors. Commercial softwares are typically based on theoretical values of the C-L factors, which can produce significant systematic errors.

Within this context, the objective of this thesis is to develop an improved Cliff-Lorimer method for the quantification of EDX elemental maps in semiconductor materials, with the specific aim to allow reliable measurements in the case of low concentrations of dopant impurities (below 1 at. %). In our improved method, the iterative correction of the X-ray absorption effect is based on the use of physical models describing the relation between the specimen density and its composition. For each one of the case studies considered in this work, the best-suited model is therefore specifically identified and applied to the quantification procedure. In particular, the "amorphous solid approximation" (based on the "Ideal Amorphous Solid" structure) will be used for the quantification of Arsenic dopants in Silicon before thermal annealing, while the "same radius approximation" (that assumes a negligible variation of the covalent radius between matrix and dopant atoms) will be shown to be valid for the quantification of Arsenic dopants in Silicon after thermal annealing. Finally, the "amorphous solid approximation" will be shown to be consistent with the "Vegard's law" and will therefore be used for the measurement of the Ge content in SiGe alloys pseudomorphically grown on a Si substrate.

In addition, the C-L factors used in our improved method are experimentally determined for the materials systems investigated in our work (i.e. As-doped silicon and pseudomorphically grown SiGe/Si stacks). For this, we used reference samples whose chemical composition was determined by the Rutherford Backscattered Spectroscopy (RBS) technique. By a direct comparison of EDX quantified data with RBS results, a reliable calibration of the C-L factors for the investigated elements could therefore be achieved.

Finally, we have developed an error estimation procedure based on linear regression and standard error propagation techniques in order to estimate the total experimental error in the dopant density as well as the detection limit for our experimental setup. This "total" experimental error includes (i) the statistical error on the measured X-rays intensity, (ii) the error on the calibrated C-L factors and (iii) the experimental error on the specimen thickness.

The background and the results of this work are presented in the first three chapters of this manuscript.

Chapter 1 contains a general description of the fundamentals of the electron microscopy and its related techniques, such as high resolution, Scanning electron Microscopy (SEM), Transmission Electron microscopy (TEM) and Scanning TEM (STEM). Then a detailed description of the EDX quantification technique will be given, including the various artifacts that have an impact on the quantified results. Finally, the existing quantification models will be presented, including the advantages and limitations of the related algorithms, with special attention to the Cliff-Lorimer method.

The new model that we have developed will be discussed in chapter 2. First, the iterative calculation for the self-consistent absorption correction is presented. Then, we will discuss the experimental calibration of the C-L factors that we have achieved by comparison with RBS measurements. The chapter will end with the presentation of the procedure for the estimation of the total experimental error.

Finally, in chapter 3, our quantification model will be applied to two different material systems, which are relevant in semiconductor processing: the quantification of Arsenic dopants in Silicon and the investigation of pseudomorphycally grown SiGe/Si stacks. In both cases, the experimental calibration of the C-L factors will first be carried out, followed by the application of the method to a technologically relevant case. In particular, in the case of Arsenic-doped Silicon, a 3D FinFET test structure will be investigated.

In parallel to the research activity focused on the quantification of EDX elemental maps, I have contributed, during my PhD, to some additional research projects being carried out in collaboration with other researchers within the LPCNO and the LAAS laboratories. In these activities, X-ray quantification techniques (in SEM or STEM mode) are needed to support other TEM-based structural characterisations of nanoelectronics materials of interest in future nanometric MOS or IoT devices. The results related to these activities will be summarised in the last chapter of this manuscript (chapter 4).

In the first part of the chapter, we report a simple and versatile laser-writing procedure to integrate flexible micro-supercapacitors and micro-batteries on current-collector free polyimide foils, starting from commercial powders. Such microdevices are good candidates for future IoT applications, to store energy and deliver power pulses while providing non-constant voltage output with time. The EDX analysis was first used to quantify the elements concentration in the fabricated structures (and therefore confirm the validity of the fabrication technique). Additional HREM and XRD (X-Ray Diffraction) investigations were conducted to identify the crystallographic structure of fabricated alloys.

In the second part of the chapter, we investigate the formation of metal silicides in Silicon nanowires, which are expected to replace the current FinFET architecture in future technology nodes. Our work in this project was focused on the determination of the crystalline structure of the fabricated metallic alloys using HREM and FFT (Fast Fourier Transform) method and on the subsequent confirmation of the structural analyses thanks to EDX quantitative analysis.

A summary of the main results obtained during my PhD as well as some perspective of the upcoming work will finally be presented in the General Conclusion of the manuscript.

Chapter 1

Energy Dispersive X-ray spectroscopy

EDX is an analytical technique used for chemical characterization. It relies on the stimulated emission of X-rays by electrons. This technique is normally used in an electron microscope and the emission is stimulated by a high-energy electron beam. The emitted characteristic X-rays can be used to obtain information on the specimen composition. The energy distribution of the characteristic X-rays is measured using an energy-dispersion spectrometer.

One of the advantages of the EDX technique over other spectroscopy techniques used in electron microscopy is the possibility to map a large range of elements with high spatial resolution. When compared with Electron Energy Loss Spectroscopy (EELS), for example, EDX gives better results on heavy elements (Ru, Au, Rh, Pt ...) and it can still be used for light elements [1].

Recent improvements in electron microscopy instrumentation have opened the way to new of EDX applications by allowing the experimenter to obtain spectral maps with an atomic resolution[2] and EDX techniques can be thus considered as en excellent candidate for elemental mapping on the nanoscale.

In particular, the good versatility of the technique in terms of observable elements combined with the elevated spatial resolution suggest that EDX could be used to characterize nanodevices (by studying both the doping and the metal distribution in the interconnection) as well as complex magnetic nanoparticles based on heavy metals, like those used in catalytic and magnetic applications.

But in spite of the recent instrumental progress, the quantitative application of EDX to nano-objects and nanodevices is still a challenging task. The low Signal To Noise Ratio (SNR) associated to the measurement of small objects or of elements in small concentration (such as dopants in nanodevices) calls for spectrum quantification models taking into account all the possible measurement artifacts in a rigorous way. In these particular cases, parasitic effects can be a critical issue since they can be of the same order of magnitude as the measured signal. The quantification algorithms thus represent a key step in the elemental mapping of nano-objects.

In this chapter, an introduction to EDX techniques will be given. The discussion will focus on the basic concepts and formalism needed to explain the new quantification model developed during my thesis work. The discussion will be organized as follows:

- First of all the fundamentals of several electron microscopy techniques (transmission and scanning electron microscopy) will be discussed.
- Then, a detailed description of the EDX technique will follow, including some details on the theory of electron-matter interaction , the physics of detection, and the quantification models
- Finally, a discussion on the available algorithms and computer program for the quantification of EDX spectra will follow with a specific focus on their limits for nanoscale and low concentration applications.

1.1 Electron microscopy

In Electron microscopy ([3] ch.1) electrons are used to obtain high resolution imaging. In general, it can be considered that the spatial resolution δ of a wave-optical device, is given by the the Rayleigh formula ([3] p.5):

$$\delta = \frac{0.61 \times \lambda}{\mathrm{NA}} \tag{1.1}$$

where λ is the wavelength of the electron and NA is the numeric aperture of the magnifying lens. The numeric aperture depends on the refractive index of the medium (a refractive index analog can be defined for electron waves [4]) and on the angular aperture of the lens. It can be shown that its value is approximately equal to 1. For an optical microscope using green light, the resolution amounts to 300 nm (NA= 1, and λ = 550 nm). This same formula can be applied to electrons since the wave-particle duality principle tells us that electrons behave, statistically, as waves. The idea behind electron microscopy is to obtain a high resolution by exploiting electrons. In 1925, Louis De Broglie[5] postulated that the wavelength of an electron depends on its energy according to the following law:

$$\lambda = \frac{h}{p} \tag{1.2}$$

where p, is the momentum of the electron and h is the Planck constant.

By using relativistic dynamics the following expression can be obtained for the electron wavelength:

$$\lambda = \frac{hc}{\sqrt{(eV)^2 + 2eVmc^2}} \tag{1.3}$$

where m and e are the electron mass and charge, respectively, c the speed of light and V is the acceleration voltage. With this formula it can be shown that a resolution of the order of the picometer can be obtained with a 200kV acceleration voltage. This is obliviously a considerable improvement when compared with light optics.

In practice, the theoretical resolution is not really achievable because of the presence of aberrations in the imaging system. Nevertheless, at present, a resolution of some Angstroms can be obtained with standard commercial devices and a sub-Angstrom resolution can be obtained by using aberration corrected microscopes. There are two main kind of electron microscopes, the Scanning Electron Microscope (SEM) and the Transmission Electron Microscope (TEM), both exploiting electrons but with a very different operation mode.

1.1.1 Scanning Electron Microscopy

In a **SEM** [6], a condensed beam is used to obtain information on a particular area of the specimen and the electrons forming the beam are characterized by an energy ranging between a fraction of a keV and 30 keV. As its name suggests, in a SEM, a specific area can be observed by scanning the specimen surfaces with the electron beam. The electrons from the primary beam are scattered in the material and, before being absorbed, they spread in a region called the volume of primary excitation. The characteristic length of this region depends on the material density and on the primary electron energy but is in the order of some microns. The electron-matter interaction in this volume causes the emission of several different signals (see figure 1.1(a) and section 1.2.1 for more details on the interaction mechanisms). Several information can thus be obtained by detecting different signals. In particular:

- In the primary region Secondary Electrons (SE) are emitted by ionization of atoms in the specimen by the primary beam. The secondary electrons have a small energy thus their absorption length is in the order of some nanometers the exact value depends on specimen density and incident beam energy). As a consequence only the secondary electrons emitted in the upper part of the excitation volume get off the specimen to be collected by the SE detector. The detection of secondary electrons can be used to obtain information on a layer with a thickness of some nanometers located just below the surface of the specimen. SE electrons are generally used to obtain 3D information on the specimen surfaces. To understand why it must be noted that their emission intensity is proportional to the cosinus of the angle between the surface normal and the SE detector. This is the same dependence followed by the intensity of light reflected by a surface, which depends on the angle between the reflecting surface and the optical detector (or the eye of the observer). The obtained image can thus be used to visualize the surface reliefs by just "looking at" the obtained image as we would look at a 3D object illuminated by light. More sophisticated techniques can be used to obtain additional information on the surface (composition, electric potential ...) by using the SE signal.
- Back-scattered Electrons (BSE) can also be collected using a specific detector.

Since they have larger energy than SE, BSE are originated from deeper regions of the interaction volumes (characteristic lengths of the order of 10 to 100 nm). Since they come from regions farther away form primary electron beam, BSE imaging has lesser resolution than SE imaging. On the other hand, since the intensity of back-scattering strongly depends on the local specimen density, it can be used to obtain direct information on the specimen composition. As a rule of thumb it can be considered that high density regions in the specimen correspond to brighter regions in the BSE image. This is only applicable to flat specimens since on irregular surfaces some region of specimen can be located between the emission point and the detector. This shadowing effects, together with a careful design of the detector can be used to obtain topographic contrast with BSE.

- Electrons from the primary beam also cause the emission of X-rays (see section 1.2.1). Since the absorption length of the emitted X-rays is of the order of some microns, the resolution of EDX techniques in the SEM is micrometric. Still the application of these technique on specimens with a uniform distribution is very interesting since a high SNR can be obtained due to the large size of the interaction volume. For the quantification special techniques (known as ZAF techniques [7]) can be used to quantify the EDX signal by taking into account the fact that X-rays are not only emitted near the beam impinging region but in the whole interaction volume.

It must be noted that the interaction volume can be greatly reduced by observing specimens having a negligible thickness with respect to the size of the volume of interaction. In this case it can be considered that all X-rays are emitted in the beam focusing point (see figure 1.1(b)) and the EDX resolution equals the beam size. This can be achieved by using specimen preparation techniques (mechanical thinning and grinding, ion beam thinning ...) to the specimen before observation. This is the configuration normally used in a transmission electron microscope in scanning mode (STEM) or in a SEM by using a dedicated specimen holder.

1.1.2 Transmission Electron Microscopy

In a **TEM**, as the name suggests, the detected signal consists of electrons transmitted trough the specimen. As a consequence only "thin" specimens can be observed. The maximum acceptable thickness for the specimen to be "transparent" to electrons depends on the specimen density and composition but is in the order of 100 nanometers. Specimens typically observed in a TEM are either nanometric objects supported on thin organic grids or bulk material and devices thinned using the combination of mechanical and ion beam techniques. The energy of the electrons of the beam ranges, in a TEM, between 80 keV and 300 keV.

The basic TEM column can be divided in several blocks [3] (see figure 1.2).

An electron gun located on the top of the microscope generates the electron current. Several kind of guns are used in commercial microscopes.

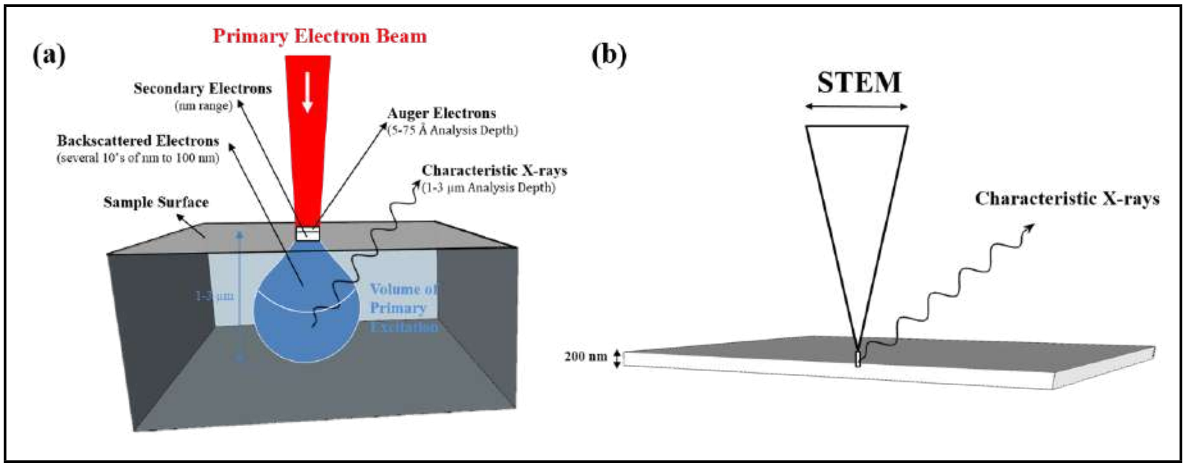

Figure 1.1: Schematic drawing of electron-matter interaction in bulk (a) and thin (b) specimens.

- In the most simple (**thermionic**) guns, a metallic filament is heated and electrons are emitted by thermal effect. The degree of spatial coherence of this kind of source is low since electrons are emitted from a large region near the gun tip and the emitted electrons have an energy spread (temporal coherence) due to the heating of the gun. In a thermionic gun the source size is of the order of some microns and the energy spread of the order of some electron volts.
- Better coherence and an improved beam current can be obtained by using **Schottky** Field Emission Guns (FEG). In this kind of sources the extraction potential is lowered by the creation of a strong field on the gun tip. Since the field strength of the created field is stronger when the radius of curvature is lower, most electrons are emitted from a narrow region near the tip. Schottky guns are also heated up to obtain electron emission but less heating is needed thanks to the extraction potential lowering. Schottky guns have better coherence than thermionic guns. They also have a higher brightness, which means that a higher current can be obtained when focusing the beam in a small region. The source size is of the order of 10 nm and the energy spread of approximately $0.7eV$.
- In **cold FEG** guns, electrons are also extracted thanks to potential lowering near the gun tip but no additional heating is provided. As a consequence better coherence and higher brightness is obtained. The source size is of the order of some nanometers and the energy spread of about $0.3eV$. Since surface contamination has a strong effect on the emitted current, cold FEGs have more strict requirements in terms of vacuum than other sources and must be periodically "cleaned". For that a short temperature spike (also called flash) is used. The current in cold FEG guns degrades with time and source flashes must be periodically used to restore it to its maximum value.

The current generated by the gun can be focused or spread on the specimen using the

condenser system. The microscope can thus be used in a TEM mode or a scanning TEM (or STEM) mode (see figure 1.3). In TEM mode the beam covers the observed region and the electron wave, after interacting with the specimen, is used to form an image using the objective lens and the projection system. In the STEM mode the beam is focused on a specific location of the specimen and and an image is created by scanning the beam over the observation region. The main difference between the SEM and STEM mode is that in STEM, in addition to the EDX detectors, several detectors located after the projection system can be used to obtain transmission images. Since the resolution in STEM mode is dictated by the beam size, in modern microscopes the condenser system is equipped with a spherical aberration corrector. Using aberration correction an high coherence sources such as cold FEG sources, electron probes of sub-Angstrom size can be obtained.

The **objective lens** is used to provide a first magnification of the image. To minimize lens aberrations, an immersion lens is normally used. This means that the specimen is inserted, using the specimen holder rod, in the middle of the polar pieces generating the objective lens field. A magnified image is created on the plane that is optically conjugated to the specimen plane, and a diffraction image on the image focal plane of the objective. The distribution of the magnetic field located before the specimen can be modified using separate coils. The pre-specimen field and the additional coils are sometimes referred to as the mini-lens even the specific design varies in different microscope models. The mini-lens can be used to further modify beam convergence. It can for example be used to provide additional convergence in STEM mode or to obtain a parallel beam in diffraction mode.

The **projection system** is composed by the diffraction intermediate and projection lenses. It provides further magnification and can be used to select the plane to be projected on the fluorescent screen or the image recording system. In diffraction mode, for example, the image focal plane of the objective lens is selected.

1.1.3 Image formation in the TEM and STEM modes

As already explained in the description of the condenser system in a TEM two main operation modes are used to characterize a thin specimen the TEM mode and the STEM mode (see Figure 1.3). The image formation mechanisms are quite different in the two cases and complementary information can be used by using the two modes. In this section the advantages and disadvantages of each mode will be discussed together with the fundamentals of image formation.

As previously discussed, in **TEM mode** the electron beam covers entire observed area and an image is obtained by using a recording device such as a photographic plate or a digital camera. This means, in the case of digital acquisition, that the image recording consists in a parallel digital acquisition of all the pixels composing the

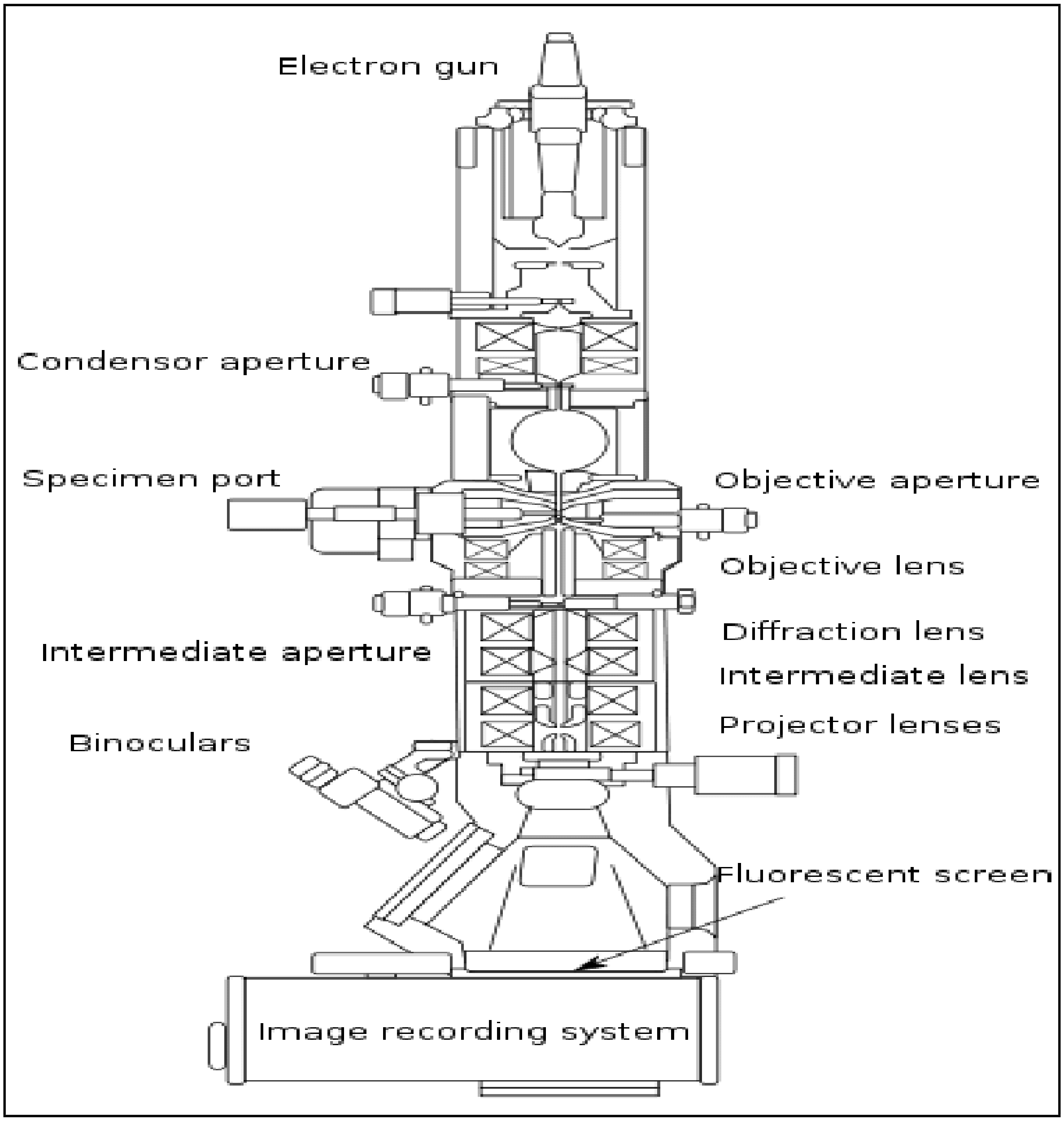

Figure 1.2: Schematic drawings of the main elements of a transmission electron microscope.

picture. On the other hand, in STEM mode, the beam is focused in a small region and the image is obtained by scanning and serial acquisition of the recorded signal. A direct consequence of the differences between the operating modes is that acquisition of an image in STEM is normally longer than a TEM acquisition. Moreover, since the beam is focused, specimen damage is much more critical in STEM mode.

On the other hand the **STEM mode** is the most suited to perform elemental mapping. In the particular case of EDX the only elemental information that can be obtained in the TEM mode is the average composition of specimen area under the electron beam. For EELS things are a bit different but it can be shown that even if elemental maps can be obtained in the TEM mode, the resolution obtained using STEM/EELS is much higher[8].

To understand what kind of information can be obtained form TEM and STEM images, we must discuss how images are formed in these two modes. Since in this thesis we have studied nanometric objects the discussion will be focused on high resolution imaging.

In the **High Resolution TEM (HRTEM) mode** [9] the incident wave is modified after interacting with the specimen. We will call this modified wave the object wavefunction. The objective lens modifies the object wavefunction by magnifying it and adding distortions due to lens aberrations. A final image is then formed by the projection lens. It can be shown that in order to obtain a maximum resolution, it is necessary to obtain a defocused image using the projection system. This means that the object plane of the projection systems must be separated by a distance $\Delta z_s = \sqrt{\frac{3C_S}{\lambda}}$ from the objective image plane. In the previous equation, C_s corresponds to the spherical aberration coefficient of the objective lens. This distance is known as Scherzer defocus while the associated optimal resolution $d = \sqrt[4]{\frac{C_s}{6}\lambda^3}$is called the Scherzer resolution. Without going into the details of the formed image it can be noted at this point that an HRTEM image provides information on the periodicity of the atomic arrangement of the observed specimen.

HRTEM imaging is often coupled with Fourier analysis This is accomplished by using Fast Fourier Transform (FFT) [10] algorithms on digitally acquired images. The use of FFT allow the experimenter to easily analyze the spatial frequencies present in the HRTEM image. This information can be used to identify the crystal structure of the specimen since the measured spatial frequencies are related to the crystal reciprocal lattice[9].

In the **High Resolution STEM mode,** quantum mechanics must again be used to understand what kind of information can be obtained from the final image. The analysis of the wave function behavior can be simplified by using a very useful principle called the TEM/STEM reciprocity principle [11]. One interesting consequence of this principle concerns the images obtained a Bright Field (BF) detector, i.e. a detector collecting only the electrons forming a small angle with the optical axis. It can in fact be shown, using the reciprocity principle, that a Bright Field STEM (**BF-STEM**) image must show the same kind of contrast of a HRTEM image.

Things are different when electrons scattered at high angles are detected using a High Angle Annular Dark Field Detector (HAADF) . In this case it can be shown that the collected signal is approximately proportional to Z^2 where Z is the atomic number of the scattering atoms. In a **STEM/HAADF** image the contrast is thus directly connected to the local specimen density and thickness, and higher density or thicker regions appear as lighter.

Both BF-STEM and STEM/HAADF can be combined with STEM/EDX allowing the experimenter to obtain simultaneous information on the specimen composition and structure.

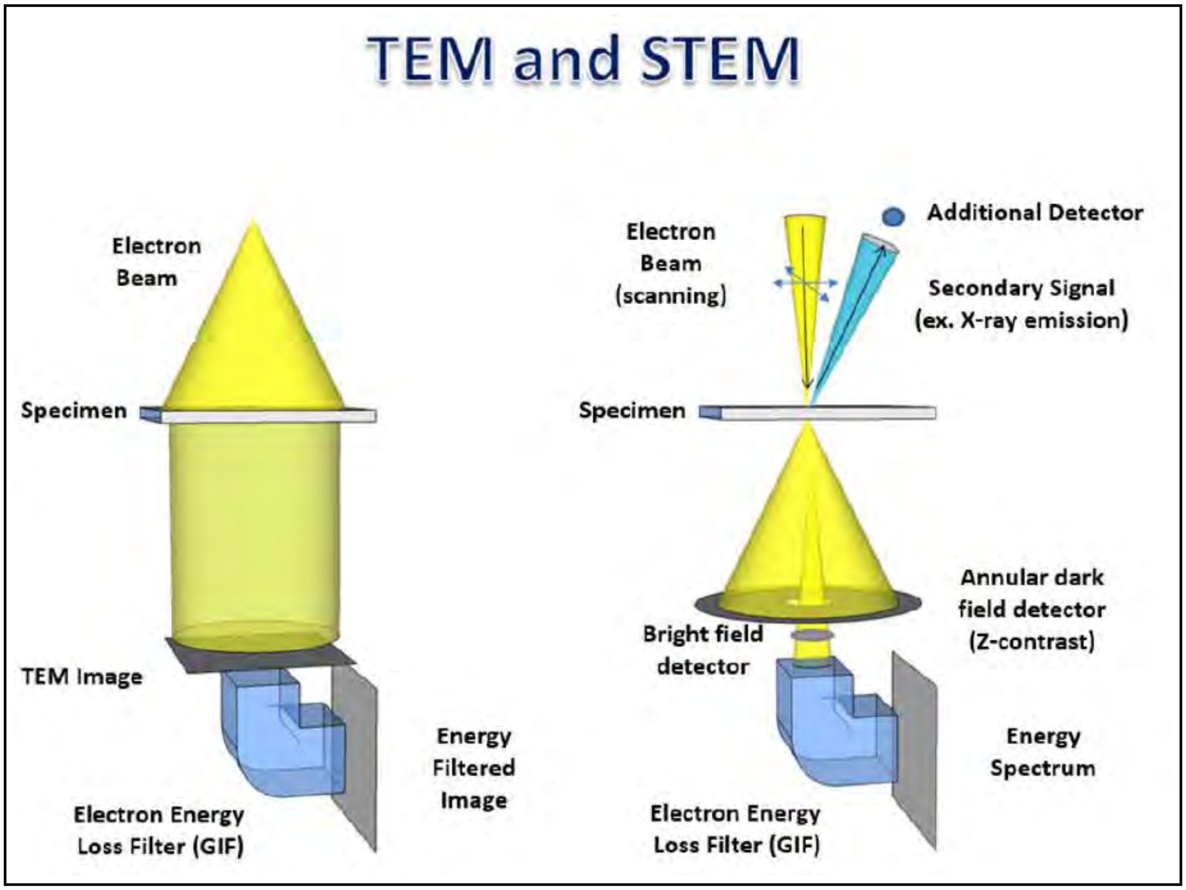

Figure 1.3: Schematic drawing illustrating the TEM and STEM modes.

1.2 The physics of EDX spectroscopy

In the following discussion, we will explain the basic phenomena involved in EDX spectroscopy including the different electron-matter interaction mechanisms, the EDX detector and the various artifacts associated with this technique. In addition, an overview of the existing quantification models and available quantification programs will be provided. The discussion will be focused on the critical issues affecting the mapping of nanodevices and nano-objects and on the limitations of the different models.

1.2.1 Electron-Matter Interaction

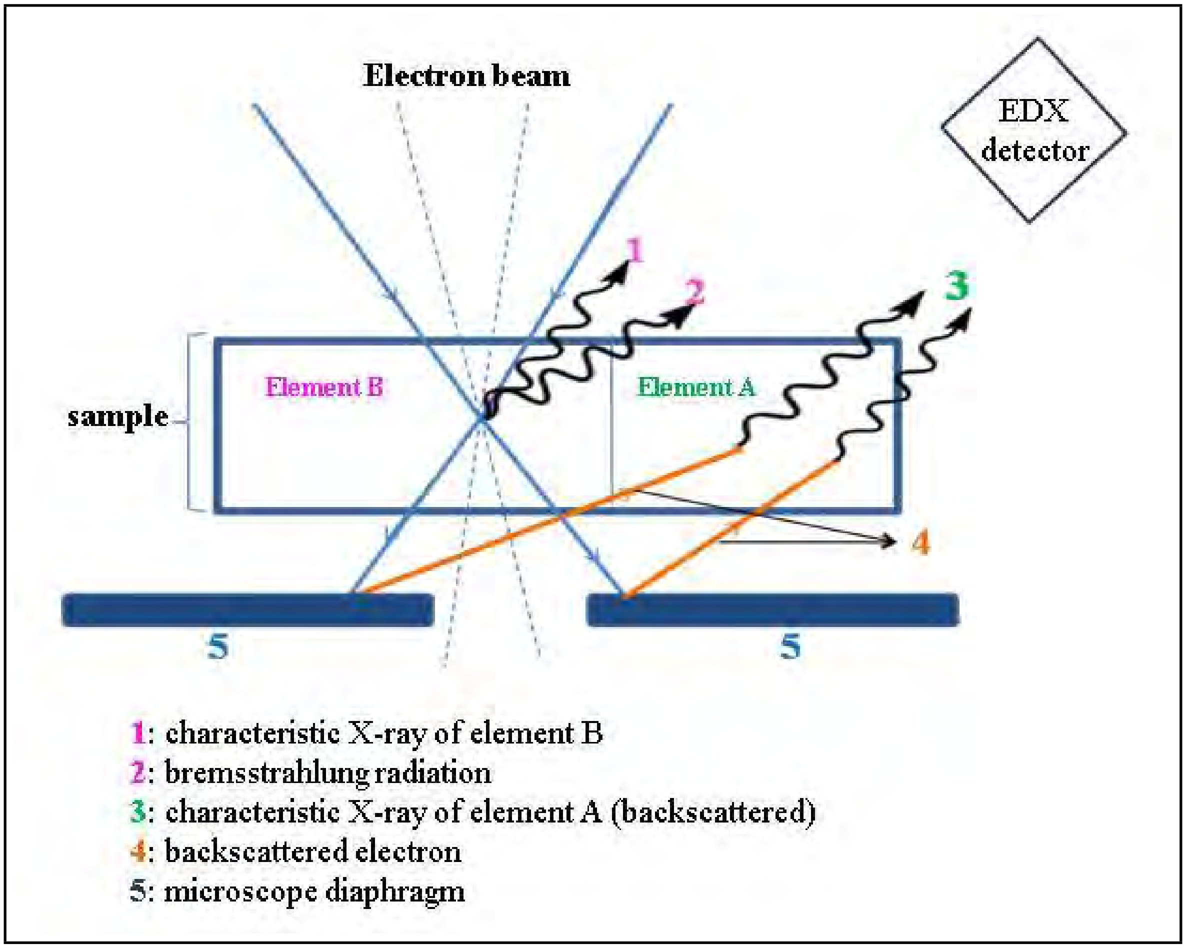

Figure 1.4: Diagram explaining the three physical phenomena resulting from the interaction of the electron beam with the sample: characteristic X-rays, Bremsstrahlung radiation and electron backscattering.

In an electron microscope, the interaction between beam electrons and the specimen can have several consequences (see Figure 1.4).

First of all, **characteristic X-rays** ([3] p.605) can be generated when a high energy electron interacts with an atom of the sample and ionizes it by releasing an electron from an inner shell. The energies associated to the characteristic peaks can be obtained using the X-ray transition energies database[12]. When the incomplete inner shell is filled by an electron coming from an external one, the excess energy can be released in the form of an X-ray. The energy of the emitted X-ray depends on the energy difference between the outer and the inner shell. Each element of the periodic table therefore gives rise to the emission of characteristic X-rays with different energies. Each peak is identified using the Barkla notation [13]. In this notation a first roman uppercase letter is used to indicate the inner shell (K for the n=1 shell, L for the n=2 shell ...). The letter is followed by a Greek letter used to sort the characteristic X-rays (also called lines) in order of increasing energy. For example the lowest characteristic X-ray involving a n=1 inner shell is called Kα, the following one Kβ ...). In fact the notation is more complex and involves the employ of subscripts and superscripts in order to take into account subshells.

In addition **bremsstrahlung** radiation (braking radiation) [14] can be emitted emitted when the electrons are deflected by an atomic nucleus. Even if the associated probability is low, inelastic scattering can take place and the electron can loose a significant amount of energy. This energy is released in the form of an X-ray (see Figure 1.5(a)). Statistically speaking, a Bremsstrahlung x-ray can have an energy ranging from zero to the total incident electron energy. Since the probability varies with the energy loss, Bremsstrahlung radiation has a continuous shape. It can be shown that the noise intensity as a function of the energy follows Kramer's law [15]. From the point of view of an EDX measurement, this radiation can be interpreted as a background noise.

Finally, the electron can be **backscattered** ([3] p.611) in a collision with an atom of the specimen. In this case the deflection angle is greater than 90° and electrons have an energy higher than 50 eV. It has to be noted that in a TEM backscattering not only takes place in the sample but can also be caused by the presence of components located near to the specimen (such as the specimen holder or the objective aperture, see figure 1.2). In this case the backscattered electron can be responsible for the presence of artifacts due to the emission of X-rays in regions located outside the electron beam (see labels 3 and 4 in Figure 1.4).

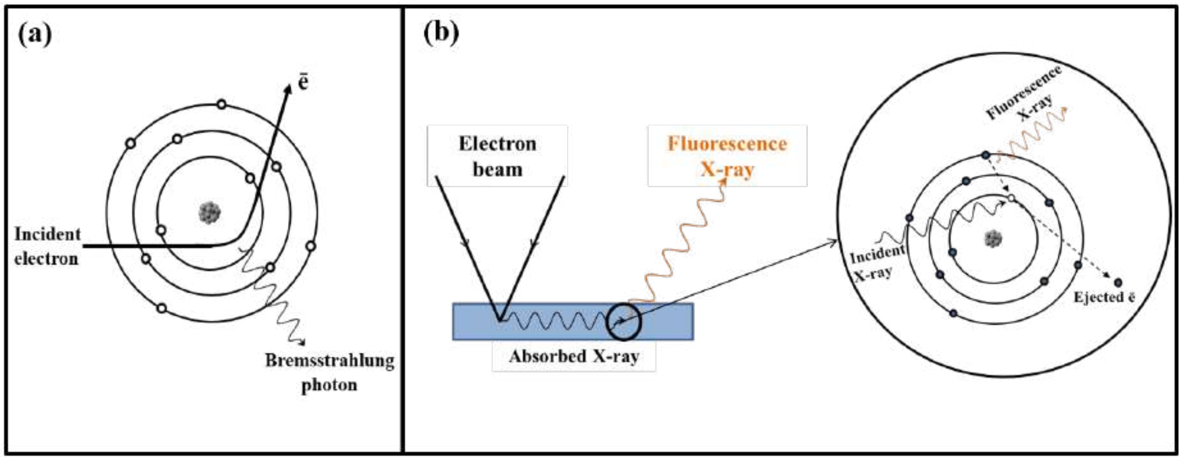

Figure 1.5: Schematic drawing illustrating the origin of Bremsstrahlung radiation (a) and Fluorescence (b).

Once emitted and independently of their origin and energy the X-rays can interact in many ways with the sample before reaching the EDX detector. This means that the emitted radiation is modified before being measured by the detector and it is important to take these effects into account in order to obtain quantitative information from the measured spectra. In particular, X-rays can be absorbed before reaching the detector. Two kind of absorption are possible:

- X-ray **fluorescence absorption** [16]: in this case a characteristic X-ray emitted by an atom of the sample is absorbed by another atom of the sample before reaching the detector. A new X-ray, with a potentially different energy is created in the process. By the energy conservation principle, X-ray generated by fluorescence must have a lower energy than the absorbed X-ray. As in the case of backscattering, fluorescence can take place in regions of the specimen or of the microscope located outside the electron beam at it is responsible for the presence of artifacts. (see Figure 1.5(b)).
- **Non-radiative absorption** of X-rays in the sample such as those described in the following section for the absorption of an X-ray in a semiconductor.

In summary we have seen that two kind of x-rays can be measured by an EDX detector: the **characteristic X-rays**, that contains the composition information and the **bremsstrahlung radiation**, that can be considered a background noise. The X-rays can be **absorbed** in the specimen and **spurious X-rays** can be generated by **fluorescence** or **backscattering** causing measurement artifacts. Since these artifacts are due to the presence of the specimen we will refer to them as **specimen artifacts** in the following. Specimen artifacts cannot be eliminated and must be taken into account in the quantification methods. In particular we will show in the following that **a rigorous treatment of absorption effects** is a key issue for quantitative mapping at the nanoscale.

1.2.2 The EDX detector

To take into account all the physical phenomena involved in an EDX measurement, we need to describe the basics of EDX detection.

The EDX detector is an instrument capable of measuring the energy of incident X-rays and represent them in the form of a spectrum, i.e. an histogram of the X-rays energy distribution measured during a specific time interval (also called exposition time). As already discussed a spectrum contains characteristic peaks superimposed to the Bremsstrahlung background noise. In order to discuss the possible measurement artifacts associated to the detection step the X-ray/matter interactions taking in place in the detector will be reviewed.

The simplest form of EDX detector consists in a reverse-biased p-i-n diode (made up by a succession of a P-doped an intrinsic and an N-doped region). The p and n regions are heavily doped (and will be thus labeled p+ and n+) to be able to create ohmic contacts at its extremities. In the case of an ideal detector the emitted X-rays are absorbed in the intrinsic zone and they generate electron-hole pairs (see Figure 1.6). The number of generated carriers is proportional to the X-ray energy and the carriers are collected at both ends of the detector due to the applied polarization. The collected charge which is proportional to the energy of the incident X-ray, is then converted into a voltage that represents the measurement output. Even if modern detectors, such as Silicon Drift Detectors (SDD) have a more elaborate design (see section 1.2.3), we will use the simple structure depicted in figure 1.6 to better illustrate the different phenomena. The same reasoning can in fact be applied to more complex geometries such has the one used for modern SDD detectors. In real detectors some **instrumental limitations** must be taken into account.

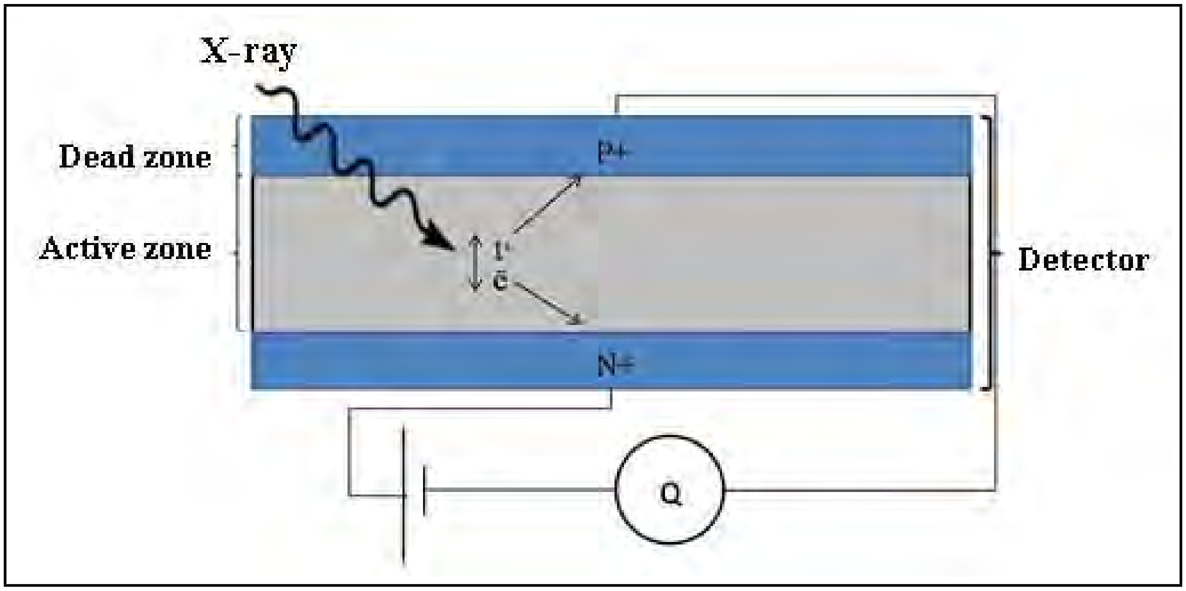

Figure 1.6: Diagram showing the structure and operation of a simple p-i-n EDX detector.

First of all the detector has a **finite extension** and it can only capture a fraction of the X-rays emitted by the specimen. The geometric efficiency of the detector is expressed by the detection angle, which represents the solid angle covered by the detector active surface. The detector solid angle is obviously a function of the detector active surface and its distance from the specimen.

In addition the detector has a limited **energy resolution**. We will not detail the physical mechanisms but we will limit ourselves to observe that because of these effects a characteristic peak, which ideally corresponds to a maximum of intensity located at a given energy, will have, in practice, a Gaussian profile[7]. The energy resolution will corresponds to the Full Width at Half Maximum (FWHM) of the peak $\sigma_{FWHM}(E)$ that can be calculated using the following equation:

$$\sigma_{FWHM}(E) = \sqrt{A(E - E_{ref}) + [\sigma_{FWHM}(E_{ref})]^2} \tag{1.4}$$

where A is a constant depending on the EDX detector, E_{ref} is an arbitrarily chosen reference energy, and all energies are expressed in electron volts.

Moreover, **absorption can take place** for the less energetic x-rays in the metallic contacts or in the other layers which may possibly cover the surface of the detector. This effect can be eliminated, at least in principle, by calibrating the response of the detector to different energies with X-rays of known energy and intensity [17].

To conclude the discussion on the detector limitations, two kind of artifacts must be discussed into detail.

1. **Collection artifacts** arising when the X-ray is absorbed in the detector but the generated charges are not fully collected.
2. **Temporal superposition artifacts** which can take place when the intensity of the incident photons is very high. In this case there is a non negligible probability that a photon can arrive in the active zone before the charges generated by a previous photon are collected. In this case the contribution of the two photons cannot be distinguished.

Collection artifacts

To understand collection artifacts it must be considered that the conversion of an X-ray into electron-hole pairs can be done through **intermediate conversion phenomena** (see Figure 1.7(a)). More specifically two intermediate phenomena can be responsible of the formation of an electron-hole pair by absorption of an X-ray:

1. Auger electron emission ([3] p.60), which occurs when X-rays ionize the electron from an atomic inner shell. The additional energy created when the inner shell is filled by an electron coming from an outer shell can cause the ionization of weakly bound outer shell electron (see Figure1.7(b)).
2. The emission of an X-ray by fluorescence, which has already been detailed previously.

In addition it must be considered that the detector has inactive zones in the p+ and n+ regions (often called **"dead layers"** in literature). This is due to the presence of defects introduced during the creation of highly doped regions. This is mainly due to the presence of crystalline defects (precipitates, interstitial, residual ionic implantation defects, ...) in the doped zones. The defects acts like traps for the carriers and can cause pair recombination.

The combination of **intermediate conversion phenomena** and the presence of **dead layers** is at the origin of several artifacts (see Figure 1.8):

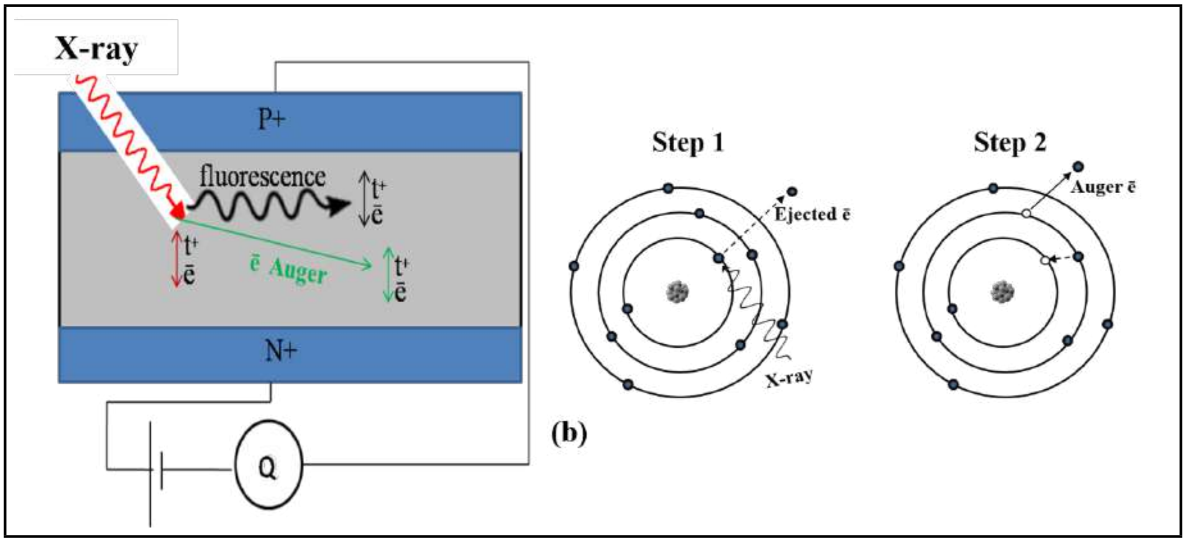

Figure 1.7: Diagram representing the three intermediate mechanisms for carrier ionisation in the detector (a) and the emission process of an Auger electron (b).

- **Absorption in the dead layer -** The X-ray is absorbed in a dead zone and no electron-hole pair is generated. This is additional absorption effect to take into account when evaluating X-ray absorption in the detector.
- **Incomplete charge collection -** Some of the intermediate electrons generated by the X-ray are absorbed into the dead zones of the detector ([3] p.595). This means, in practice, that a fraction of the X- ray energy is not detected and the value of the measured energy is therefore lower than the real one. Moreover, because of incomplete charge collection, the energy of certain photons is underestimated by the detector. The energy of some photons are thus shifted and this causes a deformation of the theoretically predicted Gaussian shape of the characteristic peaks. Due to the form of the deformed peaks the incomplete charge collection mechanisms are normally addressed as **"tail"** and **"shelf"** ([3] p.610) artifacts. It is important to consider shelves and tails as a part of the signal to be measured and not be associated to background noise.
- **Escape Peak -** A fluorescence X-ray can be emitted in the detector but not detected since it leaves the detector or is collected in the dead layer ([3] p.606). The "missing" X-ray which must necessarily be a characteristic X-ray of the material that composes the diode. As in the previous case, the measured energy for the incident X-ray will be lower than the real energy. In the specific case of detectors based on Si diodes, for example, the detected energy is reduced by 1.74 keV which corresponds to the $K\alpha$ line, the strongest line of the characteristic silicon peaks.

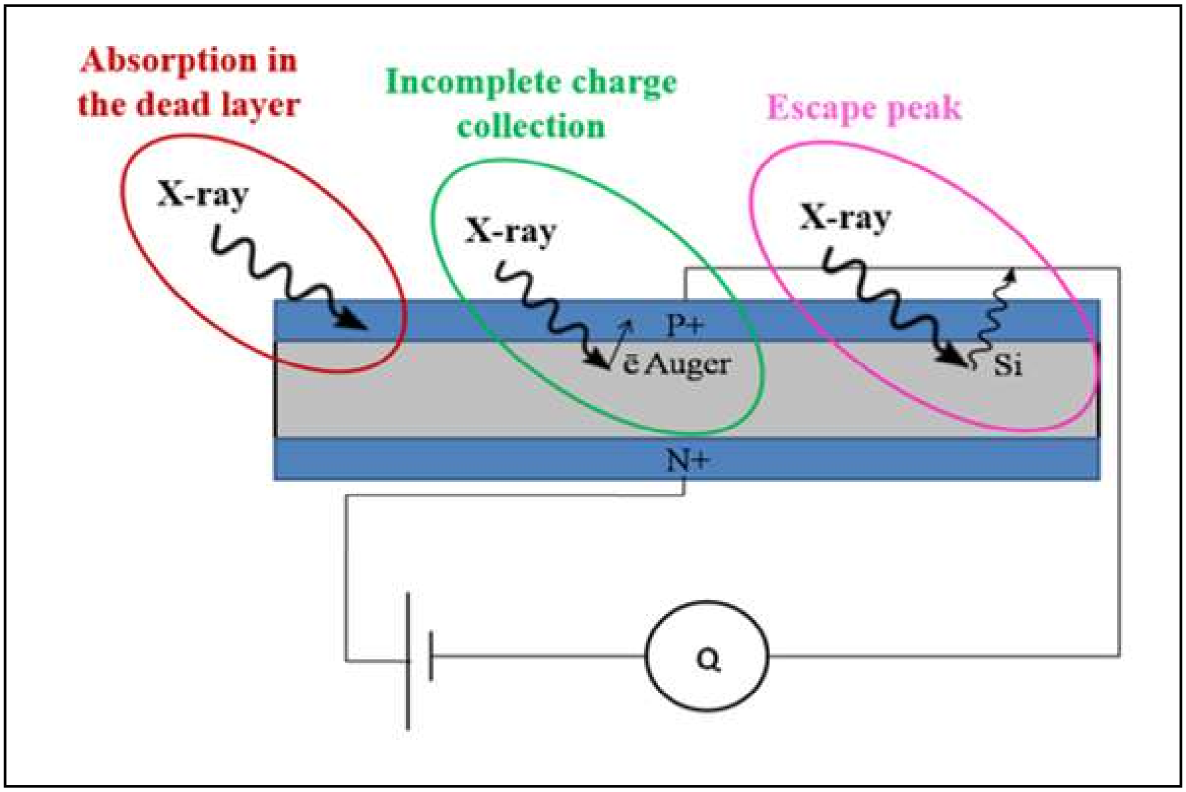

Figure 1.8: Diagram representing the detection artefacts.

Temporal collection artifacts

These artifacts are due to the temporal superposition of X-rays. To simplify the explanation we will not give details on the electronic conversion of the detector and we will limit the description on its general operation mechanisms. These artifacts take place when an energy X-ray E_B arrives on the detector while carriers previously excited by an energy X-ray E_A are still present in the detector. The detector electronics is equipped with a rejection function to deal with the temporal events overlap. If a temporal overlap is detected both measurements are rejected. But the detector rejection function obviously is not perfect and if the arrival times of the two X-rays is below a the rejection function sensibility the two X-rays are measured as a single X-ray and the measured energy is equal to $(E_A + E_B)$. It is the possible to observe, in a spectrum obtained with an elevated x-ray yield, a **sum peak** located in $E_A + E_B$ in addition to the characteristic peaks located in E_A and E_B ([3] p.607).

1.2.3 SDD detectors

SDD EDX detectors are new generation devices exploiting a circular geometry to drive electrons, generated between the back contact and the front contacts, in the central region of the detector (see image 1.9). The collection is made possible by the

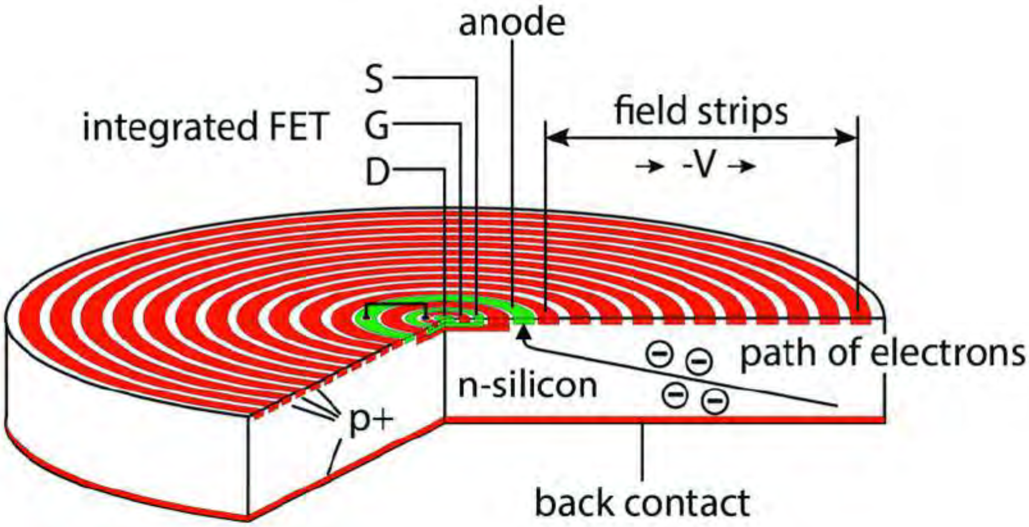

Figure 1.9: Schematic drawing of an SDD detectors, taken from [18].The image is available under the license Creative Commons Attribution International 4.0 (https://creativecommons.org/licenses/by/4.0/).

presence of several circular metallic contacts (field strips) creating an electric potential distribution which drives the electrons toward the central collection transistor. The source(S), drain (D) and gate (G) region of the transistor are indicated in the figure, and the entry point for X-rays is through the back contact.

Without going into the full details of its operation (see [19]for more details), it must be noted that one of the main advantages of an SDD detector is that, thanks to its specific design, the detector has a faster response than standard devices, and can be safely used for high counts measurements. Moreover, it has negligible "dead layer" regions, and this reduces the influence of charge collection artifacts.

The vast majority of new generation EDX detectors (including those used in our experiments) are equipped with and SDD device.

1.2.4 Summary of EDX artifacts and limitations

In this section we have reviewed all the instrumental limitations and possible artifacts affecting EDX spectra. To better understand how different artifacts affect the final measurement we can summarize the previous discussion as follows:

- The non ideality of the EDX detector can be taken into account by considering that the detector has a limited **energy resolution,** a finite detection **solid angle**, and because of **absorption effects** in the detector surface and dead layers, the intensity response of the detector at various energies must be calibrated. This is normally taken into account by the **manufacturer**, and for commercial EDX detectors, information on the solid angle and resolution is provided. The equation

1.4 is used to evaluate the resolution for a specific energy after calibration of the A constant using a reference peak. The intensity response is taken into account by direct spectrum correction or by providing the intensity response vs energy curve, also called the detector quantum efficiency curve. If the dead layers of the detector have a large extension the peak shape can be distorted by **incomplete charge collection effects** and the manufacturer must also provide some methods to take into account or correct these distortions. It has to be noted that when using modern devices such has SDD detectors, thanks to improved control of doping mechanisms and dead layers, peak distortions can be safely neglected.

- Compositional information can be extracted by measuring the **characteristic peaks intensities** after **bremsstrahlung subtraction**. For this dedicated computer programs can be used (more details will be provided in the next section). If the intensity of measured spectrum is high or the extension of the dead layer is non-negligible, spurious peaks such as **escape and sum peaks** can appear in the spectrum. This must be taken into account by the experimenter. As already discussed since the dead layers thickness is reduced, in modern devices escape peaks can safely be neglected. Moreover, as already discussed, low X-rays current are normally obtained when applying EDX techniques to nano-objects. As a consequence possible complications due to the presence of sum peaks can be safely neglected.
- There is a an additional unavoidable category of artifacts due to the presence of the specimen. For obvious reasons **specimen artifacts** cannot be accounted for by the EDX detector manufacturer. The **rigorous physical modeling** of these kind of artifacts has been **the main focus of my thesis work and more details on the techniques developed and their applications to nanodevices will be given in the following chapters**.

1.3 EDX Quantification

As already discussed, the compositional information in a spectrum is encoded in the height and position of the different peaks. In order to obtain quantitative information on the specimen composition a model correlating characteristic peak heights to the concentration of the different elements composing the specimen must be used. The different types of quantification methods and the existing computer programs implementing the quantification techniques will be described in this section. The discussion will be restricted on the quantification of EDX data in TEM/STEM.

1.3.1 Quantification Methods

Cliff-Lorimer method

This method is widely used in TEM because it is based on a thin sample approximation. The Cliff-Lorimer (C-L) method is based on a linear approximation. If we label the $N_A$elements present in the specimen with integer labels, the relation between the mass fractions of two elements i and j and the characteristic peaks intensity is given by ([3] p.640):

$$\frac{f_i^M}{f_j^M} = K_{i,j:F_i,F_J} \frac{I_{i:F_i}}{I_{j:F_j}} \tag{1.5}$$

where f_i^M is the mass fraction of the $\mathrm{i^{th}}$ element and $I_{i:F_i}$ is the associated intensity of the specific peak. It has to be noted that to apply this method, a specific peak family F_i=$K, L, M, \ldots$ has to be selected for each element. $K_{i,j:F_i,F_J}$ is the C-L factor and depends on the peak family chosen for each element. The only information needed to apply this method is the C-L factors associated to the different peaks used for the composition quantification. It is common practice in EDX software to provide a full set of simulated values for the C-L coefficients. As an alternative they can be experimentally measured by using a specimen of known composition containing the two elements.

Zeta Factor method

The ξ-factor method is based on the principle that the intensity of an X-ray line from an element A in a thin-film (i.e. ignoring absorption or fluorescence effects) is proportional to the mass-thickness and composition as the following [20, 21]:

$$\rho t = \xi_A \frac{I_A}{C_A D_e} \tag{1.6}$$

where ρ is density, t thickness, $I_A$the intensity of the peak above background, C_A the composition and $D_e$the total electron dose and can be expressed as the following:

$$D_e = \frac{I_p \tau}{e} \tag{1.7}$$

where I_p is the in-situ beam current, τ is the acquisition time and e=1.6022*10^{-19} is the electron charge.

If the same equation is applied on an element B we obtain:

$$\rho t = \xi_B \frac{I_B}{C_B D_e} \tag{1.8}$$

And since $C_A + C_B = 1$ then C_A,$C_B$and ρt can be expressed as the following:

$$\rho t = \frac{\xi_A I_A + \xi_B I_B}{D_e}, C_A = \frac{\xi_A I_A}{\xi_A I_A + \xi_B I_B}, C_B = \frac{\xi_B I_B}{\xi_A I_A + \xi_B I_B} \tag{1.9}$$

The advantage of the zeta factor method in comparison with the Cliff-Lorimer method is that pure element standards can be used for calibration. [21]. Pure-element standards have the distinct advantages of being easy to fabricate and they don't change composition during the thinning procedure or due to the beam damage. The main disadvantage is that an in-situ measurement of the beam current is necessary to apply this method, and standard TEM/STEM are not normally equipped for this kind of measurement.

Cross Section method

This method is used to calculate an EDX partial cross section in similar way of the ξ-factor method [22]. For thin samples, X-ray absorption and fluorescence can be neglected. In this situation, the number of X-ray counts is linearly proportional to sample thickness, therefore we can define an EDX partial cross section, σ, for a single atom of any given element, x, as:

$$\sigma_x = \frac{I_x e}{i \tau n_x t} \tag{1.10}$$

where I_x is the intensity of the X-ray of the element x, e is the unit electronic charge, i is probe current, τ is the total pixel dwell time and $n_x t$ is the atom density per unit area.

If the partial cross section of each element for a particular microscope are known, it is possible to calibrate EDX maps into atom counts, N_x, per pixel of the spectrum image using the following equation:

$$N_x = n_x t A = \frac{I_x e}{i \tau \sigma_x} \tag{1.11}$$

where A is the illuminated area. As in the case of the ξ- factor method, pure calibration specimens can be used an in-situ beam current measurement is needed.

The advantage of this method is its simplicity of implementation but it is not well adapted to specimens providing a low EDX signal.

1.3.2 Quantification software

As already discussed, in order to extract information on the specimen composition from EDX measurements, background noise must be subtracted first. Then the characteristic peaks intensity (corresponding to the peak area) must be calculated. Finally a quantification model must be applied to obtain information on the composition. This sequence of operation is implemented in some specific computer programs that can be used for the treatment of EDX data. In this section we will review the available computer programs with particular attention to their strength and weakness. The possibility to obtain quantitative information using the existing software will also be discussed.

It has to be noted that both commercial and free software exist. A really interesting feature of existing free computer programs for EDX data treatment is that they are also open-source. This means that a precise knowledge of the algorithm implementation can be obtained by looking at the code, and some of the software features can be reused. Code re-usability has been used in the development of the model used in this thesis, as explained in the following. Two **free** computer programs will be reviewed in the following **NTSA-II** and **Hyperspy**.

Commercial software is mainly developed by manufacturers to be sold with the EDX detectors. In the following just two commercial computer programs will be reviewed since all the presented EDX data have been obtained using two detectors provided by two different manufacturers: Bruker and JEOL. As a consequence I have only used the **Esprit** program, developed by Bruker, and **Analysis Station**, developed by JEOL.

It must also be noted that the **NTSA-II** software is not suited for EDX treatment in TEM since the allowed maximum beam energy is of 80 keV. Still this software can be used for EDX quantification since a large set of routines that can be used for TEM are available using a library, called **EPQ** library, provided with the computer program and accessible using the Java programming language.

Finally it must be considered that Hyperspy is not, strictly speaking, an EDX analysis software but a framework for the analysis of EDX data using the python programming language. For this reason it does not provide a full-featured graphical user interface, and the experimenter must write his own python programs in order to analyze the data.

To illustrate the difference between the different programs the basic operation mode of an EDX data treatment will be discussed in the following. Some images, obtained with Esprit, will be used for each step to better illustrate the procedure. For each step the differences between the techniques used by each program will be discussed in order to assess their strengths and weaknesses. The discussion will be divided in two parts, corresponding to the main quantification steps: **measurement of peak intensity** and **quantification of specimen composition**.

Measurement of peak intensity

The quantification of a spectrum begins with the **identification of the elements**, and this is done graphically [23, 24]. The mechanism differs slightly from software to software but the general idea is that by selecting a peak on the spectrum (also called a line for historical reasons) all the elements that can be associated to that specific line are listed. It is up to the user to choose the element by inspecting the presence of the other lines associated to each characteristic peak family of the element. He must also pay attention to the possible presence of escape or sum peaks and to avoid identifying them as additional elements. The element can be considered as identified when all the characteristic peaks in the measurable energy window are present and the identified peaks can then be “tagged”. In the example of the Figure 1.10, Si and Ge can be identified because all the visible characteristic peaks are present in the spectrum.

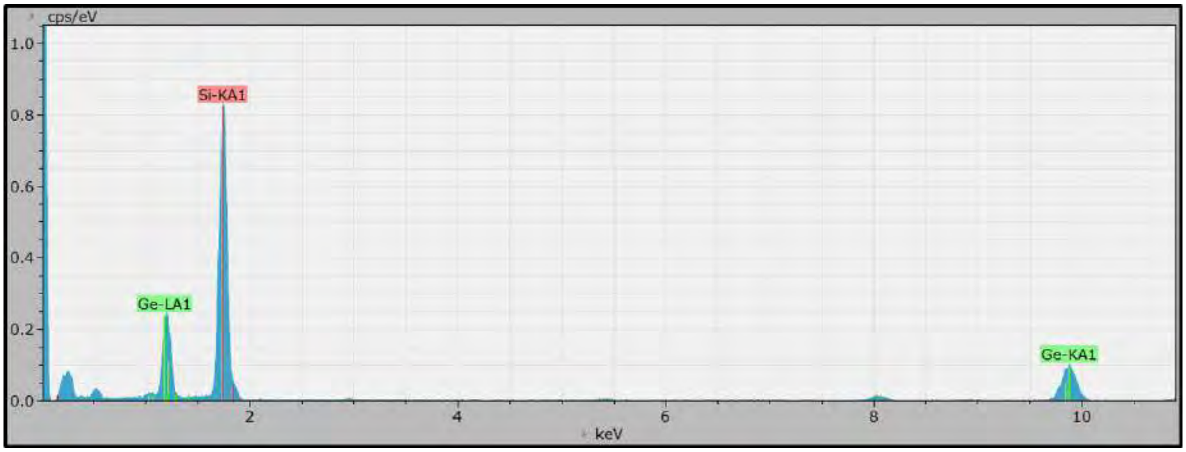

Figure 1.10: EDX spectrum obtained on a SiGe sample using the 2100F microscope installed at UMS Castaing.

For the **measurement of the selected peaks intensity** the **background noise** has to be subtracted, the possible **peak distortion** due to detector artifacts has to be taken into account and the **intensities of eventually overlapped peaks need to be separated**.

In all the fore-mentioned computer programs, **background (bremsstrahlung) subtraction** (see Figure 1.12) is handled by removing the regions where characteristic peaks are present in the spectrum and interpolating the spectrum background obtained after removal of the peak windows. The width of each characteristic peak window is calculated using equation 1.4 and the A coefficient is calculated using a reference peak (usually the $K\alpha$ peak of copper that is also used to assess the spectrometer resolution). Different interpolation functions are provided by the different applications.

It has to be noted that the precise algorithm used by commercial software is not always available. As a consequence, for commercial programs, it is not always possible to provide precise information and he following discussion will be based on the information available in the documentation or obtained using a series of comparative tests.

- In **Esprit** two models are available for TEM. The mathematical model (see 1.11(a)), that is a variation of the Kramer's model (the exact mathematical expression is not available) and the physical model that, in addition, takes into account the absorption of bremsstrahlung X-rays in the sample 1.11(b). The second model is therefore more precise and gives better results.1.11.
- Several models are provided by the **EPQ** library, based on papers by Lifshin[25], Reed[26] and Small [27]. The model used by default is a slightly modified version of the Lifshin model.
- No information is given on the model used by **Analysis Station.** Since the interpolated background has a continuous shape it can be supposed that an analytical

model based on Kramer's law is used and that absorption in the specimen is not taken into account.

- In **Hyperspy** the background shape can be obtained by averaging the intensity in two windows on each side of a X-ray line and using several standard interpolation functions (polynomial, spline ...).

It has to be noted that, even if the most complete approach is provided by **Esprit**, the bremsstrahlung interpolation procedure is only critical for low energy peaks, since in this region the noise is higher and the presence of several peaks due to contaminants (O, C, N, ...) are present (see again figure 1.11). For the quantification of characteristic peaks at higher energy no substantial difference is obtained using the different models.

The correction of **peak distortions** due to incomplete charge collection in the detector is only specifically provided by **Esprit**. But as already noted this kind of corrections can be safely avoided for modern SDD detectors.

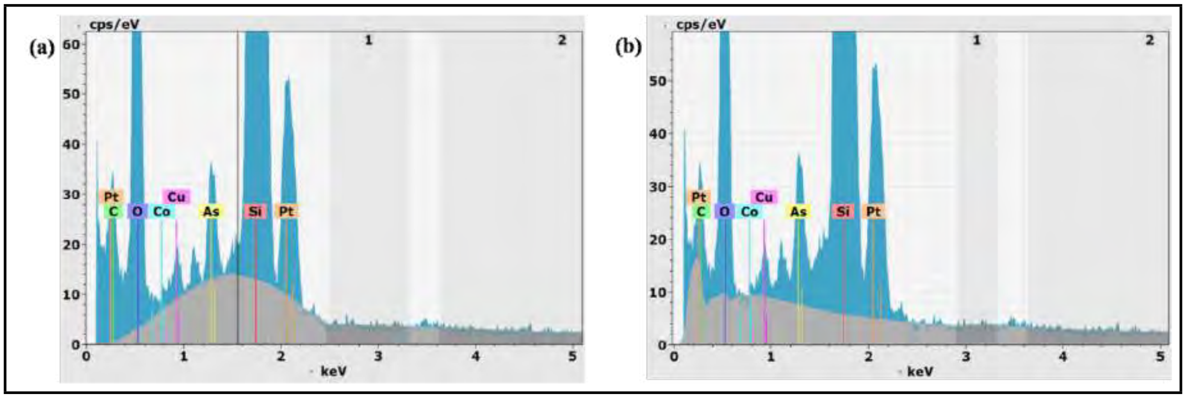

Figure 1.11: Diagram showing the two Bremsstrahlung elimination models: (a), Mathematical and (b), Physical TEM.

Finally to measure characteristic peak intensities and taking into account possible overlaps a **peak integration and deconvolution** procedure must be used [24]. It has to be noted that, as already mentioned, in all programs the calibrated information on peak width is available. The procedure of deconvolution consists in fitting a background subtracted spectrum with a series of Gaussian peaks of known width. This means that the adjustable parameters of the fit procedure are the Gaussian peak heights.

It has to be noted that the intensities of the different characteristic peaks forming the spectrum are not completely uncorrelated. For example, if no absorption is present, there is a fixed intensity ration between the different lines of the same characteristic peaks family that can be retrieved using the various X-ray emission cross sections. The main difference between the various deconvolution algorithms consists on how this correlation is handled.

In **Esprit** for example three approaches can be used:

- The spectrum is considered as a sum of independent Gaussian peaks. This is the most versatile approach since it can handle absorption effects but can be less precise in the case of small overlapping peaks.

- A constraint on the relative heights of lines of the same family is imposed. The relative heights of the peaks of the same series (K series, L series, etc.) are calculated by using the theoretical values of the cross-sections contained in the XCOM photon cross-section database[28]. This technique gives better results for small overlapping peaks.

- An approach based on a statistical iterative deconvolution technique called Bayes deconvolution, using no "a-priori" information [29]. In our tests this method has never given acceptable results.

The independent peak approximation is the most suited for our case, since specimen absorption can be present, and this algorithm is available in **Analysis Station** and **Hyperspy**, that additionally provides more advanced signal separations techniques based on principal component analysis [30]. **DTSA-II** and the **EPQ** libraries are mainly focused on quantification using standard specimens and reference spectra in SEM, and is less usable in our case.

In **summary,** commercial and free EDX programs provide different algorithms for the measurement of peak intensities. In general, the better results for all programs are obtained for high energy peaks (energy above 2 keV, since in this region background subtraction is easier) and neglecting peak intensity correlation (algorithms are more stable in this case, if absorption is present).

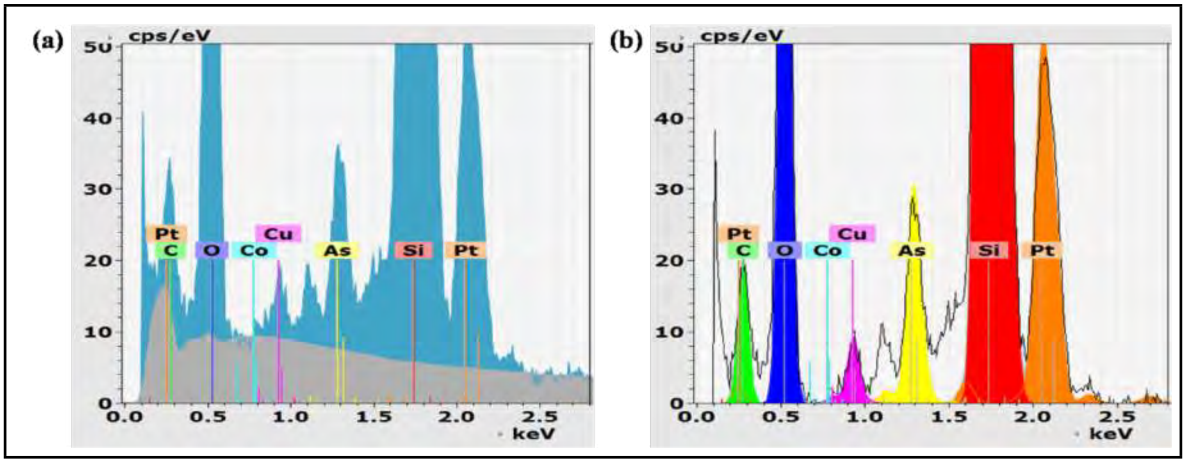

Figure 1.12: Example of subtraction of background noise (a) and deconvolution (b).

Quantification of specimen composition

Once the peak intensities have been measured, one of the techniques discussed in 1.3.1 must be used to extract information on the specimen composition. It has to be noted that all the fore-mentioned programs implement the C-L quantification method while the ζ-factor method is only implemented in **Hyperspy**.

As already explained, in order to avoid in-situ current measurement the C-L approach has been used for my work. Two main problems must be addressed when using with the C-L approach for quantitative mapping of nano-objects: the problem of **absorption** in the specimen and the problem of the **quantification** of the measurement error.

As already explained **specimen absorption** can modify the measured peak intensity. This modification must be taken into account in order to obtain an accurate value. When the C-L approach is used, all the fore-mentioned programs provide an absorption correction method (described in the next chapter), based on the knowledge of the specimen density. This means that the user is asked for the value of the specimen density in order to apply absorption correction. The problem is that in the vast majority of cases the specimen density is unknown since it depends on the specimen composition, and the specimen composition has to be determined using the EDX measurement. To solve this problem **a self-consistent approach**, described in the next chapter, has been developed.
In order to obtain a quantitative result, the accuracy of the C-L coefficients and the **associated experimental error** must be obtained. Moreover the different sources of experimental error must be combined to obtain the error on the final measurement. This feature ins not available in the fore-mentioned programs. The approach used in this thesis for the calibration of the C-L coefficients and the calculation of the final error will be described in the next chapter.

1.4 EDX and the other Quantification Techniques

It is interesting to compare EDX to the other characterization techniques that can be used to quantify the specimen composition.

As already mentioned, one of the most used techniques for chemical analysis in semiconductors is SIMS [31]. The SIMS technique is based on the analysis of the secondary ions sputtered when a (primary) ion beam is focused on the specimen. As described in the introduction the main advantage of this technique is its low detection limit (around 1 x10^{14} atoms/cm3). On the other hand,the lateral resolution of SIMS is about 0.2 μm and the depth resolution is in the order of 2 nm. For this reason the SIMS quantification technique can be easily used to obtain depth profiles on specimens with a multi-layered structures but cannot be used in modern nano-scaled 3D specimens.

Another important technique for composition measurement is Rutherford Backscattering Spectroscopy (RBS) [32]. RBS uses a beam of high energy (E~ 1MeV) He+

ions to obtain an absolute measurement of the composition of the specimen. Information on specimen composition is obtained by measuring the energy distribution of back-scattered He+ ions at a fixed angle. Like for SIMS, the lateral resolution of the technique prevents it to be used for composition profiling of modern 3D devices, and it is usually used to obtain depth concentration profiles. Nonetheless, it has to be noted that there is an important difference between RBS ans SIMS. RBS is an absolute technique: no calibration is needed in order to obtain a quantitative measurement.

For this reason this technique has be used in in this work to calibrate the C-L factors needed to obtain quantitative STEM/EDX measurements on calibration specimens (see chapter 2 and 3).

There is another technique worth mentioning for concentration measurement in nanoscale devices, that has the additional advantage of being able to obtain 3D information. This technique is called Atomic Probe Tomography (APT) [33] and is based on the extraction of atoms from a point-shaped specimen using the electric field (in non conducting specimens such as semiconductors, laser excitation is coupled to field effect). The analytic information and 3D distribution is obtained by using spatially resolved time of flight mass spectroscopy. The main reasons to prefer RBS to APT in this work are that the precision of the concentration measurement obtained by RBS is higher and that specimens to be measured by APT need a complicated specimen preparation (a point-like structure must be created using Focused Ion Beam techniques). Since STEM/EDX calibration can be performed on planar specimens, the 3D capability of APT was not needed in this work and RBS has thus been chosen to improve the precision of the calibration and avoid an additional specimen preparation step.

Chapter 2

Development of a new quantification method

As explained in the previous chapter, the available EDX software do not provide a rigorous approach to treat absorption correction using the C-L equation. Moreover, it is necessary, for quantitative measurements, to have an estimation of the measurement error and of the minimum density measurable by the technique (the technique detection limit). For this, a new quantification method based on the Cliff-Lorimer equation has been developed. The advantage of this approach when compared with other methods (see section 1.3.1) is that an in-situ current measurement is not needed. This kind of measurement need the presence of a Faraday cage, and this is not a standard equipment in commercially available microscopes. As a consequence, this method can be applied in a standard microscope, without any need for special equipment.

In this chapter, we will describe the absorption correction problem and justify the need of a self-consistent method. Then, we will detail the procedure used for the calibration of C-L factors and for the estimation of the error in the final measurement.

2.1 Mass fractions and density calculation

As already discussed (see section 1.3.1 and equation 1.5) the C-L approach is based on a proportionality relation between peak intensities and the elements mass fractions. The proportionality constant $K_{i,j:F_i,F_J}$ is the Cliff-Lorimer factor relative to the i$^{\text{th}}$ and j$^{\text{th}}$ element, it depends on the peak families F_i and F_j that have been chosen for each element. In the vast majority of commercial software, the C-L constants values are extracted from a simulated database.

It can be shown that the C-L coefficients can be also written as follows:

$$K_{i,j:F_i,F_J} = \frac{k_{i:F_i,F_{i_0}}}{k_{j:F_j,F_{i_0}}} \tag{2.1}$$

where $k_{i:F_i,F_{i_0}}$ is the C-L coefficient relative to the element i and a common reference element i_0. It has to be noted that, by definition, the reference element has a unitary C-L coefficient ($k_{i_0:F_{i_0},F_{i_0}} = 1$) and F_{i_0} denotes the peak family that has been chosen for the reference element. With this convention it can be shown that there is a direct formula relating measured intensities and the mass fractions for a material composed of N_A different atoms :

$$f_i^M = \frac{k_{i:F_i,F_{i_0}} I_{i:F_i}}{\sum_{j=1}^{N_A} k_{j:F_j,F_{i_0}} I_{j:F_j}} \tag{2.2}$$

The total intensity $I_{i:F_i}$of the family F_i for a specific element is obtained by adding the intensity of the N_{F_i} lines ($K\alpha$, $K\beta$...) belonging to the family chosen for the element i.

$$I_{i:F_i} = \sum_{k=1}^{N_{F_i}} I_{i:F_i,k} \tag{2.3}$$

Following this notation each characteristic peak line has an intensity given by $I_{i:F_i,k}$ and is associated to the energy $E_{i:F_i,k}$ where i identify the element F_i the peak family and k the index identifying the peak line.

It should also be noted that the intensities to be used in the formula correspond to the integral of the characteristic peaks, to which must be added the intensity of the X-rays which are shifted in other regions of the spectrum (in the peaks "sum" or "escape", in the "tail", in the "shelf"...) because of measurement artifacts. All the previously described effects must therefore be taken into account for the application of this formula. Moreover, for a correct interpretation of the results, the absorption effects in the sample must be taken into account because they are neglected in the C-L model. Finally, it should be noted that the coefficients of C-L are normally calculated using simplified models and they must be calibrated in the case where results with a controlled precision are needed. They must therefore be considered as empirical parameters with an associated measurement error.

Even if it is easy to calculate mass fractions from EDX measurements, it can be useful (and customary, in semiconductor literature on doping) to use atomic concentrations (in atoms/cm^3) instead of mass fractions. The conversion between mass fractions and atomic concentrations c_i^A can be obtained using the following formula:

$$c_i^A = \frac{\rho^M f_i^M}{m_i} N_{AV} \tag{2.4}$$

where ρ^M is the mass density of the element i, m_i its atomic mass and $N_{AV} = 6,02214076 \cdot 10^{23} mol^{-1}$ is the Avogadro number.

Another quantity conventionally used to express concentration is the mass fractions. This is used, for example, for binary alloys (composed by the elements A and B) whose chemical formula is normally expressed as $A_{1-x}B_x$ where x is the atomic fraction of

B. The mass fractions relative to a series of elements (f_i^A) can be calculated from the corresponding mass fractions using the following formula:

$$f_i^A = \frac{f_i^M / m_i}{\sum_{j=1}^{N_{AT}} f_j^M / m_j} \tag{2.5}$$

2.2 Absorption Correction

To quantify an EDX spectrum, the intensities of the various peaks are measured. But since the measured X-rays pass through the specimen before reaching the detector the measured intensity of X-rays I^* can be different of the emitted intensity I. This effect need to be taken into account to obtain reliable results. The following formula can be used to calculate the measured intensity $I^*(E)$ of X-rays of energy E going through a **homogeneous** material of thickness z and mass density ρ^M([3] p.654):

$$I^* (E) = I (E) e^{-\mu(E)\rho^M z} \tag{2.6}$$

where $\mu(E)$ is the mass absorption coefficient of the material, $I(E)$ is the initial X-ray intensity and $I^*(E)$ is the intensity measured by the detector after absorption in the specimen.

This formula can be obtained under the hypothesis that X-rays emission is uniform in depth. This means that for a specimen of thickness t the emission density is constant and its value is equal to $\frac{I(E)}{t}$. X-rays are all emitted with the same probability, but the distance they go through in the specimen before reaching the detector depends on the emission depth. Using equation 2.6 we obtain:

$$I^* (E) = \int_0^t \frac{I (E)}{t} e^{-\mu(E)\rho^M z} dz = \frac{1 - e^{-\mu(E)\rho^M t}}{\mu \rho_M t} I (E) \tag{2.7}$$

Therefore we can define a transmission coefficient which relating the intensity of emitted rays $I(E)$ with that measured by the detector$I^*(E)$:

$$T(E, \{f_i^M\}) = \frac{1 - e^{-\mu(E)\rho^M t/\sin(\alpha)}}{\mu \rho_M t/\sin(\alpha)} \tag{2.8}$$

The transmission factor depends on the X-ray energy and on the mass fractions $\{f_i^M\}$ of the different elements since both $\mu(E)$ and ρ^Mdepends on the mass fractions (for this reason they will be noted as $\mu\left(E, \{f_i^M\}\right)$ and $\rho^M\left(\{f_i^M\}\right)$ in the following). α is the elevation angle of the detector (see figure 2.1)

There is no universal formula connecting the density of a material to the mass fractions of the atoms composing it, since the density obviously depends on the atomic arrangement of the composing atoms. As a consequence the analytical expression of $\rho^M\left(\{f_i^M\}\right)$ depends on the specimen.

On the other hand there is a universal formula for $\mu(E)$ ([3] p.654, [34]):

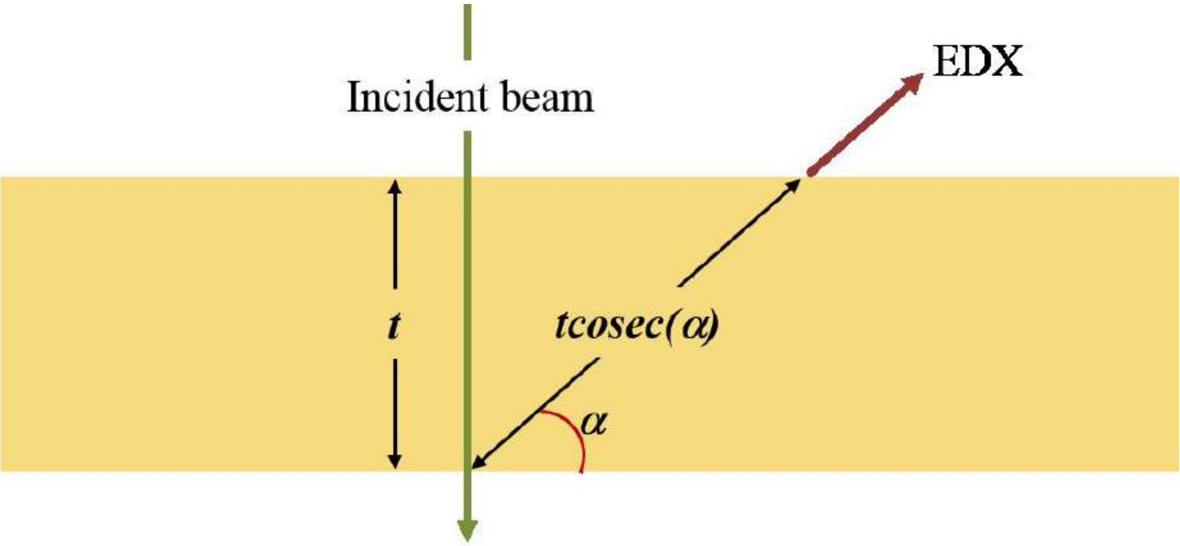

Figure 2.1: Schematic diagram of the absorption geometry in a homogeneous material.

$$\mu\left(E,\left\{f_i^M\right\}\right)=\sum_{i=1}^{N_{AT}}\mu_i\left(E\right)f_i^M \tag{2.9}$$

where $\mu_i(E)$ is the mass absorption coefficient associated to the $\mathrm{i^{th}}$ atom.

This relation is normally cited in literature without any proof of reference. It is hence hard to ascertain its limit of validity. For this reason a proof of equation and the underlying approximations needed to obtain it will be given here. Using the total interaction cross sections$\sigma_i(E)$ for an X-ray of energy E with an atom of an element i we can write [35]:

$$\mu_i=\frac{\sigma_i}{m_i} \tag{2.10}$$

Equation 2.9 can then be obtained by making the hypothesis that the cross section of a mixture of atoms is the sum of the cross sections of the individual atoms. This means that the contribution of the bonding between atoms does not affect their interaction with X-rays. This is a good approximation since it is used in many other calculations (characteristic X-ray energies and relative intensities for example). Supposing that the cross sections are additive and that the number of atoms of type i in the alloy is n_i, we can write:

$$\mu(E)=\frac{\sum_{i=1}^{N_{AT}}n_i\sigma_i}{\sum_{j=1}^{N_{AT}}n_jm_j}=\sum_{i=1}^{N_{AT}}\left(\frac{\sigma_i}{m_i}\frac{n_im_i}{\sum_{j=1}^{N_{AT}}n_jm_j}\right) \tag{2.11}$$

and this equation is equivalent to equation 2.9 since $\mu_i = \sigma_i / m_i$ and by definition $f_i^M = n_i m_i / \sum_{j=1}^{N_{AT}} n_j m_j$.

The value of $\mu_i(E)$ for the various elements can be obtained using one of the several available tabulated values collections (see for example [36] and [37]). In our case they have been calculated using the EPQ library implementation of the model proposed by Heinrich [37].

For each characteristic peak $E_{i:F_i,k}$ the intensities $I_{i:F_i,k}$ can be calculated from the measured intensities $I^*_{i:F_i,k}$ using equation 2.8. If the sample is homogeneous and $\mu\left(E, \left\{f_i^M\right\}\right)$ and $\rho^M\left(\left\{f_i^M\right\}\right)$ are known, equation 2.8 and equation 2.9 can be used to calculate the mass fractions of the values elements. This is the approach normally used by commercial software. The specimen is assumed to be homogeneous, the user is asked for the value of the specimen density and the mass absorption coefficients are evaluated applying equation 2.9 to the mass fractions calculated without taking into account the absorption effects. The main improvements of our approach to take into account specimen absorption are:

- First of all, we have developed an iterative approach to overcome the limitation of the existing algorithms. More details on the algorithm we have used are given in the section 2.2.
- In addition we have taken into account that the specimen is not homogeneous. This difficulty can be solved for specimen with a 1D geometry, such as those observed in my thesis, by carefully choosing the specimen orientation in the microscope. If the specimen is oriented as in Figure 2.2 and we consider that the detector size is negligible, we can consider that the X-rays are going through a homogeneous slice to reach the detector. In this case equation 2.8 holds for each slice but μ and ρ^M can't be considered as constant since their value varies from slice to slice (see again Figure 2.2). For this reason, from now on, we will explicitly indicate dependence on the x (depth) coordinate of the various quantities in the following ($f_i^M(x)$, $\mu\left(x, E, \left\{f_i^M(x)\right\}\right)$, $\rho^M\left(x, \left\{f_i^M(x)\right\}\right)$ ...).

To take into account specimen absorption, an iterative approach is needed since to calculate the mass fraction $\left\{f_i^M(x)\right\}$ at each position x of the profile, we need the value of the transmission factor T which depends on $\left\{f_i^M(x)\right\}$ (see equation 2.8). For the iterative procedure we use as a starting point the mass fractions $\left\{\left[f_i^M(x)\right]_0\right\}$ calculated by neglecting absorption (i.e. by assuming that $I^*_{i:F_i,k}(x) = I_{i:F_i,k}(x)$) for all the characteristic peaks. For each iteration, a new set of mass fractions is obtained by calculating the transmission factor using the values obtained in the previous iteration:

$$\begin{aligned}
\left[T_{i:F_i,k}(x)\right]_n &= T(x, E_{i:F_i,k}, \left\{\left[f_i^M(x)\right]_n\right\} \\
&= \frac{1 - e^{-\sum_{j=1}^{N_A} \mu_i\left(E_{j:F_j,k}\right)\left[f_j^M(x)\right]_{n-1}\rho^M(x, \left\{\left[f_i^M(x)\right]_{n-1}\right\}t/\sin(\alpha)}}{\sum_{j=1}^{N_A} \mu_j\left(E_{j:F_j,k}\right) f_j^M \rho^M(x, \left\{\left[f_i^M(x)\right]_{n-1}\right\} t/\sin(\alpha)}
\end{aligned} \tag{2.12}$$

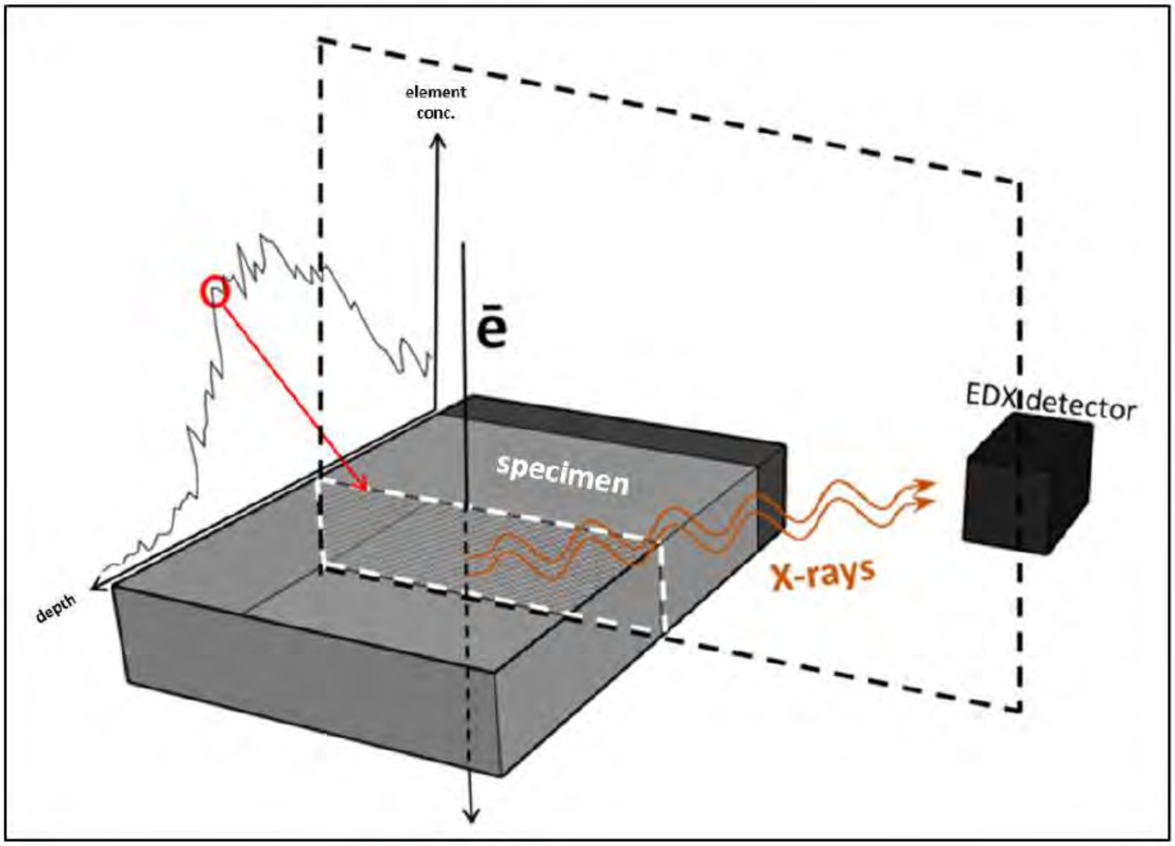

Figure 2.2: Schematic illustration of the detector position and of X-ray path, when the detector is placed on a plane perpendicular to the variation direction of the doping profile.

and the new values of the absorbed intensities and the corresponding absorption corrected mass fractions are evaluated as follows :

$$[I_{i:F_i,k}]_n = \frac{I^*_{i:F_i,k}}{[T_{i:F_i,k}(x)]_n} \tag{2.13}$$

Since:

$$[I_{i:F_i}]_n = \sum_{k=1}^{N_{F_i}} [I_{i:F_i,k}]_n \tag{2.14}$$

we can write :

$$[f_i^M]_n = \frac{k_{i,F_i,F_{i_0}} * [I_{i:F_i}]_n}{\sum_{j=1}^{N_A} k_{j,Fj_i,F_{i_0}} * [I_{j:F_j}]_n} \tag{2.15}$$

The final values $\widetilde{I}_{i:F_i,k}(x)$ and $\widetilde{f}_i^A(x)$ are obtained after N_I iterations, the stopping criterion being that the relative variation of the mass fractions between two subsequent iterations is below a fixed tolerance ($\frac{\left|\left(f_i^M\right)_n-\left(f_i^M\right)_{n-1}\right|}{\left(f_i^M\right)_n} < \epsilon$).

As already discussed, the relation between the specimen local mass density $\rho^M(x)$, and the local elements mass fractions $f_A^M(x)$ and $f_B^M(x)$ must be known to apply the iterative procedure. This expression depends on the specimen structure and will be discussed, for different materials, in the next paragraph 2.3.

2.3 Mass density calculation

The relation between the specimen local mass density $\rho^M(x)$ and the local mass fractions $f_i^M(x)$ of the atoms forming the material can be, in general, quite complicated. In these section we will discuss some simple approximations that can be used in three cases of interest for the study of semiconductors:

- The case of doped crystalline specimens
- The case of amorphous alloys (that can be obtained for example by implanting a crystalline specimen with a high dose impurity)
- The case of pseudomorphic alloys (such as for example the SiGe alloy).

2.3.1 Doped crystalline materials and the “same radius” approximation.

In an ideal doped crystalline material, we can consider that a small fractions of the substrate atoms (labeled by 1) are replaced by a dopant atom (labeled by 2). This is equivalent to say that all the doping atoms are in substitution. Since the doping atoms are in small concentration the mass density can be easily calculated starting from the mass density of the substrate $\rho_1^M(x)$ and evaluating the mass difference obtained when a dopant atom replaces a substrate atom.

$$\rho^M(x) = \rho_1^M\left[f_1^A(x) + \frac{m_2}{m_1}f_2^A(x)\right] = \rho_1^M\left[1 + \left(\frac{m_2}{m_1} - 1\right)f_2^A(x)\right] \tag{2.16}$$

where $f_i^A(x)$ are the atomic fractions for the two elements, related, in a binary alloy, by the following equation $f_1^A(x) = 1 - f_2^A(x)$.

The atomic fractions for the element can be calculated from the mass fractions using equation 2.5.

In the case of two elements, this formula simplifies to:

$$\begin{aligned} f_1^A(x) &= 1 - f_2^A(x) \\ f_2^A(x) &= \frac{f_2^M(x)}{f_2^M(x) + \frac{m_2}{m_1} f_1^M} = \frac{f_2^M(x)}{f_2^M(x) + \frac{m_2}{m_1}\left(1 - f_2^M(x)\right)} \end{aligned} \tag{2.17}$$

and equation 2.16 can be written as:

$$\rho^M(x) = \rho_1^M \left[1 + \frac{(m_1 - m_2)\, f_2^M(x)}{m_1 - (m_1 - m_2) f_2^M(x)} \right] \tag{2.18}$$

This is the formula we will looking for since it relates the mass density to the mass fractions. Since in this approximation it is assumed that the dopant atom causes no deformation, we will refer to it as the "same radius approximation" since it is equivalent to consider that the doping atoms an the substrate atoms have exactly the same radius.

2.3.2 Amorphous solids and the "amorphous solid approximation"

A better approximation can be obtained by using a formula that has been originally derived for solids that do not present any kind of ordering (also known as ideal amorphous solids (IAS)) [38]:

$$\rho^M = \sum_{i=1}^{N_{AT}} \rho_i^M f_i^V \tag{2.19}$$

where ρ_i^M is the mass density of an amorphous amorphous solid composed exclusively by atoms of the i element and f_i^V is the volume fraction of the same elements in the alloy. We will refer to this approximation in the following as the "amorphous solid approximation". The main hypothesis behind the derivation of this formula is that the space occupied in the solid by an atom of a specific element is always the same in any alloy, in the sense that it does not depend on the alloy concentration. Another way to express the same approximation is to say that the structure around a specific kind of atom in the alloy does not depend on the alloy concentration. This requirement is obviously fulfilled for IASs since in this case the atomic distribution is fully random and does not depend on the concentration of the two elements in the alloy. The space around an individual atom just depends on the "size" of the atom that can be estimated using its covalent radius.

Equation 2.19 can also be used in solids that have not an IAS structure provided the fore-mentioned approximations holds. An example of its application to amorphous solid that do not have an IAS structure will be given in section 3.1.3.

To establish a relation between the alloy mass density and the mass fractions the following formula can be used to calculate the volume fractions from the mass fractions (this formula can be obtained under the same assumptions of equation 2.19):

$$f_i^V = \frac{\frac{f_i^M}{\rho_i^M}}{\sum_{j=1}^{N_{AT}} \frac{f_j^M}{\rho_j^M}} \tag{2.20}$$

Inserting equation 2.20 into equation 2.19 and considering that the mass fractions are normalized to 1 ($\sum_{j=1}^{N_{AT}} f_j^M{=}1$) we obtain the amorphous mass density equation:

$$\rho^M = \frac{1}{\sum_{j=1}^{N_{AT}} \frac{f_j^M}{\rho_j^M}} \tag{2.21}$$

2.3.3 Pseudomorphic alloys

It is interesting, to better understand the “perfect amorphous” approximation, to calculate the density of pseudomorphic alloys. Pseudomorphic alloys are binary alloys composed by two elements (Si and Ge for example) that have exactly the same crystalline structure in their pure form (Si an Ge both have a cubic structure of type diamond). The element A will identified by the index 1 and the element B by the index 2. We will also indicate with x the atomic fraction $f_2^A$of the second element so that $f_1^A = 1 - x$ and the alloy chemical formula will have the form$A_{1-x}B_x$. In a pseudomorphic alloy the two lattices have a very close lattice parameter (lattice parameter is 0.227 Angstrom larger in Ge than in Si) and the binary alloy retains the same structure of the pure elements (SiGe has a diamond structure). The lattice parameter of the alloy follow Vegard’s law[39, 40]:

$$a_{A_{1-x}B_x} = a_1(1-x) + a_2 x \tag{2.22}$$

where $a_i$is the lattice parameters of the crystals formed by a pure element.

Using Vegard’s law the mass density of a $A_{1-x}B_x$ alloy can be calculated by considering that a unit cell contains, in total n atoms: $n(1-x)$ of type A and nx of type B:

$$\rho^M = n\frac{m_1(1-x) + m_2 x}{[a_1(1-x) + a_2 x]^3} \tag{2.23}$$

The final expression can then be obtained by transforming the atomic fractions x and $(1-x)$ into mass fraction. We will not derive this formula because it can be shown that for this case, the “amorphous solid approximation” can be used. This seems paradoxical since in this case the alloy is not at all amorphous. But in fact it is easy to understand that in this case it is a good approximation to suppose that the volume occupied by a A or B atom in the $A_{1-x}B_x$ alloy does not depend on x. This derives from the fact that in the pure crystal an atom of type A occupies a volume $V_1^A = \frac{a_1^3}{n}$ (atomic volume)

where n is, again, the number of atoms per unit cell. In the same way $V_2^A = \frac{a_2^3}{n}$ since the two atoms have exactly the same crystalline structure and the number of atom per unit cell n is the same. Since a_1 and a_2 have a close value, the values of V_1^A and V_2^A are also close and we can expect that the atomic volume does not have a strong variation. As a consequence it is a good approximation to suppose that the atomic volumes of the two atoms are almost constant in the alloy and the "amorphous solid approximation" can be applied.
This can be shown in a rigorous way by comparing the exact result (equation 2.23) with the result that is obtained using the "amorphous solid approximation". In this case in the volume occupied by $n(1-x)$ atoms is of type A is $V_1 = n(1-x)V_1^A$, the volume occupied by atoms of type B is $V_2 = nxV_2^A$ and the total volume is $V = V_1 + V_2$. The density in this approximation is given by equation 2.19.

Taking into the account that we have $f_i^V = V_i/V$, and that for a crystalline solid with n atoms per unit cell $\rho_i^M = \frac{nm_i}{a_i^3}$ we can write:

$$\begin{aligned}\rho^M =& \frac{\rho_1^M n(1-x)V_1^A + \rho_2^M nxV_2^A}{n(1-x)V_1^A + nxV_2^A} \\ =& \frac{\frac{nm_1}{a_1^3} n(1-x)\frac{a_1^3}{n} + \frac{nm_2}{a_2^3} nx\frac{a_2^3}{n}}{n(1-x)\frac{a_1^3}{n} + nx\frac{a_2^3}{n}} \\ =& n\frac{m_1(1-x) + m_2 x}{a_1^3 + x(a_2^3 - a_1^3)}\end{aligned} \tag{2.24}$$

Expressions 2.23 and 2.24 are obviously different,. But it can be shown that they are approximately the same for a pseudomorphic alloy. For that we can express both denominators using the parameter $\varepsilon = \frac{a_2 - a_1}{a_2}$ that can be considered to be small ($\epsilon = 4.2\%$ in SiGe). For the denominator of equation we can write 2.23:

$$\begin{aligned}\left[a_1(1-x) + a_2 x\right]^3 =& \\ &= a_1^3\left[1 + \epsilon x\right]^3 \\ &= a_1^3\left[1 + 3\epsilon x + 3\left(\epsilon x\right)^2 + \left(\epsilon x\right)^3\right] \\ &= a_1^3\left[1 + 3\epsilon x + O\left(\epsilon^2\right)\right]\end{aligned} \tag{2.25}$$

while for the denominator of equation 2.24 it can be shown that :

$$\begin{aligned}a_1^3 + x(a_2^3 - a_1^3) =& \\ &= a_1^3 + x\left[a_1^3(1+\varepsilon)^3 - a_1^3\right] \\ &= a_1^3\left[1 + 3\varepsilon x + 3\varepsilon^2 x + \varepsilon^3 x\right] \\ &= a_1^3\left[1 + 3\varepsilon x + O\left(\epsilon^2\right)\right]\end{aligned} \tag{2.26}$$

It can be noted that the two expressions are equal up to the first order and the "amorphous solid approximation" is indeed a good approximation for pseudomorphic alloys.

2.4 Model calibration and error estimation

As already discussed, in order to be able to obtain a reliable measurement, the C-L coefficients must be calibrated. In addition, in order to obtain a quantitative measurement the error on the calibrated coefficient must be estimated, and the error on the final composition measurement calculated by combining all the possible source of errors. The procedure and formulas we have used for calibration and error estimation will be discussed in this section. A direct application of these techniques using Rutherford Backscattered Spectroscopy "RBS" [32] for the calibration will be given in chapter 3.

In the general case of an alloy composed by N_{AT} atoms, all the $k_{i:F_i,F_{i_0}}$ C-F coefficients relative to the reference element $i_0$must be calibrated.

The general technique for the calibration and the error estimation of the error of the C-L coefficient relative to two elements i and i_0 for the peak families F_i and F_{i_0} will be explained in the following. This procedure must be applied on two peaks at a time until the full set of C-L coefficients is obtained. Several calibration specimens can be used, the only requirement is that using the specimen a measurement $\left[f_i^M(x)\right]_{Meas}$ of the mass fractions can be obtained with an experimental technique different from EDX. For two elements i and i_0 the C-L factors relative to the peak families F_i can be obtained by linear regression starting from the following formula (see equation 1.5 and 2.1):

$$k_{i:F_i,F_j}\frac{\widetilde{I}_{i:F_i}(x)}{\widetilde{I}_{i_0:F_{i_0}}(x)}=\frac{\left[f_i^M(x)\right]_{Meas}}{\left[f_{i_0}^M(x)\right]_{Meas}} \tag{2.27}$$

To estimate the error on $\Delta k_{As:F_{As}}$ on the calibrated value of $k_{As:F_{As},F_{Si}}$ we have assumed that the statistical distribution of the measured intensities follow Poisson law. In this case the error on the measurement of the intensity I is given by $\Delta I(x)=\sqrt{I(x)}$ and the relative error is given by $\epsilon_I=\frac{\Delta I}{I}=\frac{1}{\sqrt{I}}$.The best fit value for $k_{i:F_i,F_j}$ can be obtained by using the weighted least squares techniques and minimizing the expression ([41] p.75):

$$R=\sum_k \frac{1}{w(x_k)}\left[\frac{\left[f_i^M(x)\right]_{Meas}}{\left[f_{i_0}^M(x)\right]_{Meas}}-k_{i:F_i,F_{i_0}}\frac{\widetilde{I}_{i:F_i}(x_k)}{\widetilde{I}_{i_0:F_{i_0}}(x_k)}\right]^2 \tag{2.28}$$

where $\{x_k\}$ is the set of positions where the densities have been experimentally measured. In order to favor the most precise points the weighting factors $w(x_i)$ have been chosen to be equal to the relative experimental error associated to $\frac{\widetilde{I}_{As:F_{As}}(x_i)}{\widetilde{I}_{Si:F_{Si}}(x_i)}$.

By using error propagation laws we can then write $w(x_k)=\sum_{i=1}^{N_{AT}}\frac{1}{\sqrt{\widetilde{I}_{i:F_l}(x_i)}}$.

The best fit value of $k_{As:F_{As}}$ and the associated statistical error $\Delta k_{As:F_{As}}$have been calculated using the standard formula for parameter error estimation in weighted least square regression ([41],[42]).

When performing a quantitative measurement, it is of course important to evaluate the total measurement error. In the case of a concentration measurement carried out by EDX using the calibrated value of the C-L coefficients three kind of errors must be taken into account:

1. The fore-mentioned statistical error on the measured intensities $\Delta I(x) = \sqrt{I(x)}$. The contribution of this error to the mass fraction can be calculated, using standard error propagation techniques [42], to be:

$$\begin{aligned} \Delta_I f_i^M(x) &= \frac{k_{i:F_i,F_{i0}}}{\left[\sum_{j=1}^{N_{AT}} k_{j:F_j,F_{i0}} I_{j:F_j}(x)\right]^2} \times \\ &\quad \sum_{j\neq i} \left[k_{j:F_j,F_{i0}} \left(I_{j:F_j}(x)\Delta I_{i:F_i} + I_{i:F_i}(x)\Delta I_{j:F_j}(x)\right)\right] \end{aligned} \tag{2.29}$$

   where $\sum_{i\neq j}$ indicates the sum over all atoms except the i atom.

2. The errors $\Delta k_{j:F_j,F_{i0}}$ on the calibrated value of the CL constant. The contribution of this error can be calculated to be :

$$\begin{aligned} \Delta_k f_i^M &= \frac{I_{i:F_i,F_{i0}}}{\left[\sum_{j=1}^{N_{AT}} k_{j:F_j,F_{i0}} I_{j:F_j}(x)\right]^2} \times \\ &\quad \sum_{j\neq i} \left[I_{j:F_j}(x) \left(k_{j:F_j,F_{i0}}\Delta k_{i:F_i,F_{i0}} + k_{i:F_i,F_{i0}}\Delta k_{j:F_j,F_{i0}}\right)\right] \end{aligned} \tag{2.30}$$

3. The experimental error on the specimen thickness Δt. In this case it is not possible to apply the error propagation formula to evaluate the error since the dependence of $f_j^M(x)$ on t is given by the previously discussed iterative calculation. In this case the contribution to the total error has been estimated using the following formula $\Delta_t f_i^M(x) = \frac{\left|\left[f_i^M(x)\right]_{t+\Delta t} - \left[f_i^M(x)\right]_{t-\Delta t}\right|}{2}$ where $\left[f_i^M(x)\right]_t$ is the density calculated for a thickness t.

Assuming that the error on k and the error on the intensities are statistically dependent (the same detector is used for the calibration and the measurements) and that the error on the thickness is statistically independent of the other errors we can obtain the expression of the total error :

$$\Delta f_i^M(x) = \sqrt{\left[\Delta_I f_i^M(x) + \Delta_k f_i^M(x)\right]^2 + \left[\Delta_t f_i^M(x)\right]^2} \tag{2.31}$$

As already noted, even if mass fractions are easier to calculate from EDX measurements, it in some occasions better to use the atomic concentration. To evaluate the error on the atomic concentrations $c_i^A(x)$, equation 2.4 can be used. The obtained result is :

$$\Delta c_i^A(x) = \frac{N_{AV}}{m_i}\left(\sum_{j=1}^{N_{AT}}\left|\frac{\partial\left(\Delta\rho^M\right)}{\partial f_j^M}\right|\Delta f_j^M + \rho^M \Delta f_i^M\right) \tag{2.32}$$

The precise formula depends on the formula used for ρ^M. We can the estimate the error for the two mass density approximation discussed in section 2.3.
For the **"constant radius approximation"** the following formula is obtained:

$$\begin{aligned} \Delta c_2^A(x) = & \frac{N_{AV}}{m_j}\rho_1^M\left[1+\frac{(m_1-m_2)\, f_2^M(x)}{m_1-(m_1-m_2)f_2^M(x)}\right]\times \\ & \times\left\{1+\frac{m_2(m_2-m_1)}{\left[m_2-(m_2-m_1)f_2^M(x)\right]^2}f_2^M(x)\right\}\Delta f_2^M(x) \end{aligned} \tag{2.33}$$

while for the **"amorphous solid approximation"** we have:

$$\Delta c_i^A(x) = \frac{N_{AV}}{m_{As}}\frac{1}{\sum_{k=1}^{N_{AT}}\frac{f_k^M}{\rho_k^M}}\left\{\Delta f_i^M(x)+\frac{1}{\sum_{k=1}^{N_{AT}}\frac{f_k^M}{\rho_k^M}}\sum_{j=1}^{N_{AT}}\frac{\Delta f_j^M(x)}{\rho_j^M}\right\} \tag{2.34}$$

As already discussed, it is conventional, for binary alloys, to use the atomic fractions instead of the mass fractions. In this case the error on the mass fractions can be calculated applying error propagation formula on equation 2.5. The obtained expression for the error on the atomic fractions is:

$$\begin{aligned} \Delta f_i^A = & \frac{1/m_i}{\left[\sum_{j=1}^{N_{AT}} f_j^M/m_j\right]^2}\times \\ & \sum_{j\neq i}\left[1/m_j\left(f_j^M\Delta f_i^M + f_i^M\Delta f_j^M\right)\right] \end{aligned} \tag{2.35}$$

2.5 Discussion and conclusions

In this chapter we propose a new quantification technique taking into account the absorption in the specimen with a self-consistent method and including model calibration for error estimation. The critical point for the model application is to establish a relation between the mass density and the specimen composition. For, this two approximations have been proposed.

It will be demonstrated in the following chapter that these two approximation can be successfully applied to obtain quantitative concentration measurements in amorphous and crystalline semiconductors.

To conclude this chapter, in this section we will compare the model we have developed with other existing methods and discuss how it can be applied to materials different from the ones discussed in the next chapter.

2.5.1 Comparison with other models

As already stated, the main novelties of this new approach are the use of RBS data to calibrate the k-factors and that the specimen local density has been calculated using physical models. The knowledge of the local density is used to correct the absorption effects without any in situ measurement of the electron beam current, which is an advantage with respect to other techniques such as the ζ-factor method or the cross-section method (see section 1.3.1).

This being said, other techniques have been proposed in the past that do not require any current measurement and yet can be used to correct absorption. We can cite, for example, the techniques proposed by Morris et al. [43] and Qiu et al. [44], where the difference in absorption between **different peaks** is used to deduce the specimen thickness. Another approach uses measurements performed at **different tilt angles** (see again Morris et al. [43]) to estimate the specimen thickness.

Concerning the technique using different peaks to obtain information on the thickness, it must be noted that it can only be applied to specific materials. To be applicable, two main peaks of the substrate must be measurable and their characteristic energy must be big enough for the difference in absorption to be measurable. This technique is, for example, not applicable in pure silicon substrates since at at the energy commonly used in TEM (~100 kV), just one characteristic peak (the SiK peak) can be measured.

Some limitations also apply to the technique using several tilt angles. First of all the specimen must be reasonably flat (but this also apply to our model since a fixed specimen values is used in the calculations). Moreover the difference in tilt angles must be high enough for absorption effect to vary, and this is problematic in modern microscopes. In high resolutions microscopes the maximum tilt angle can be limited by the small objective lens pole-pieces gap, and in analytical microscopes equipped with large EDX detectors, shadowing effects can appear at small tilt angles.

To our knowledge, the idea of using RBS to calibrate the C-L coefficients and error propagation to estimate the measurement error has never been used before. This is an original feature of the model proposed here.

The main disadvantage of our model when compared with techniques such as ζ-factor method, is that a density model to be used depends on the specimen and must be established while in the ζ-factor method, the additional information provided by the in-situ current measurement can be used to measure thickness and density at the same time.

2.5.2 Model applicability

As already discussed, the establishment of a density formula is the main drawback of our model and it is the important to understand in which cases the approximations discussed in 2.3 can be used.

If we focus on the case in which only two elements are present (binary alloys), there are three categories of materials for which it is simple to establish a density model:

- Alloys composed by atoms of comparable "size" (covalent radius) in which one of the two atoms is in small concentration. In this case the same-radius approximation can be used. Interesting cases included in this category are some doped semiconductors, Si:B, Si:P, Si:Al, Si:As but also metallic alloys provided the two fore-mentioned conditions are satisfied (low concentration iron alloys such as FeCo, FeNi, FeCu ...).
- Pseudo-morphic alloys (see 2.3.3) like SiGe, CuPd, AgAu...
- Alloys presenting no local ordering (ideal amorphous solid see section 2.3.2). It will be shown in section 3.1.3 that binary alloys composed by elements having the same packing ratio fall in this category.

The model presented in this chapter can, in principle, also be applied, to alloys composed by more than two elements, or alloys with a known phase-diagram provided that the density in each domain can be calculated using one of the fore-mentioned approximations. This being said, in cases in which the development of a density model becomes too complicated (because of the presence of several elements or several phases in the alloy phase-diagram) the ζ-factor method must be preferred.

Chapter 3

Quantitative EDX mapping in semiconductors

As already discussed in the introduction, Elemental mapping at the nanoscale is a particularly critical issue for semiconductor devices. The emergence of devices based on ultra-shallow junctions or 3D geometries has created a demand on new techniques since standard techniques such as Secondary Ion Mass Spectroscopy cannot be used on new generation devices.

The quantification model described in the previous chapter has specifically been developed to obtain quantitative concentration measurements by STEM/EDX and can be used for composition profiling in semiconductor nanodevices.

In this chapter two applications will be described:

- The measurement of low concentration impurities in a Si nanodevice structure.
- The measurement of Ge concentration in a SiGe nanostructure.

The discussion will include, for each application, details on the implementation of the model, observed specimens and experimental setup.

3.1 Dopant profiling in Si nano-devices

Dopant profiling in modern semiconductor devices is a key issue. The problem arises from the development of transistors based on new substrates (such as silicon on insulator) or based on new 3D architectures (3D transistors on substrate, nano-wires ...). The problem of this devices is that their characteristic size is of the order of some nanometers.

Using the developed model, STEM/EDX can actually be used for this kind of measurements. For that, dopant mapping has been carried out applying STEM/EDX to the source drain regions of a FinFET device.

A FinFET device [45] is specific type of 3D transistor that can be obtained by using standard lithography techniques on Silicon On Insulator (SOI) substrates. SOI consists in a wafer composed by a thin crystalline Si layer of uniform thickness on top of an oxide layer. The top layer can be used to create horizontal nano-rods, called fins, using standard lithography techniques (see figure 3.1(a)). A MOSFET transistor, called a FinFET, can then be build using the obtained fins. Several types of FinFETs exist, depending on the specific design of the several oxide and metal layers composing the transistor. However, the general idea behind all possible geometries is to obtain an enhanced control of the transistor by improving the gate geometry. For this, small fins are normally used (some tens of nanometers), and the gate has a 3D structure composed by several walls. A schematic drawing of a FinFET with a three walls gate is shown in figure 3.1(b).

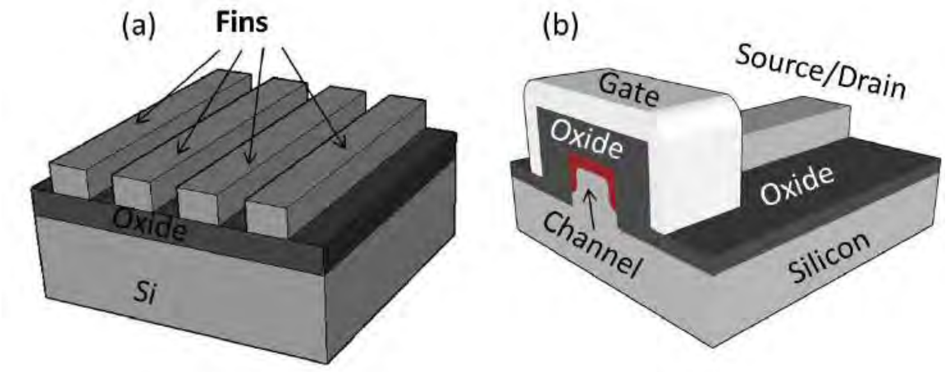

Figure 3.1: Schematic illustrations of a SOI substrate with fins (a) and a FinFet (b).

One of the main problems when creating a FinFET is that doping must be symmetrically distributed on all the walls used to control the structure. This means that (again with reference to figure 3.1(b)) the lateral walls in a three walls structure must have the same doping concentration than the upper wall. A doping distribution fulfilling this requirement is referred to as a “conformal” distribution.

It is easy to understand that for a transistor to work correctly the source and drain doping must also have a conformal distribution. And since the gate can be lowly doped (and even unopened) in FinFET devices while the source drain region must be highly doped to assure an ohmic contact, the problem of the conformal doping of the source and drain region is the most critical problems for FinFET devices. For this reason we have decided to apply the developed model to the measurement of a high concentration As conformal doping in FinFET test structure.

In the following the experimental details on the observed specimen and the observation conditions will be described. In section 3.1.4, the calibration of the model will be discussed and it will be shown that a quantitative As profile can be obtained on the nanometer scale. Finally the measurement errors and doping detection limit will be estimated, and the possibility to improve the detection limit by changing the observation parameters will be discussed.

3.1.1 Description of the samples

Dopant distribution A FinFet test structure with a channel width of 80 nm a height of 100 nm having received a high dose implant (see Figure 3.2(b)). The test structure did not present any gate oxide or metallic contacts since we wanted the observation to be focused on dopant distribution. For the creation of the doped region an arsenic plasma implant has been used to dope the specimen in order to obtain a conformal distribution of the doping profile.

To be able to measure arsenic doping concentration in silicon nanodevices, we have designed some calibration specimen obtained by ionic implantation of arsenic in monocrystalline silicon wafers. In order to check the precision of the calibration on different concentrations, two specimens have been used. Both were implanted using an acceleration voltage of 21 keV but with a different dose amounting, respectively, to 9.4x 10^{15}cm^{-2} and 1.8x10^{15}cm^{-2}. It has to be noted that due to the high dose, the implanted wafers are amorphized in the implantation region (see figure 3.3). The implantation parameters have been chosen by simulating the implantation profile using the SRIM (Stopping and Range of Ions in Matter) Monte Carlo simulation software ([46] ch.3). The simulation results corresponding to the two different doses are shown in 3.2(a). It can be noted that the value of the concentration peak amounts to 10^{21} cm^{-3} (equivalent to 10% atomic As concentration) for the higher dose implant and to 5x10^{21} cm^{-3} (2% atomic As concentration) for the lower dose implant.

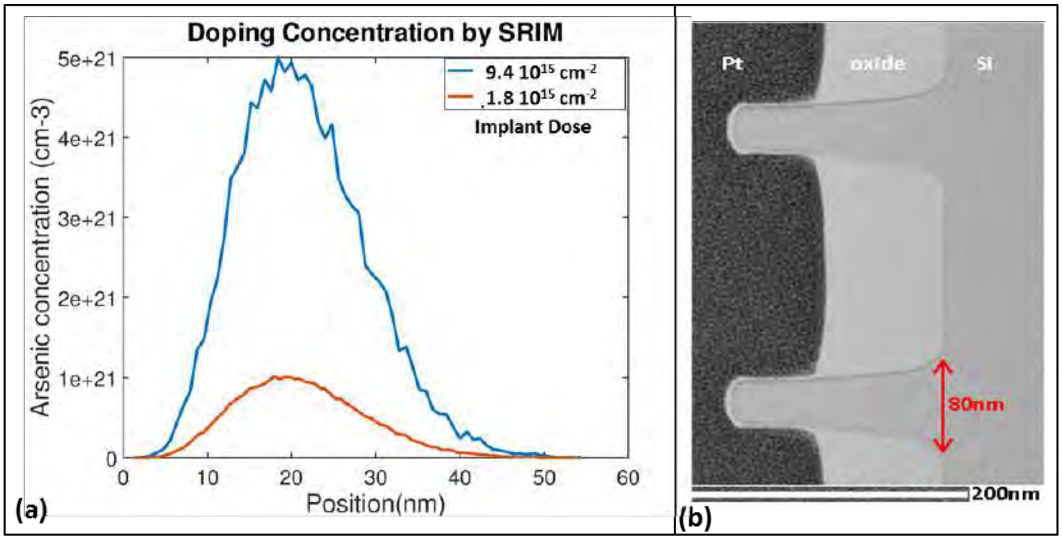

Figure 3.2: (a) Implanted doping distribution simulated with SRIM for As implant in silicon with an energy of 21keV; (b)TEM image of the cross section of the FinFET sample.

In order to have an absolute measurement of the arsenic concentration Rutherford backscattering spectroscopy (RBS) measurements have been carried out on the implanted specimens using He^+ ions accelerated at 1.5 MeV. The detector resolution and solid angle have been obtained on a SiO_2 reference specimen using a detector collection angle of 10°. For the As concentration measurements a collection angle of 60° has been used. Using RBS the atomic concentration profiles (atoms/cm^3) of arsenic in the two calibration specimens have been obtained. The spatial resolution of the RBS technique is about 4 nm while the final error on the concentration measurement is in the order of 10%. These results were used to calibrate the C-L coefficients, using the method described in section 2.4.

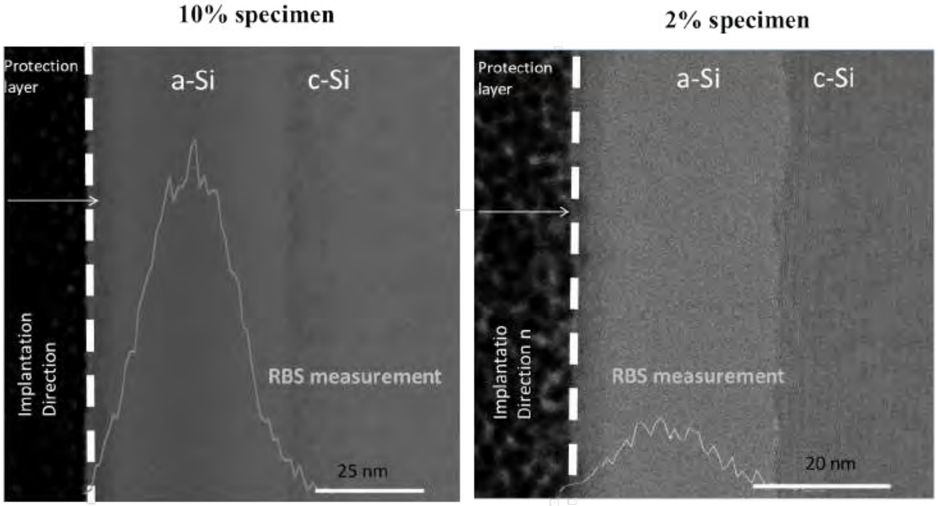

Figure 3.3: RBS measurement of As atomic density superimposed to the TEM image obtained in the same specimen. The contrast variation in the TEM images indicate that the high concentration implanted region is amorphized.

3.1.2 Specimen preparation and TEM observations

For TEM observation, a cross sectional lamella has been created using a FEI Helios 600i dual beam focused ion beam (FIB) [47]. A lift-out procedure has been used to transfer the specimen on a supporting copper grid. In order to minimize curtaining effects a layer of platinum has been deposed on the wafer surface before the creation of the lamella. Platinum deposition has been carried out in two consecutive steps by using Electron Beam-Induced Deposition (EBID) followed by Ion Beam-Induced Deposition (IBID) in order to avoid any kind of ionic damage near the surface, that can be potentially created during IBID. It has to be noted that there is an additional advantage in using FIB specimen preparations for EDX analysis. The use of a lamella reduces the emission of secondary X-rays by fluorescence and the backscattering in comparison with specimens prepared by other techniques like mechanical grinding followed by ion thinning (see figure 3.4). FIB preparation has also been used in the case of the FinFets since a precise specimen region has to be selected in order to observe the implanted regions (such as the region shown in figure 3.2).

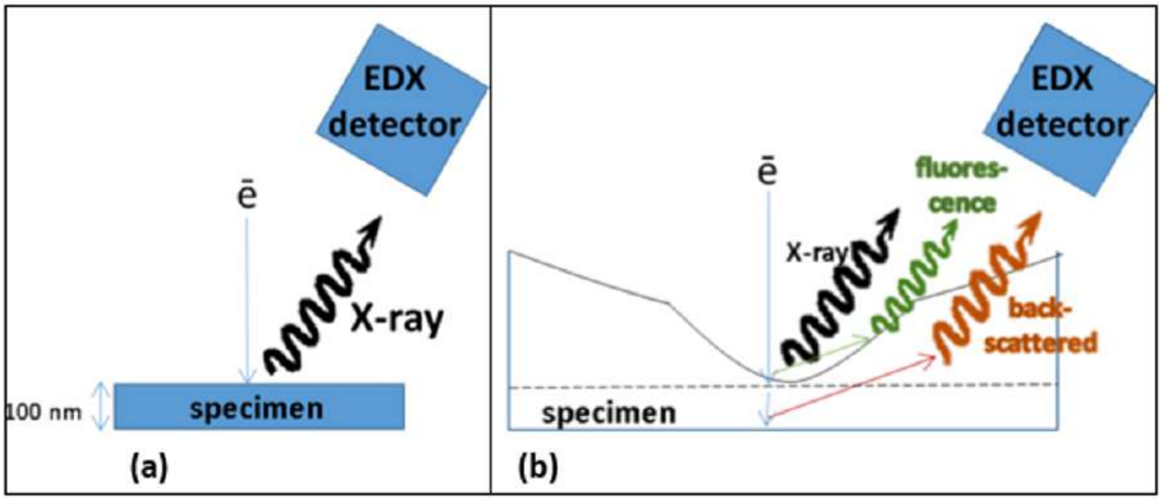

Figure 3.4: Schematic illustration of the influence of the specimen geometry on EDX artifacts (secondary X-rays created by fluorescence and backscattered electrons) in specimens prepared using: a) FIB. b) mechanical thinning.

The STEM/EDX measurements have been carried out on a JEOL ARM cold FEG microscope equipped with a probe spherical aberration corrector at 200kV with a STEM resolution about 0.78 Å. For the EDX measurements, a CENTURIO-X detector with an elevation angle of 24.3 degrees and a collection angle of 0.98 steradians has been used. The EDX detector has an energy resolution of 129 eV.

The distribution profiles have been obtained by acquiring STEM/EDX maps and subsequently creating cumulative spectra at several depths by integrating the signal in the lateral direction. The JEOL analysis Station program has then been used order to subtract the Bremsstrahlung background noise in the cumulative spectra and to calculate the integrated intensities of the characteristic peaks for the various elements. The obtained intensities have been used as a starting point for the calibration, the absorption correction and the error estimation.

3.1.3 Application of the quantification Method

The quantification of the data have been carried out using the methods in the previous chapter. To be able to apply the the self-consistent calibration method the formula to be used to calculate the mass density has been established both for amorphous SiAs alloy (a-SiAs) found in the calibration specimens and for the As-implanted crystalline silicon (c-SiAs) composing the FinFETs.

For a-SiAs, the "constant radius" and "amorphous solid" approximations can be considered. The value of the covalent radius for silicon and arsenic have a close value, $R_{Si} = (111 \pm 2)pm$ and $R_{As} = (119 \pm 4)pm$, while the value of their atomic masses greatly differ $m_{Si} = 28.0855\frac{g}{mol}$ and $m_{As} = 74.9216\frac{g}{mol}$. Hence the "constant radius approximation" could in principle be a good approximation and 2.16 could be used for density calculation.

But in practice this approximation overestimates the mass density of amorphous SiAs (a-SiAs) for high arsenic concentrations comparing to the value of the amorphous arsenic found in the litterature ($\rho^M_{a-As} = 4.7\frac{g}{cm^3}$ [48]) as shown in figure 3.5.

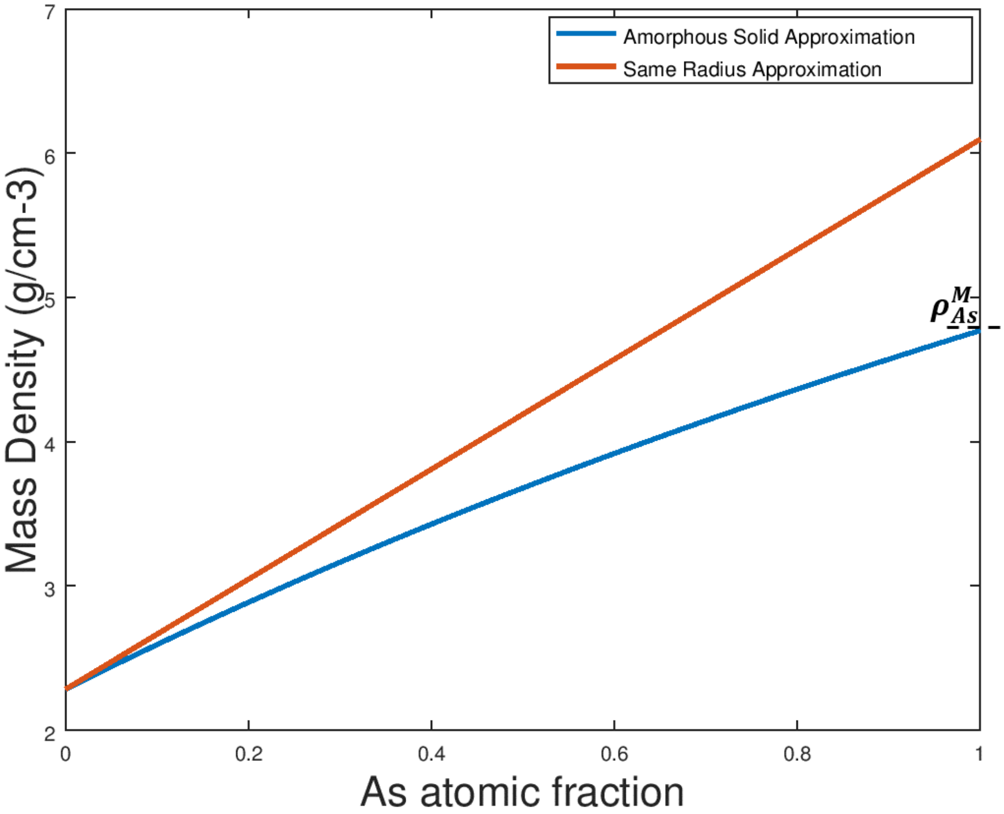

Figure 3.5: Mass density a function of the As mass fraction calculated with two different approximations. The experimentally determined value of the mass density ρ^M_{As} of amorphous arsenic [48] is shown in the plot.

It could then be tempting to use the "amorphous solid approximation" (equation 2.19) in this case. But, as already discussed in section 2.3.2, to justify this choice one of this two assumptions must be satisfied:

- The structure of a-SiAs is compatible with that of an IAS structure.
- The structure of the alloy is similar to that of the amorphous forms of the pure

elements. In this case the same reasoning applied in section 2.3.3 to the pseudomorphic alloys can be applied in the case of a-SiAs.

It is easy to prove that neither a-As nor a-Si are ideal amorphous solids. For a-Si this can be proved by noting that the density predicted by the IAS model $\rho^M_{a-Si,IAS} = 4.32 g/cm^3$[38] is higher than the density of crystalline Si (c-Si) $\rho^M_{c-Si} = 2.32\, g/cm^3$for the diamond structure. This is in clear contradiction with the experimentally determined density of amorphous silicon $\rho^M_{a-Si} = 2.285\, g/cm^3$[49] which is slightly lower than ρ^M_{c-Si}. The same kind of reasoning can be used to prove that the structure of amorphous As ($\rho^M_{a-As} = 4.7\, g/cm^3$,$\rho^M_{c-As} = 5.73\, g/cm^3$) is also not compatible with that of an IAS. In conclusion there is no reason to think that the a-SiAs alloy (whose structure is a combination of the structure of amorphous Si and amorphous As) has an IAS structure.

On the other hand it is easy to show that a-Si and a-As have a similar structure. It can then be assumed that this same atomic arrangement is preserved in the SiAs alloy for any value of As concentration which is precisely the assumption used to derive equation 2.19. To show this the fraction $s = \frac{V^S}{V^A}$ between the atomic volume V^A and the atom size V^S must be evaluated. This parameter is an estimator of the packing ratio of the solid. The volume V^A is by definition the inverse of the atomic density $\rho^A = \rho^M/m$ of the material while the atom size calculated by using using a spherical approximation ($V^S = \frac{4}{3}\pi r^3$) and the covalent radius r. The values of $s = \frac{4}{3}\pi r^3 \rho^A$ for amorphous Si and amorphous As can be calculated by using the previously defined data for the density, the radius and the mass of the two elements. The obtained values are quite close ($s_{Si} = 0.28$,$s_{As} = 0.26$) confirming that the packing of the two structure is almost the same.

The comparison between the “amorphous solid approximation” and the “same radius approximation” is shown in figure 3.5. It can be noted that the “amorphous solid approximation” gives better results than the “same radius approximation” for high arsenic concentrations while the two approximations are almost equivalent for low As concentrations as we can see in figure 3.5.

For c-SiAs, it is much simpler to obtain the mass density formula since this correspond exactly to the case the “constant radius approximation” has been derived for. Mass density can then be calculated using 2.16 with $m_1 = m_{Si}, m_2 = m_{As}, \rho^M_1 = \rho^M_{Si}$.

3.1.4 Experimental results and discussion

In this section we will present the experimental results obtained on the FinFET test structure. For that, the calibration results, that have been used to obtained the calibration value of the C-L coefficients will be described first. Then the final results obtained on dopant profiling will be discussed.

Calibration results

In order to apply the calibration techniques the atomic density concentrations $c^A_{A/RBS}(x)$ measured by RBS have been converted into mass fractions. Then the C-L coefficients have been obtained by weighted linear regression as described in section 2.4. Equations 2.4 and 2.21 can be combined to obtain the mass fractions measured by RBS:

$$\left[f^M_{As}(x)\right]_{Meas} = \frac{m_{As}c^A_{As/RBS}(x)}{N_{AV}\rho^M_{a-Si} + m_{As}c^A_{As/RBS}(x)\left(1 - \frac{\rho^M_{a-Si}}{\rho^M_{a-As}}\right)}$$

The calibration technique described in section 2.4 have been applied to the a-SiAs calibration specimens described in section 3.1.1. An EDX hyper-map consisting of a series of spectra (one for each pixel of the corresponding STEM image) has been recorded (see figure 3.6 for the 2% specimen and figure 3.7 for the 10% specimen). For the acquisition the FIB specimen has been oriented as in figure 2.2. Then a line profile has been obtained by integrating the obtained map (see figure 3.6(a) and 3.7 (a)) in a direction perpendicular to the depth direction (defined in figure 2.2). Several characteristic peak families have been used associated: the K peaks for silicon, and either the K or the L peaks for arsenic (see figure 3.8).

The absorption correction procedure described in section 2.2 has then been used to calculate the absorption corrected intensities $\widetilde{I}_{Si:K}$, $\widetilde{I}_{As:K}$ and $\widetilde{I}_{As:L}$. The iterative absorption algorithm has shown a rapid convergence and no numerical instability (see figure 3.9(a)). Convergence is basically obtained after two iterations (only few curves are visible since the profiles for the iterations from 2 to 10 are superimposed). Moreover it can be observed that the absorption effects are more pronounced in the high density region (see figure 3.9(b)). This can be understood by noting that the mass density of the specimen is higher in this region and, as a consequence, the absorption effects are bigger. This is a clear demonstration of the fact that it is important to establish a density formula in order to take into account the mass density dependence on the local concentration.

Then fore-mentioned linear regression techniques have then been used on the absorption corrected data to calibrate:

- the CL factor $K_{As,Si:K,K} = k_{As:K,K}$ associated to the K family of peaks of arsenic when the K family of peaks of silicon is used as reference
- the CL factor $K_{As,Si:L,K} = k_{As:L,K}$ associated to the L family of peaks of arsenic when the K family of peaks of silicon is used as reference

In order to minimize the error on the C-L coefficients we have carried out the calibration on the higher dose specimen. The reason of this choice can be easily understood by observing that under the fore-mentioned hypothesis that the X-ray count has a Poisson

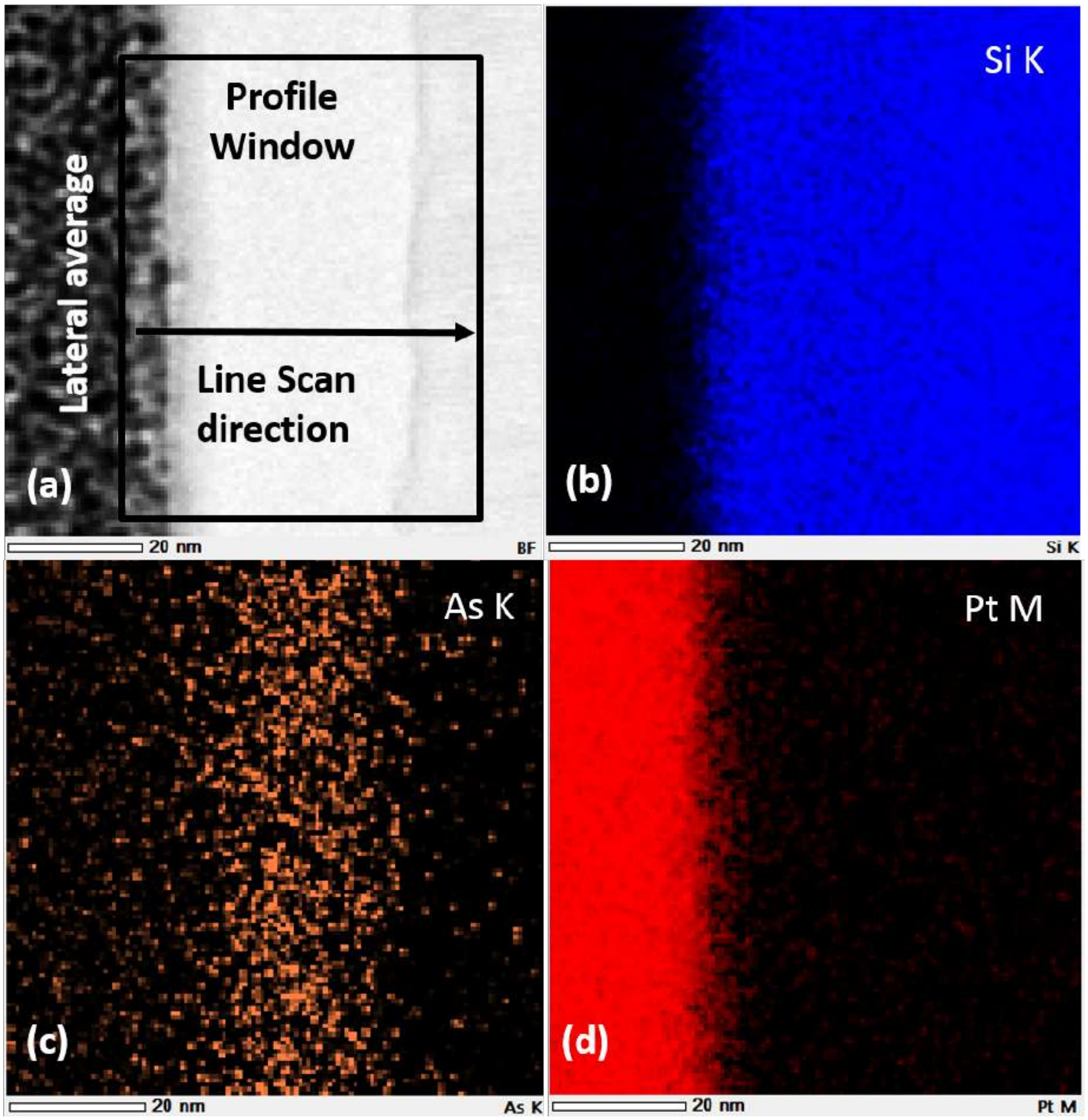

Figure 3.6: Intensity maps obtained on the calibration specimen with a **2% atomic density peak**. In inset (a) the BF-STEM image of the mapped region is shown together with the geometry of the linescan used for the extraction of a profile. The intensity maps after peak integration and bremsstrahlung subtractions are show in the other insets for the following peak families: SiK(b), AsL(c), Pt(M) (d).

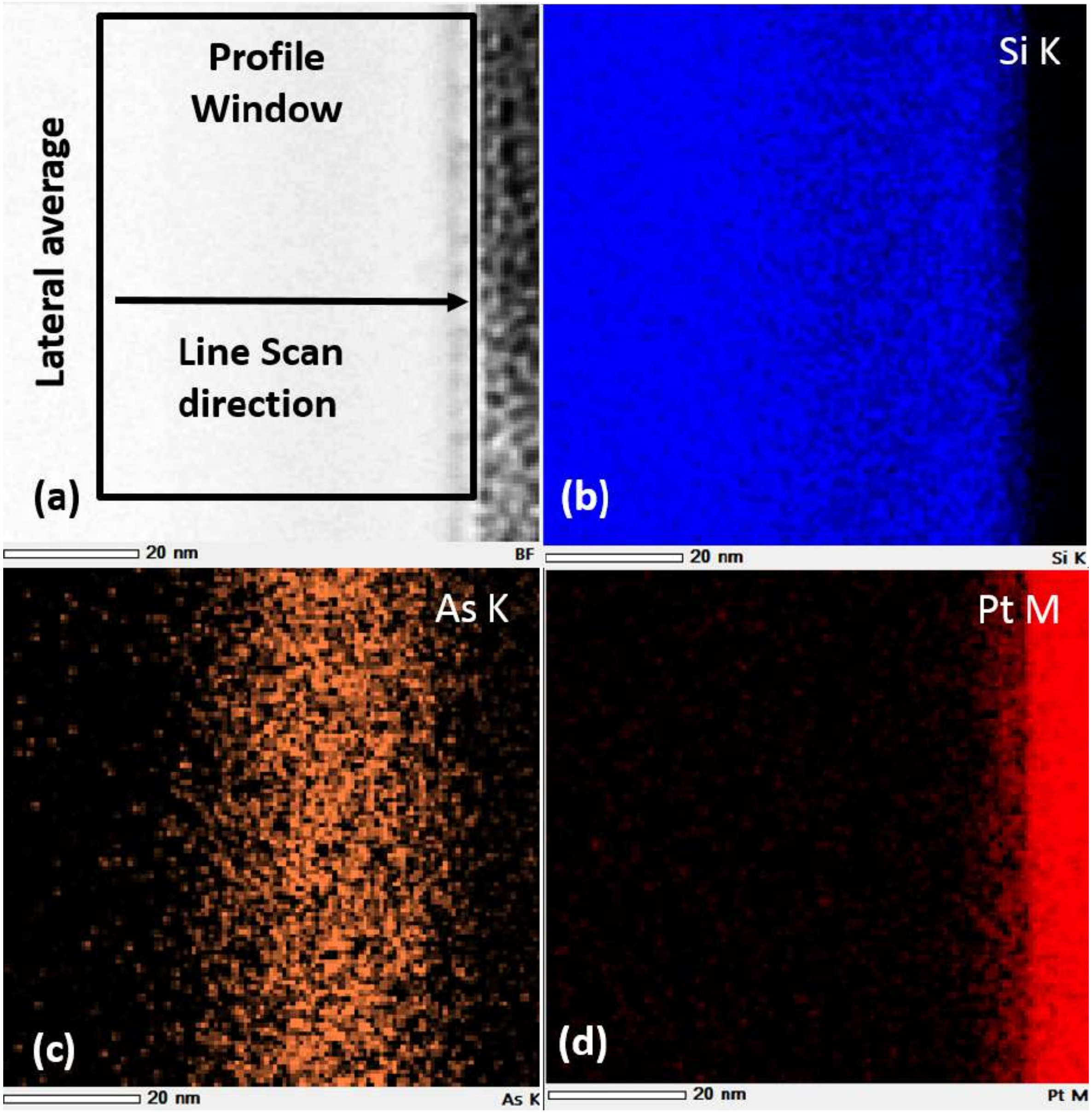

Figure 3.7: Intensity maps obtained on the calibration specimen with a **10% atomic density peak**. In inset (a) the BF-STEM image of the mapped region is shown together with the geometry of the line scan used for the extraction of a profile. The intensity maps after peak integration and bremsstrahlung subtractions are show in the other insets for the following peak families: SiK(b), AsL(c), Pt(M) (d).

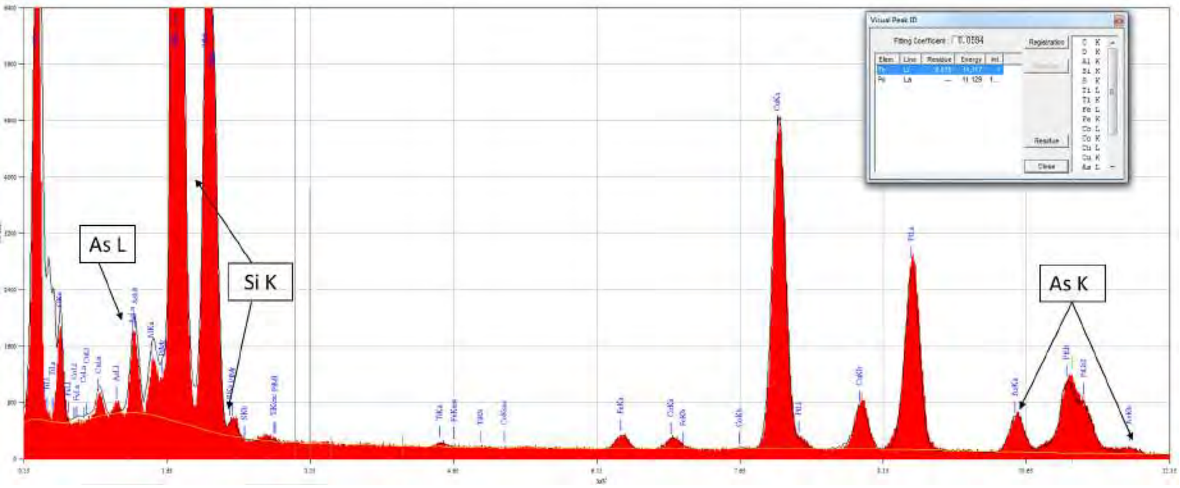

Figure 3.8: EDX spectrum obtained from the 10% specimen and showing the position of the Si and As peak families.

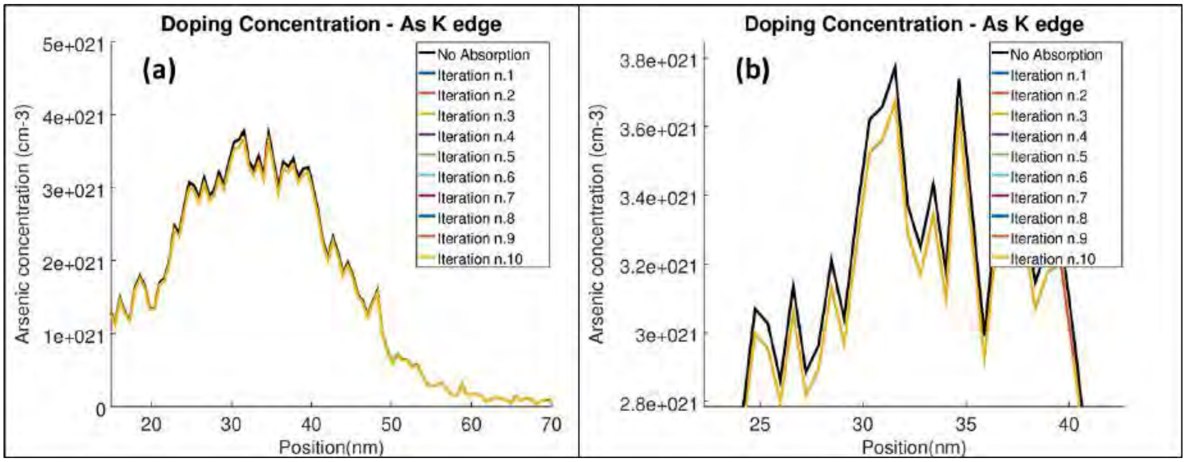

Figure 3.9: The result of the correction absorption for the first 10 iterations. In (a) the full profile is shown while in (b) a zoom on the high density region is displayed.

distribution the relative error is minimized for higher peak intensities. This implies a lower variance on the intensity values and a lower error on the best-fit values of the C-L coefficients

The doping concentration measured by EDX and RBS are reported in figure 3.10 before and after the calibration of the C-L coefficients. This has allowed us to obtain the following best fit coefficients for the microscope used in this experiment: $K_{As,Si:K,K} = 2.18 \pm 0.03$, $K_{As,Si:L,K} = 1.89 \pm 0.03$.

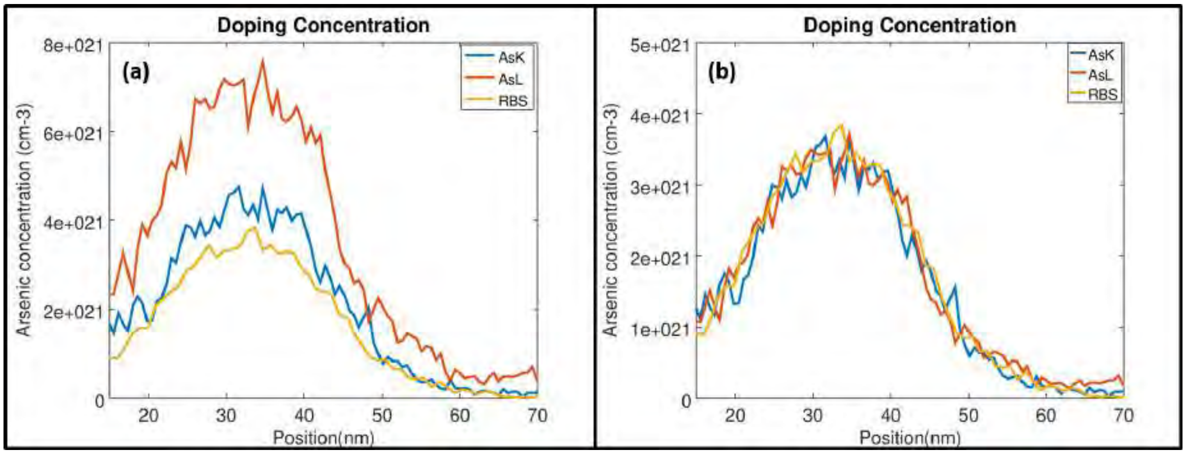

Figure 3.10: Plot of the measures As concentration $\widetilde{c}^{A}_{As}(x)$ before (a) and after (b) calibration of the CL coefficients. The values obtained by using the $I_{As:K}$(AsK) and $\widetilde{I}_{As:L}$ peaks are reported and compared with the values obtained by RBS.

The error on the C-L coefficients can be used to estimate the final errors on the density profile as explained in section 2.4 where the possible sources of error have been discussed. Between the different errors the error arising from the uncertainty on the specimen thickness deserves a special discussion. It is generally complicated to measure specimen thickness in a reliable and precise way. Even if some techniques exist, measurement by SEM, EELS, convergent beam electron diffraction, it is complicated, in general to obtain a value with a low error. As a consequence measurement errors on the thickness can be in the order of 30% or higher. It is then important to assess the influence of the thickness error on the density measurement. For this, the measurement variation on the peak region of the two specimens (that, as already noted are the most affected by absorption) is reported in figure 3.11. It can be easily observed that the variation of the concentration is small even for large thickness variations. This means that a precise measurement of the doping concentration can be obtained even if the error on the specimen thickness (Δt) is high. The obtained profiles as well as the total experimental errors on the EDX As concentration measurement in the 10% specimen are shown in figure 3.12.

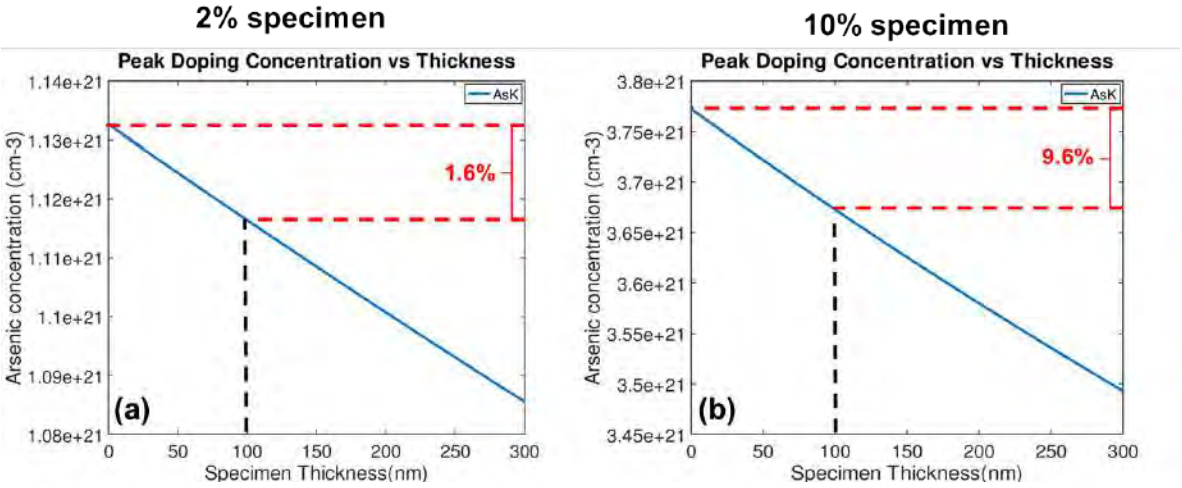

Figure 3.11: Variation of the absorption corrected peak density in the 2% (a) and 10% (b) specimen. The concentration has been obtained by using the AsK and SiK families.

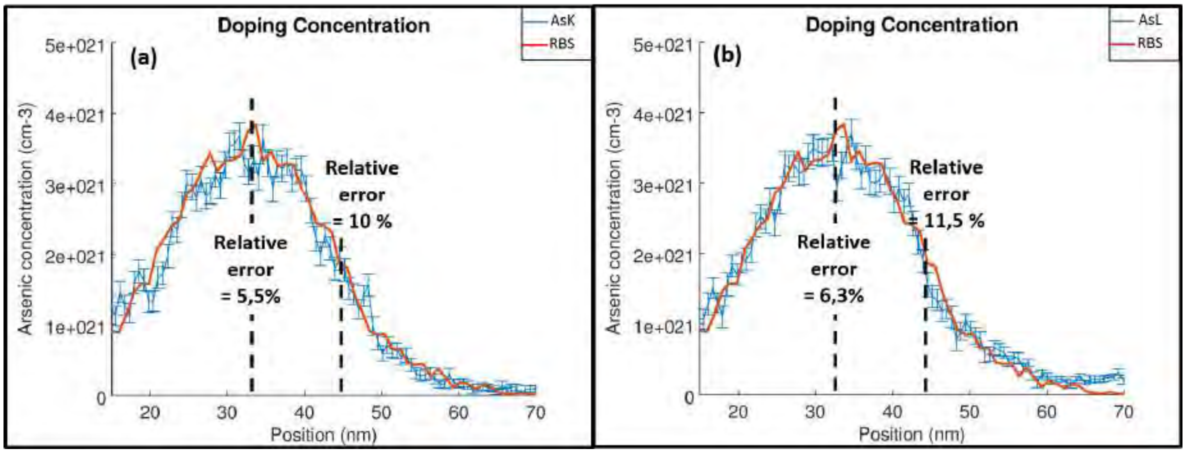

Figure 3.12: Plot of the measures As concentration $\widetilde{c}^{A}_{As}(x)$ of the 10% specimen using (a) K peaks for Si and As and (b) K peak for Si and L peaks for As. In both cases the obtained values are compared with the values obtained by RBS.

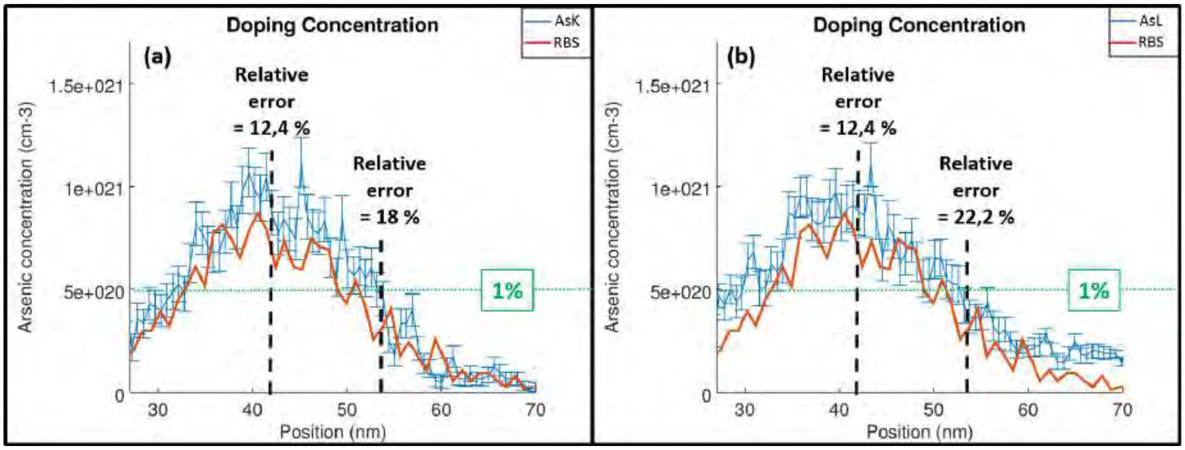

Figure 3.13: Plot of the measures As concentration $\widetilde{c}^{A}_{As}(x)$ of the 10% specimen using (a) K peaks for Si and As and (b) K peak for Si and L peaks for As. In both cases the obtained values are compared with the values obtained by RBS.

In order to check the validity of our procedure and the applicability of these coefficients to arsenic distribution with lower concentrations, we have used the previously obtained values of the CL coefficients to measure the doping concentration in the 2% a-SiAs specimen. The results are shown in figure 3.13 where the experimental errors on the EDX measurements are also reported.

First of all it must be observed that the experimental error is larger for higher concentrations. This is due to hypothesis that X-ray intensities follow a Poisson distribution. This implies that the absolute error on the measured intensity increases with the intensity while the relative error decreases. The error on doping concentration follow the same trend since it directly depends on the error on the measured intensity. This means that, in the doping distribution peak, the measured value of doping concentration is more precise (i.e. has a lower relative error) than the values in the distribution tail, even if larger error bars appear in the graph.

Figure 3.13 clearly shows that the results obtained using the K peaks of arsenic are more accurate than those obtained using the L peaks. This is still more evident for low concentrations (i.e. in the rightmost tail of the doping profile).

The origin of this discrepancy can be sought, in our opinion, in the lack of precision on the measured intensity of the L peaks of arsenic. This is due to the position of the L peaks, located in the low energy region of the spectrum. In this region the subtraction of the bremsstrahlung noise is more difficult since the noise is higher and there are neighboring peaks associated to oxygen and carbon. For low As concentrations, such as those we are measuring, this problem becomes critical since the bremsstrahlung and peak intensities can be of the same order of magnitude. This means that a small error on the background noise interpolation has a strong impact on the measurement of As concentration. We have thus decided to use the arsenic K peaks for all the measurements reported in the following.

Dopant profile measurement

To check the applicability of our method to a real nanodevices we have carried out some measurements on the FinFET device already described in section 3.1.1. For that an EDX hyper-map has been acquired. Some intensity maps and profiles extracted from the hyper-map are shown in figure 3.14.

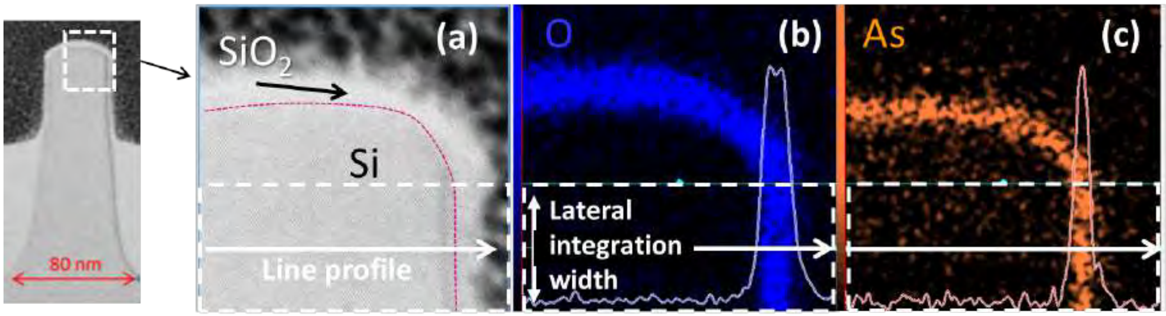

Figure 3.14: Bright field STEM images(a) and EDX intensity maps (b-c) obtained on a FinFET device. The K peaks have been used both for oxygen and arsenic to obtain the elemental maps shown in (b) and (c) from the EDX hyper-map. Intensities profiles obtained using a laterally averaged line-scan are superimposed to maps ((b) and (c)). The direction and position for the line-scan as well as the lateral integration width are shown in figure (a), (b) and (c).

In order to be able to apply the same measurement geometry illustrated in chapter 2 and in figure 2.2 we have decided to study the distribution of one of the FinFET vertical wall and the specimen have been oriented for the acquisition as in figure 3.15(a). The newly developed quantification method described in the previous section has then been applied to the silicon and arsenic K peaks profiles. The final result is shown in figure 3.15(b) where the doping profile on the lateral wall and the corresponding errors are shown.

The results clearly show that a doping profile in a nanodevice can be obtained with this technique and that the obtained experimental error is low enough to be able to appreciate the concentration variations in the profile.

3.1.5 Detection limit

It is interesting, in the context of doping profile by STEM/EDX to try to understand what is the detection limit for arsenic concentration. To estimate the detection limit we have used a simple approach based on the experimental results. It is easy to understand that a density measurement c cannot be distinguished by zero if zero is included in the confidence interval (i.e. it is between $c-\Delta c$ and $c+\Delta c$). The obtained result obviously

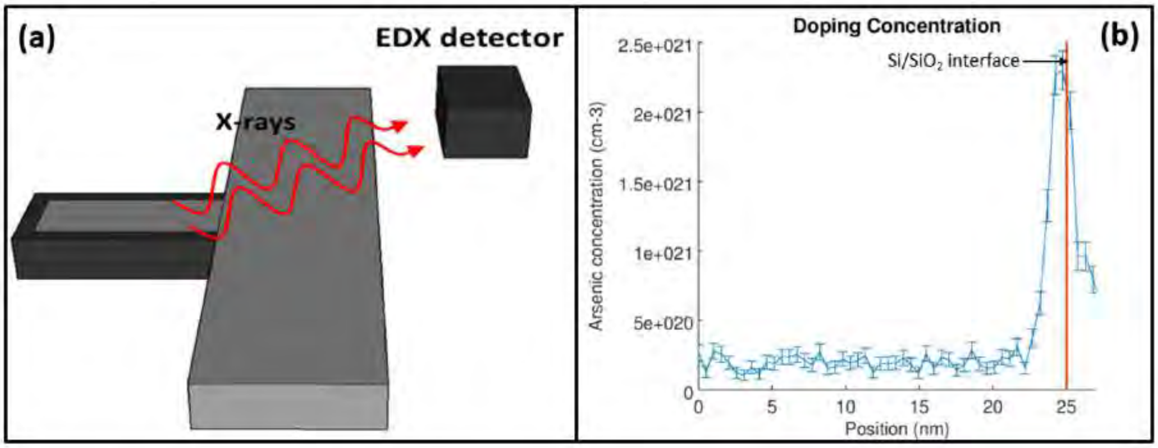

Figure 3.15: (a) Schematic image illustrating the geometry used to obtain the doping profile and (b) doping profile with experimental error obtained by applying the quantification method described in chapter 2.

depends on the chosen confidence level[42] (a Student coefficient equal to 1 has been chosen in this paper).

The analysis of the profiles (see figure 3.15) clearly show that doping concentration is always above the concentration limit. The concentration limit can be obtained from the calibration data shown in 3.13(b) and can be estimated to be $7.7 \cdot 10^{19} cm^{-3}$.

This is not an absolute estimation since the value of the detection limits clearly depends on the measured doping peaks intensity (see equation 2.29 and 2.30) and can be improved by increasing the hyper-map exposition time. The previously discussed formulas can be used to calculate the error associated to a specific set of measured intensities but it is impossible to deduce a theoretical lowest limit since the maximum exposition time depends on many experimental factors such as the stability of the specimen to drift and its resistance to electron irradiation.

Yet a target intensity value can be estimated. To give an example of this procedure, we have estimated the exposition times needed to obtain a given detection limit using the specific parameters of our experimental setup. More specifically we have used the values of the count per seconds of our setup to calculate the measuring time needed to obtain different values of the detection limit. For the calculations we have supposed that the counts-per-seconds are not changing with time.

Using equation 2.2, 2.31 and 2.34 and making the approximations that the error on the thickness is negligible and that the As peak has a negligible intensity when compared to the Si peak we we can obtain the following formula:

$$I_{Si:F_{Si}} = \frac{\frac{k_{As:F_{As},F_{Si}} * \widetilde{f}^M_{As}\left(1-\widetilde{f}^M_{As}\right)}{\widetilde{f}^M_{As}(x)} + 1}{\left(\frac{\frac{\Delta\widetilde{c}^A_{As} m_{As}}{N_{AV}\left\{\widetilde{\rho}^M_{a-SiAs} + \widetilde{f}^M_{As}(x)\frac{\widetilde{\rho}^M_{a-Si}\eta}{\left[1-\eta\widetilde{f}^M_{As}\right]^2}\right\}}}{\widetilde{f}^M_{As}\left(1-\widetilde{f}^M_{As}\right)}\right)^2 - \left(\frac{\Delta\widetilde{f}^M_{As}}{k_{As:F_{As},F_{Si}}}\right)^2} \tag{3.1}$$

This formula express the intensity $I_{Si:F_{Si}}(x)$ of the Si peak needed to obtain the following value for the As density: $\widetilde{f}^M_{As} \pm \Delta\widetilde{f}^M_{As}$. According to our definition of the detection limit, the intensity I_D needed to obtain a detection limit D can be obtained by putting $\Delta\widetilde{f}^M_{As} = \widetilde{f}^M_{As} = D$ and in equation 3.1

The exposition time needed to obtain a measured intensity I_D can be estimated by using the counts per second (cps) as the following (it is obviously assumed that $I_{Si:F_{Si}} = 0$ for $t_{exp} = 0$) :

$$t_{exp} = \frac{I_{Si:F_{Si}}(x)}{cps} \tag{3.2}$$

The measuring time needed to improve the detection limit can then be calculated, and some results are shown in table 3.1. It can clearly be observed that in our case it is difficult to considerably improve the detection limit just by increasing the measuring times, since the presence of specimen drift, beam damage and current instability (in our case a cold Field Emission Gun gun is used) limit the measuring time to a few tens of minutes.

As density detection limit	**Measuring time (live time)**
$1\,10^{19} cm^{-3}$	51 minutes
$5\,10^{18} cm^{-3}$	1 hour and 43 minutes
$1\,10^{18} cm^{-3}$	8 hours and 55 minutes

Table 3.1: Estimated measuring time (live time) needed to obtain higher detection limits

3.2 Composition profiling of SiGe nanostructures

SiGe layers are of high interest in modern microelectronics due to their improved hole mobility compared to silicon (p-type Metal Oxide Semiconductor transistors channel engineering) and their compatibility with current devices. In modern devices very low resistivity boron- doped SiGe sources and drains are used to compressively stress the channel of short gate length devices, resulting in better electrical performances[50].

To obtain highly-doped and ultra-shallow source and drain regions in SiGe devices some specific annealing processes are needed, such as (RTP).

In particular, Ultra Violet Nanosecond Laser Annealing (UV-NLA) receives much attention because of several promising results obtained on pure silicon and pure germanium [51]. However, there are few studies dealing with the behavior of silicon/germanium layers upon UV-NLA.

On these samples SIMS studies can be performed in order to measure the Ge concentration, but the lack of reliability in nanoscale devices brings us to apply the STEM/EDX technique we have developed. The results obtained in SiGe devices will be discussed in this section.

As in the section 3.1, the experimental details on the observed specimen and the observation conditions will be described, the calibration of the model will be examined and the measurement errors will be calculated.

3.2.1 Description of the samples

As in the case of the SiAs specimen, in order to have an accurate measurement of the Ge concentration two calibration samples with two different thicknesses (28nm and 48 nm) of the SiGe layer have been used as we can see in the figure 3.16. The growth of the SiGe layer was performed in a 300 mm reduced Pressure Chemical Vapor Deposition (PCVD) chamber after surface preparation.

To obtain a calibrated value of the C-L coefficients, Rutherford backscattering spectroscopy (RBS) measurements have been carried out using He^+ ions accelerated at 1.5 MeV. The detector resolution and solid angle have been obtained on a SiO_2 reference specimen using a detector collection angle of 10°. For the Ge concentration measurements a collection angle of 65° has been used. Using RBS the atomic atomic fraction of Ge in the two calibration specimens have been obtained and these results were used to calibrate the C-L coefficients.

To check the applicability of our technique at the nanoscale, a germanium profile has been measured by STEM/EDX on a nanodevice test structure consisting in an undoped pseudo-morphic $Si_{1-x}Ge_x$ layer grown at 550°C on n-type Si (100) substrates. The samples were then subjected to UV-NLA in a SCREEN-LT3100 system, operating at 308 nm wavelength with a 145 ns FWHM pulse. Energy densities were chosen to study regimes from sub-melt to full SiGe layer melting. Melt threshold was detected using in-situ Time-Resolved Reflectivity (TRR) at 635 nm, and surface quality was studied by means of atomic force microscopy and SP2 Haze.

FIB preparation has been performed on all the specimen, in the same conditions described in section 3.1.2.

For the self-absorption correction, the mass density function contained in equation 2.21 and described in section 2.3.3 has been used.

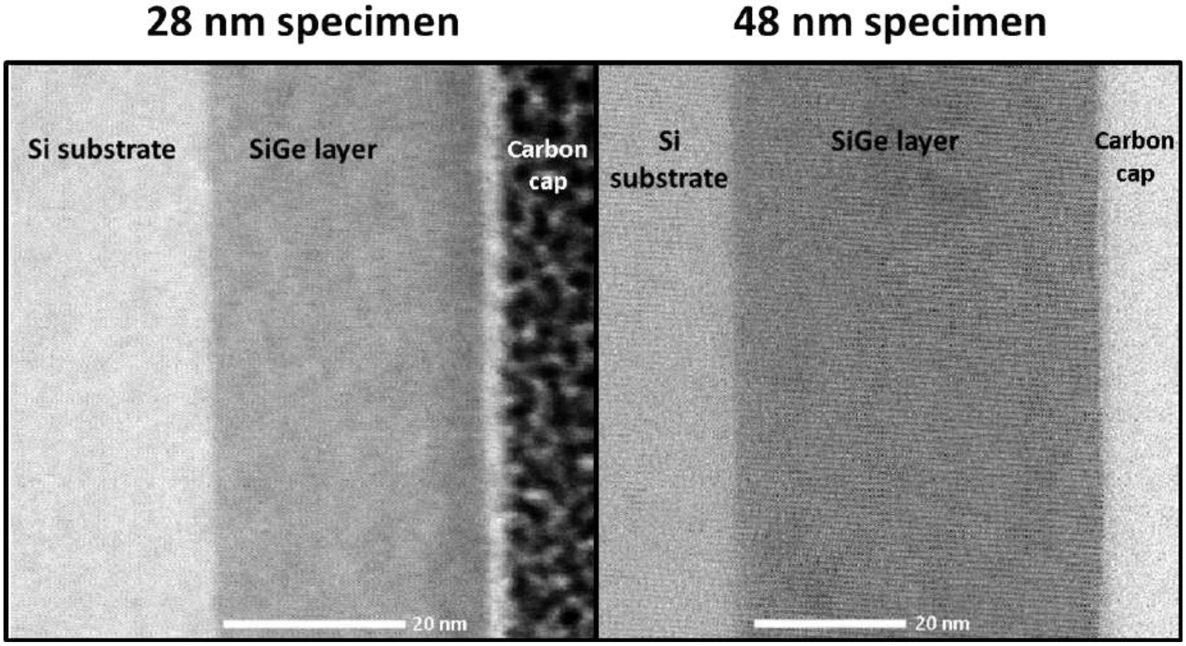

Figure 3.16: Cross-sectional TEM micrographs showing the calibrated specimens structure.

3.2.2 STEM/EDX Results

Calibration results

In order to apply the calibration techniques the atomic fraction $f^{A}_{A/RBS}(x)$ measured by RBS have been used in this case. Then the C-L coefficients have been obtained by weighted linear regression as described in section 2.4 after conversion from the mass fraction to atomic fraction by equation 2.5:

EDX hyper-maps have been also recorded for the 28 nm specimen and the 48 nm specimen (see figure 3.17 and 3.18). For the acquisition the FIB specimen has been oriented as in figure 2.2. Then a line profile has been obtained by lateral integration.

As discussed in section 3.1.4 for the case of Arsenic, the results obtained using the K peaks are more accurate than those obtained using the L peaks since background subtraction is harder to perform on L lines. This is also true for germanium, and in the following discussion we will focus on the results obtained using silicon and germanium K peaks.

To obtain a precise value of the C-L coefficients, the calibration technique described in section 2.4 have been applied to SiGe specimens.

This has allowed us to obtain the calibrated value of the C-L coefficient: $K_{Ge,Si:K,K} = 3.83 \pm 0.02$.

The atomic fraction measured using the Ge K lines before and after calibration are reported, for the two calibration specimens, in figure 3.19 and 3.20.

As in the case of SiAs specimens, the iterative absorption algorithm has shown a rapid convergence and no numerical instability (see figure 3.21). As in the previous case, it can be observed that the absorption effects are more pronounced in the high density region.

Following the same procedure as in the SiAs specimen, the error has been estimated on the two calibration specimen and the results are reported in figure 3.22.

Nanostructure test

To check the applicability of our method to a real nanodevices we have carried out some measurements on the nanodevice test structure described in section 3.2.1. For that, an EDX hyper-map has been acquired. Some intensity maps and profiles extracted from the hyper-map are shown in figure 3.23.

As in the SiAs specimen, the newly developed quantification method has then been applied to the silicon and germanium K peaks profiles. The final result is shown in figure 3.24 where the germanium and silicon profile and the corresponding errors are shown.

The results show, that this technique is relevant for nanodevices and that the obtained experimental error is low enough to be able to appreciate the concentration variations.

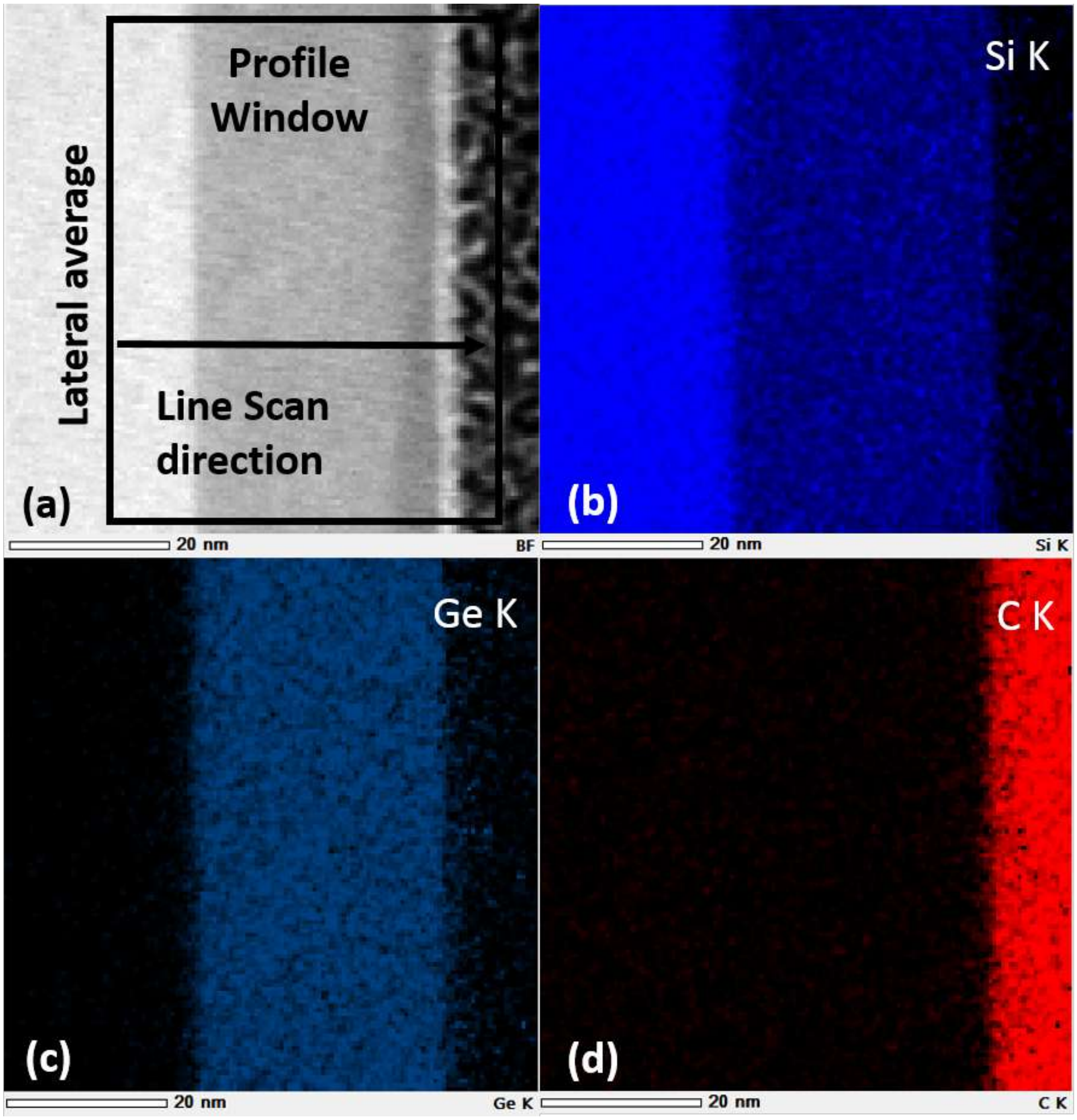

Figure 3.17: Intensity maps obtained on the calibration specimen with a **28 nm of SiGe layer**. In inset (a) the STEM of the mapped region is shown together with the geometry of the line scan used for the extraction of a profile. The intensity maps after peak integration and bremsstrahlung subtractions are show in the other insets for the following peak families: SiK(b), GeK(c), CK (d).

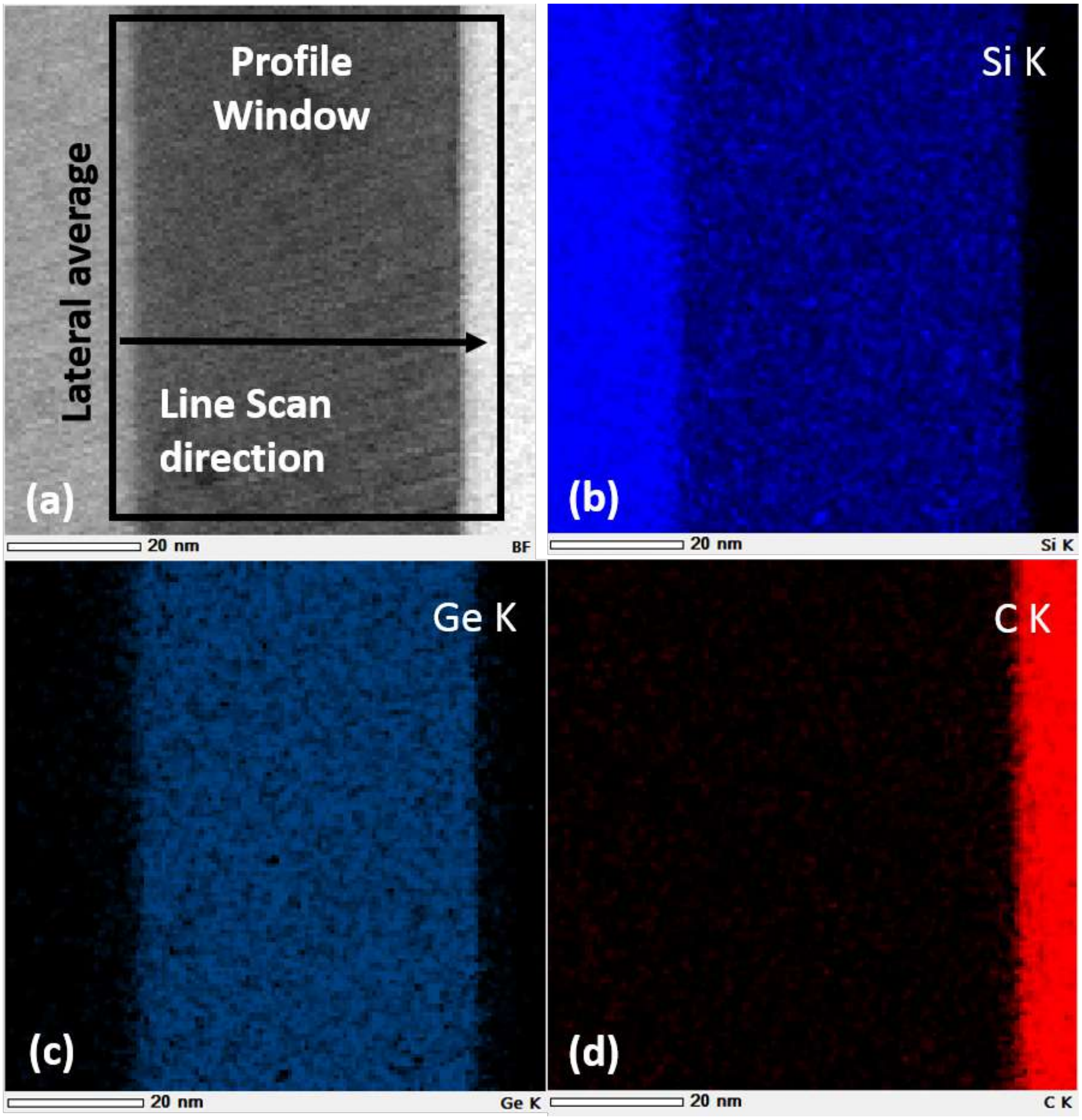

Figure 3.18: Intensity maps obtained on the calibration specimen with a **48 nm of SiGe layer**. In inset (a) the STEM of the mapped region is shown together with the geometry of the line scan used for the extraction of a profile. The intensity maps after peak integration and bremsstrahlung subtractions are show in the other insets for the following peak families: SiK(b), GeK(c), CK (d).

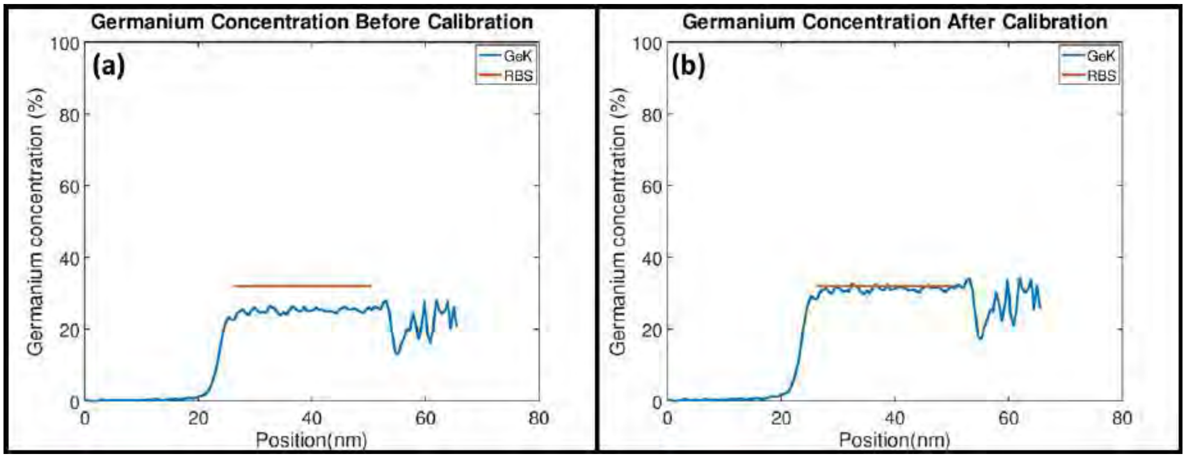

Figure 3.19: Plot of the measures Ge atomic fraction$f^A_{Ge}(x)$ before (a) and after (b) calibration of the CL coefficients for the 28 nm specimen. The values obtained by using the $I_{Ge:K}$(AsK) and $\widetilde{I}_{Ge:L}$ peaks are reported.

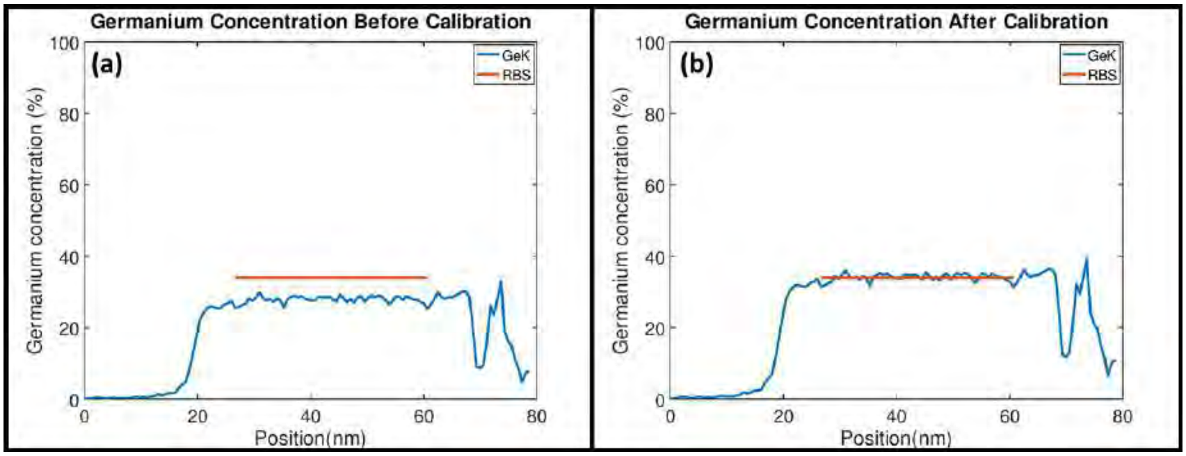

Figure 3.20: Plot of the measures Ge atomic fraction$f^A_{Ge}(x)$ before (a) and after (b) calibration of the CL coefficients for the 48 nm specimen. The values obtained by using the $I_{Ge:K}$(AsK) and $\widetilde{I}_{Ge:L}$ peaks are reported.

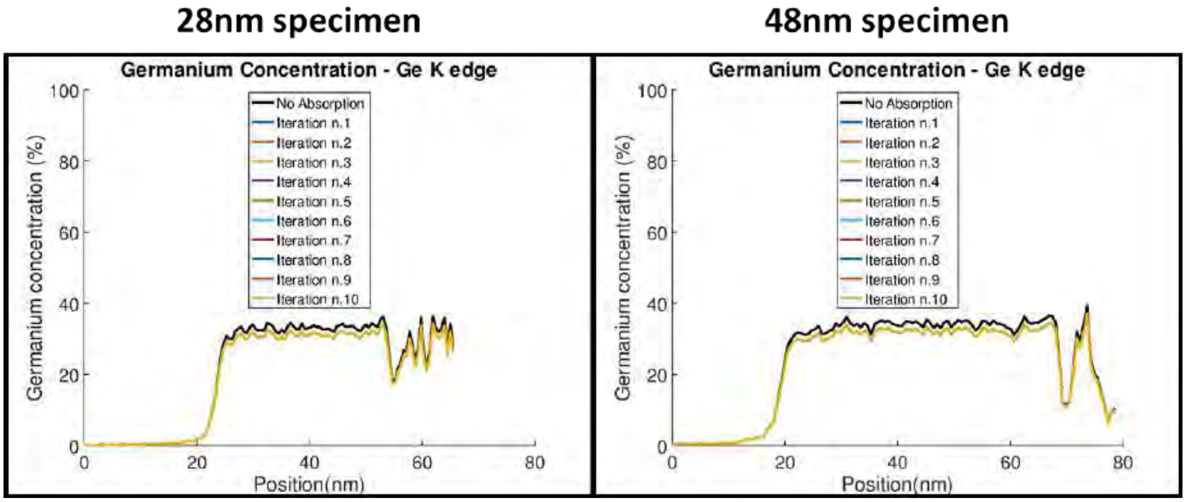

Figure 3.21: The result of the correction absorption for the first 10 iterations of the two calibration specimens.

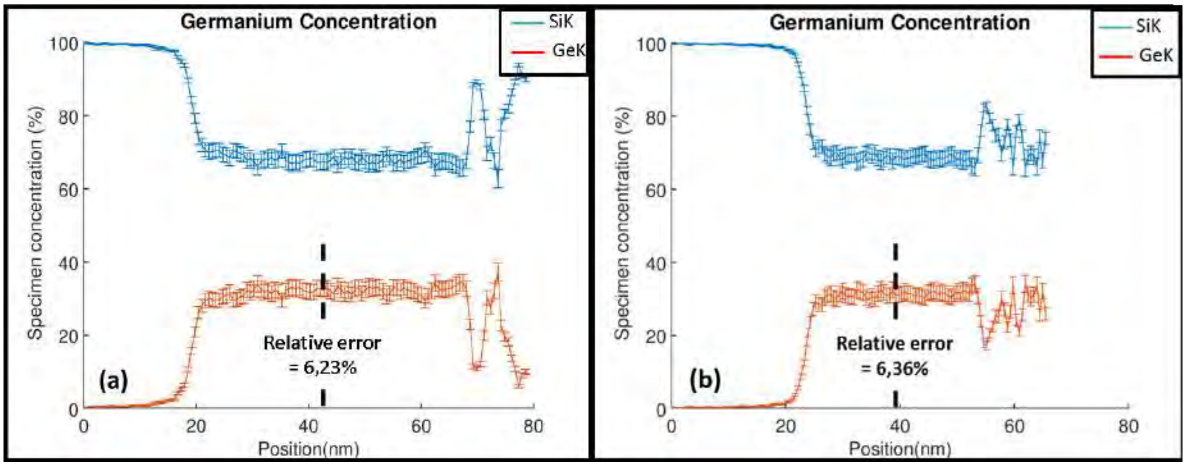

Figure 3.22: Plot of the measures Ge atomic fraction $f^{A}_{As}(x)$using K peaks for Si and Ge in the 48 nm (a) and 28 nm (b) specimen.

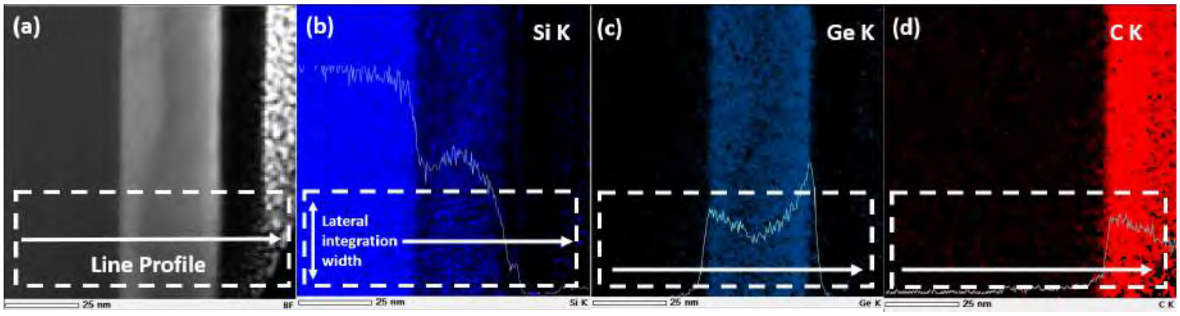

Figure 3.23: Bright field STEM images(a) and EDX intensity maps (b-c-d) obtained on a nanodevice. The K peaks have been used both for germanium and carbon to obtain the elemental maps shown in (c) and (d) from the EDX hyper-map. Intensities profiles obtained using a laterally averaged line-scan are superimposed to maps ((b), (c) and (d)). The direction and position for the line-scan as well as the lateral integration width are shown in figure (a), (b) and (c).

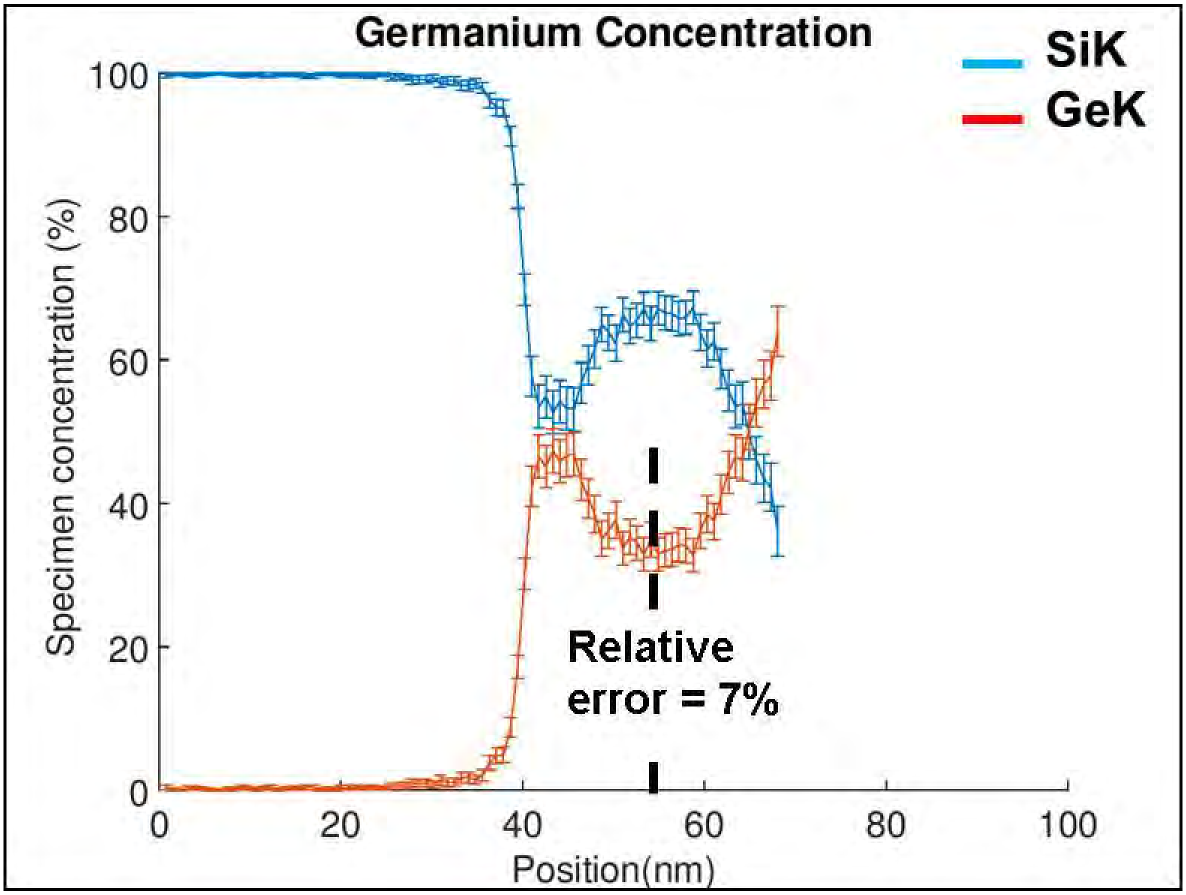

Figure 3.24: SiGe profile with experimental error obtained by applying the quantification method described in chapter 2.

Chapter 4

Additional research activity

In addition to the work described in the previous, I have participated during my Ph.D. to two additional research projects where my main contribution was associated to electron microscopy studies. The obtained results will be described in this chapter, together with a brief summary of the motivations.

The first project I have contributed to, dealt with the fabrication of optimized micro-supercapacitors by laser writing. My main contribution to this project was the study of the structure and composition of the obtained layers to confirm the validity of the fabrication technique and understand the super-capacitor properties.

The second project was focused on the fabrication of vertical nanowire transistors with a surrounding grid. My work in this project concentrated on the characterization of the platinum sillicide layers formed during the fabrication of Pt metal contacts by HREM and EDX.

Since the work presented in this chapter has been carried out before or during the development of the model presented in chapter 2, all the treatment of EDX data presented in the following have been obtained using standard quantification software (Analysis Station by JEOL and Esprit by Bruker).

4.1 Results obtained in the micro-supercapacitors study

4.1.1 Project motivation and description

Smart wearable systems have attracted a growing interest in the last past years to support the development of sensor networks and communicating objects called the (IoT). IoT is a generic term used to describe the exchange of data between portable, smart and connected devices [52, 53] creating a new range of devices able to interact and communicate through the internet. Applications relying on wearable devices such as healthcare, smart clothes or electronic papers have motivated many research works to achieve for instance individual management and continuous monitoring of patients [54].

Reliable micro-sized energy storage sources (ESS) such as batteries and Electrochemical Capacitors (ECs) are needed to power these devices [55, 56, 57]. ECs and batteries are complementary ESS covering a broad range of applications. While batteries can deliver low power for long time (tens of hours), ECs are suitable for delivering high peak current or power for short times (up to tens of seconds), making them promising candidates to power smart wearable systems [58, 59]. Screen-printing of carbon [60] and pseudocapacitive materials [61] or stamping processes [62] were reported with limited areal capacitance (< 20 mF.cm^{-2}) or resolution. Similarly, micro-devices prepared from Atomic Layer Deposition (ALD) , reactive sputtering and electron beam evaporation [63] techniques suffer from a poor areal capacitance (few mF.cm^{-2}) due to the small electrode thicknesses ($<$100 nm).

Wet processing routes, such as electrodeposition [64, 65] or electropolymerization [66], are suitable for preparing thick electrodes (> 50 µm) on flexible substrates with capacitance exceeding 10 mF.cm^{-2}. However, these multi-step wet processing routes are not fully compatible with the techniques used in the semi-conductor industry and are therefore difficult to upscale.

Laser-writing process focused a lot of interest these past years for preparing electrodes for energy storage applications. Following pioneer work from Arnold et al [67], laser irradiation was used to reduce graphite oxide (GO) into laser-scribed graphene (LSG) [68] or to achieve direct conversion of polyimide (PI) substrates into laser-induced graphene (LIG) [69, 70, 71] with a limited areal capacitance (< 20 mF.cm^{-2}).

Ruthenium oxide exhibits one of the highest gravimetric capacitance (1450F.g^{-1}) together with decent electrical conductivity (from 4 to 46S.cm^{-1} depending on the hydration rate of RuO_2) [72]. Since the realization of micro-supercapacitors requires only a limited amount of RuO_2, typically less than 1mg.cm^{-2}, the cost is not that much an issue [73]. Therefore, Kaner's group recently adapted their GO laser-scribing method to prepareLSG/RuO_2based flexible micro-supercapacitors fromGO/$RuCl_3$mixture [74]. Laser irradiation of the mixture coated onto flexible substrate led to simultaneous reduction of GO into LSG and Ru(+III) oxidation into Ru(+IV). However, the small RuO_2 weight loading that could be achieved by this method – about 90µg.cm^{-2} – limited the areal and volumetric capacitance of the device to 10mF.cm^{-2} and 11 F.cm^{-3}, respectively, in 1M H_2SO_4 (estimated from Ragone plot). In addition, such oxidation dependent process is not convenient for the preparation of every carbon- (microporous carbon), metal oxide- (Nb_2O_5, MnO_2 for example, for which a specific morphology has to be obtained) or phosphates-based electrodes ($LiFePO_4$), as the final active material is obtained from the transformation of a precursor under the laser beam. Differently, the present work reports about the preparation of RuO_2-based micro-supercapacitors from the direct laser-writing of a commercial $RuO_2.xH_2O$ powder. For this, powder-containing ink spin-coated onto an electrically insulating flexible polyimide film, which does not need the design of masks or controlled atmospheres. This process, which results in the preparation of stable electrodes with improved mechanical properties, can be extended to other materials such as metal oxides, carbons or phosphates to design a large variety of micro-devices for various applications.

In the following, we will give a description of the RuO_2 specimen preparation, then we will detail the electron microscopy study and its importance in this work.

4.1.2 Description of the samples

Figure 4.1 shows the fabrication process of the RuO_2-based micro-supercapacitors onto a polyimide (PI) flexible substrate. An ink containing a mixture of a tetrachloroauric acid ($HAuCl_4.3H_2O$) gold precursor and cellulose acetate dissolved in tetrahydrofurane (THF) is spin-coated onto the flexible substrate (layer 1).In a second step, a $RuO_2.1.8H_2O$ commercial powder dispersed in THF is deposited by spin-coating (layer 2) onto the layer 1.Then, laser-writing was performed on the bilayered $HAuCl_4.3H_2O$ / RuO_2 film with a UV laser (wave length of 405 nm) with a spot size of 5μm.When the bilayered film was deposited, laser-writing was performed at 116 mW with a writing speed of 3 ± 1 $mm.s^{-1}$. After washing in acetone and ethanol, mechanically stable patterned electrodes adhering to the flexible PI film were obtained.

4.1.3 Electron microscopy characterization

The facile laser-writing procedure developed in this work was used to make RuO_2-based electrodes on a polyimide substrate. To understand the role of the $HAuCl_4.3H_2O$ transition layer, the cross-section of an electrode was prepared by cross-polishing[1]. Indeed, capacitance was very limited without the Au precursor, i.e. the Ru amount deposited on polyimide was too small.

SEM images (obtained using secondary electrons) representative of the as-prepared laser-scribed RuO_2electrodes reveal that the film covers entirely the flexible substrate (figure 4.2A). The deposit grows as small crystals and some popcorn-like structures can also be locally observed, accounting for about 20% of the total surface (figure 4.2B). These crystals form a homogeneous and dense structure onto the substrate as observed in figure 4.2C (top view) and figure 4.2D (cross section). In figure 4.2E is shown a cross sectional view obtained using SEM in backscattered electrons mode, representative of the deposit, which reveals the bi-layered aspect of the deposit (the tilt angle between the observation axis and the specimen surface is 54°). The popcorns start to grow from the RuO_2 crystals; such structure might be due to a local over-heating during the laser-writing process. EDX mapping allowed us to show the presence of oxygen and ruthenium in both layers, but it can be clearly observed that the oxygen concentration is much higher in the 500 nm-thick layer containing the pillars (figure 4.2F), in comparison with the thin interface layer at the PI film / RuO_2 pillars. This suggests that the upper layer is composed by RuO_2 while the lower one could be mainly composed by metallic Ru. In addition, figure 4.3A shows that several Au nanoparticles are visible in the RuO_2 layers, which are likely to enhance the electrical conductivity of the RuO_2. XRD measurements confirmed the presence of crystalline RuO_2 (figure 4.3B) as well as Au

---

[1] See http://www.gatan.com/products/sem-specimen-preparation/pecs-ii-system

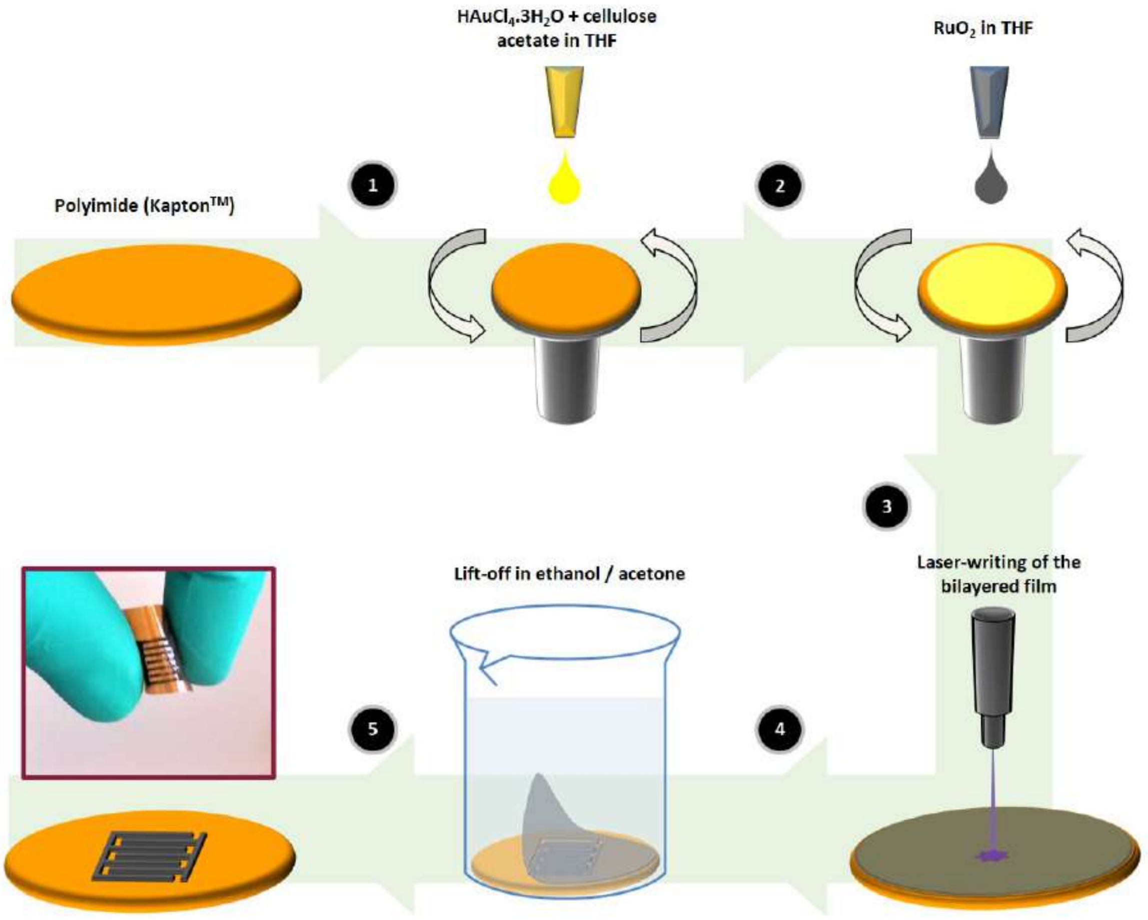

Figure 4.1: **Fabrication process of** RuO_2**-based flexible micro-supercapacitors**. $HAuCl_4.3H_2O$ / cellulose acetate mixture (1) and RuO_2 (2) are dispersed in THF and successively spin-coated on polyimide. Laser-writing is performed on the as-deposited bilayered film (3) and the non-exposed areas are removed by washing with ethanol and acetone (4) to reveal the interdigitated electrodes (5).

and Ru metals, which is compatible with the presence of a metallic Ru/RuO_2 stack suggested by the EDX maps.

To obtain a better understanding of the microscopic structure, cross-sectional TEM specimens were prepared by FIB and observed by TEM. The TEM cross sectional view presented in figure 4.4 allowed us to obtained a local perspective of the crystalline structure observed by SEM. Some rare “popcorn-like” structures starting from a dense layer containing small pillars lying on a thin porous layer (figure 4.4A) are dispersed on the surface. Figure 4.4B as well as the high resolution TEM of the RuO_2/ PI substrate interface presented in figure 4.4C show that the first 100 nm-thick porous layer contains particles randomly oriented. The Fourier transform of some particles of the image in figure 4.4C, displayed in inset, shows that the crystalline structure of the single particles

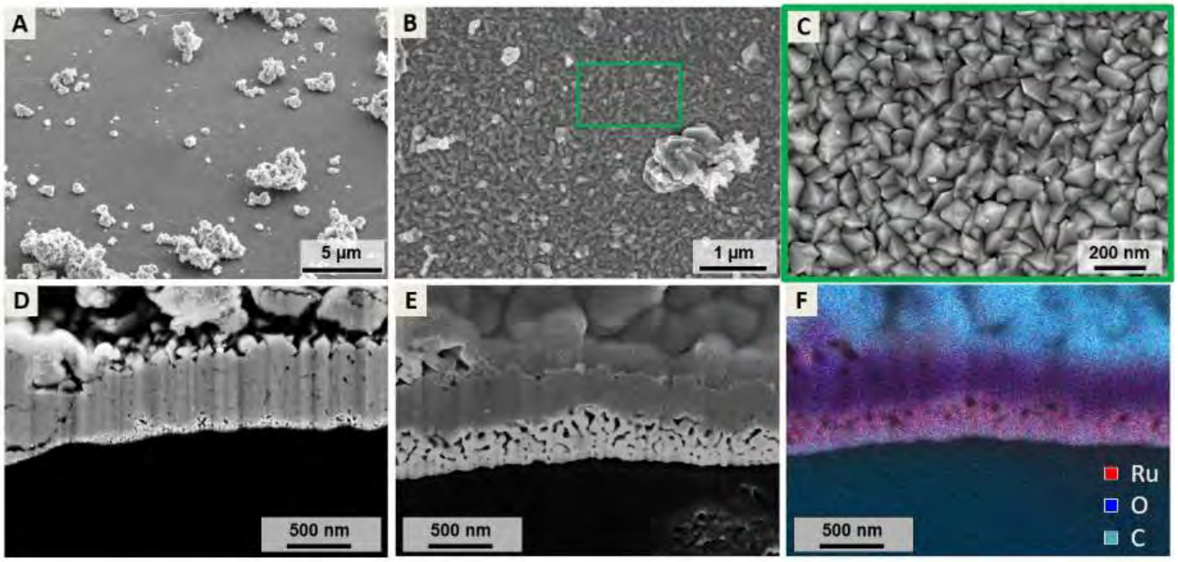

Figure 4.2: Structure of the Au/RuO2 growing under laser beam. (A) Tilted and (B) top view of the Au/RuO$_2$ deposited on KaptonTM and (C) zoom on the RuO$_2$ crystals. (D) Cross-sectional view of the Kapton^{TM}/laser-scribed Au/RuO2 with (E) tilted SEM image obtained using backscattered electrons and the corresponding EDX map (F) evidencing the presence of Ru at the interface. The large 50° tilt angle used in Figure E and F to highlight the porous layer prevent from using reliable scale bar.

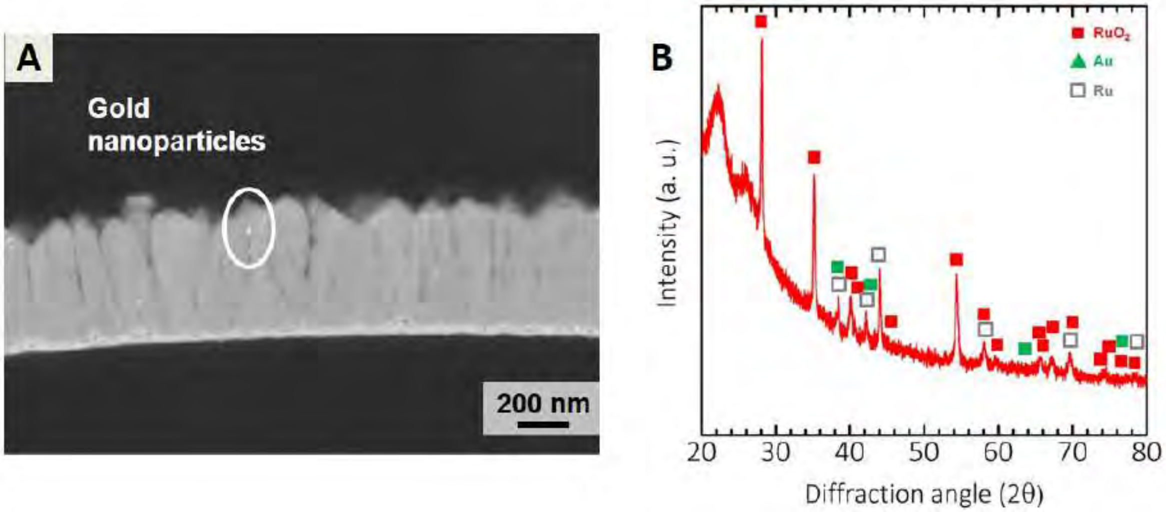

Figure 4.3: Characterization of the RuO$_2$-based electrodes. (A) Cross sectional view of the Kapton^{TM}/Ru/RuO2 prepared by Cross Polisher technique. (B) XRD pattern of the laser-scribed Au/RuO2 deposited on PI flexible substrate without Ti/Au current collector.

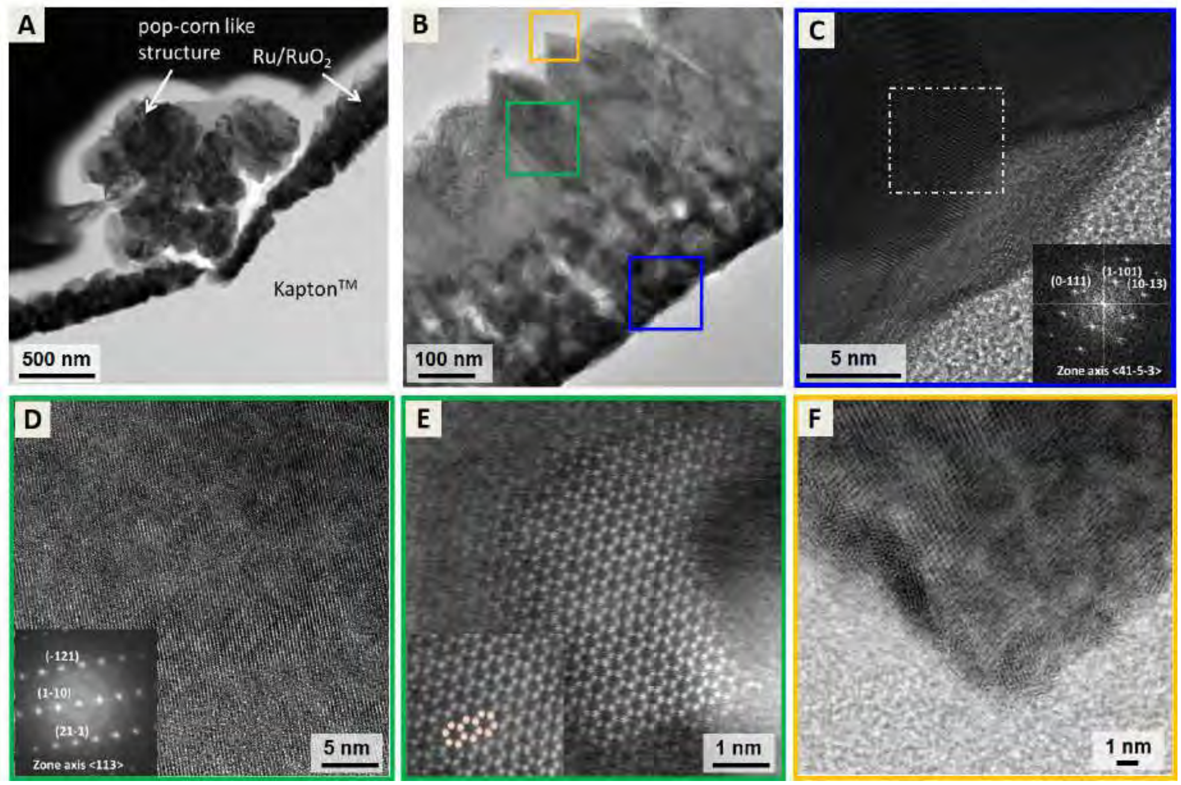

Figure 4.4: Observation of the Kapton^{TM}/ RuO_2 interface. TEM image of (A) a pop-corn like structure grown (B) on the Ru/ RuO_2 at the interface with the flexible substrate. High resolution TEM image of (C) the RuO2/KaptonTM interface; the inset shows the Fourier transform of the image in the dotted rectangle. (D) Morphology of the RuO_2, with a Fourier transform of the full image as an inset and (E) Ru contained in the pillars (the inset shows the superposition of the hexagonal ruthenium structure in a <0001> orientation and a region of the image). (F) Bright-field TEM observation of the top of the pillars.

is compatible with the structure of metallic Ru (hexagonal compact P63/mmc, a = b = 270 pm, c = 427.5 pm). Inside the pillars, single crystal patterns are obtained in this region, indicating that the process induced a polycrystalline growth with all the domains oriented in the same direction, mainly composed by RuO_2, with the presence of Ru inclusions. Indeed, Fourier analysis performed on different particle inside the pillar region shows patterns compatible both with tetragonal RuO_2 (quadratic P4/2mnm a = b = 452 pm, c = 311.6 pm) and hexagonal Ru (figure 4.4D and figure 4.4E respectively). Surface faceting is another indication of the regular and monocrystalline character of the pillar growth. However, the presence of several nanoparticles of top of them prevent a precise identification (see figure 4.4F). It is worth mentioning that Au nanoparticles were also found in the porous layer (EDX analysis, figure 4.5A and figure 4.5B). In summary, the laser-writing of the bi-layered $HAuCl_4.3H_2O$- cellulose acetate / RuO_2

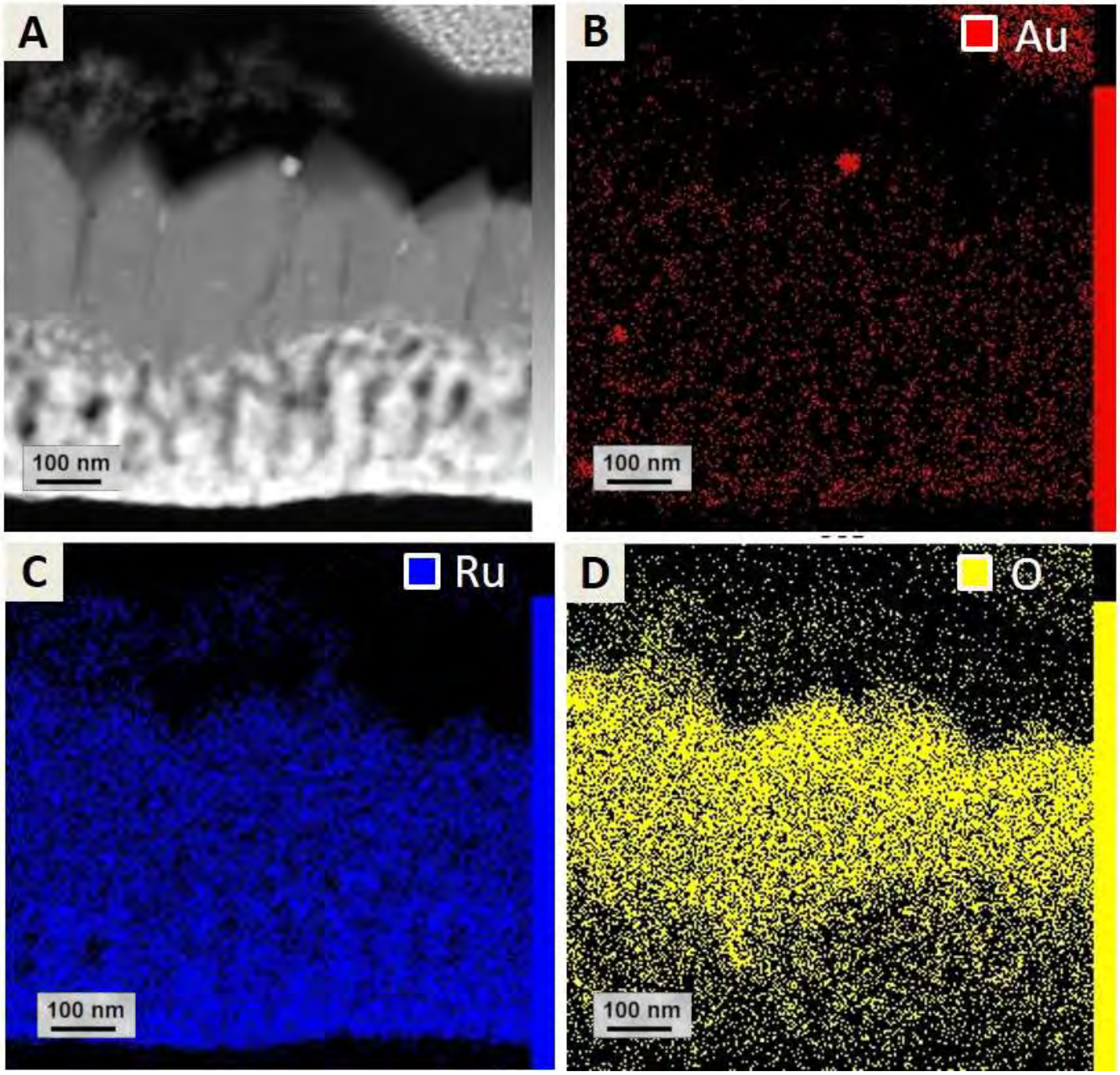

Figure 4.5: EDX analysis of the flexible substrate / laser scribed electrode interface of 4.4 Analysis shows that there is a higher O concentration in the upper region compared with the lower region. This is compatible with a Ru (lower) /RuO_2 (upper) stacking. Au is present in the layers in nanoparticle form.

leads to a 500 nm-thick deposit containing a layer of metallic Ru, and a second layer of Ru/ RuO_2 pillars (figure 4.5C and figure 4.5D) embedding Au nanoparticles.

4.2 Results obtained in the vertical nanowire transistors study

4.2.1 Project motivation and description

One of the most limiting factors to follow Moore's law is the short channel effect that affects planar devices and can be reduced by adopting new architectures. In this project a specific architecture capable of reducing this kind of effects has been studied: the NanoWire Field Effect Transistors "NWFETs" [75](see figure 4.6).

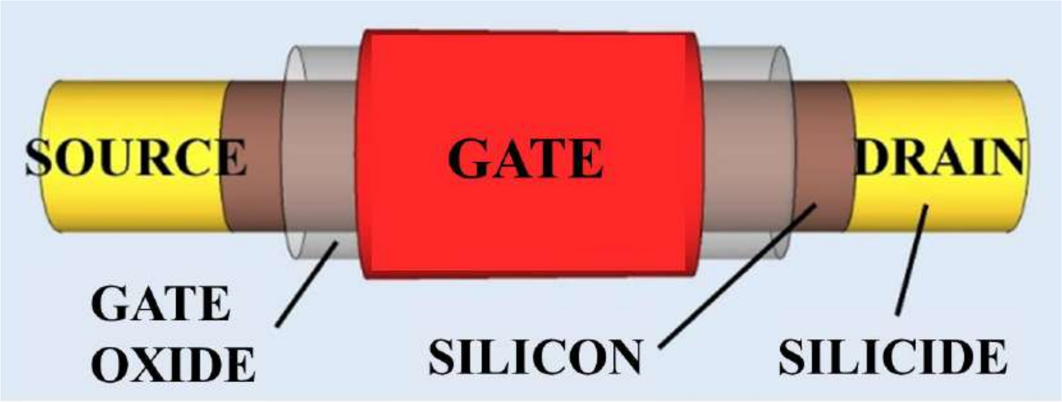

Figure 4.6: Diagram of a silicon nanowire transistor (NWFET).

The Si-NWFET silicon vertical nanowire technology is a promising breakthrough architecture for the next technological nodes and its advantages over conventional architecture are remarkable (see figure 4.7):

- A surrounding gate allowing optimal electrostatic control of the channel.
- An increase in the density of transistors per unit area due to the vertical structure of NWFETs.

However, like any technological breakthrough, an optimization phase is essential in order to first identify the axes of improvement of the new architecture and, secondly, to establish strategies to understand and solve them. In the case of NWFETs, there is still a lack of understanding regarding the formation of metal contacts, still with a view to reducing access resistance. Indeed, the usual procedure for forming these contacts is based on a rapid annealing (RTA) at around 300° C after deposition of a platinum film on silicon of a few tens of nanometers until the silicide PtSi is obtained.

PtSi is not the only phase to come into play during the silicon-platinum [76, 77] inter-diffusion.

It is possible to obtain mainly 3 phases: PtSi, Pt_2Si and Pt_3Si. The parametrization and the understanding of the mechanisms that take place in the silicidation reaction are

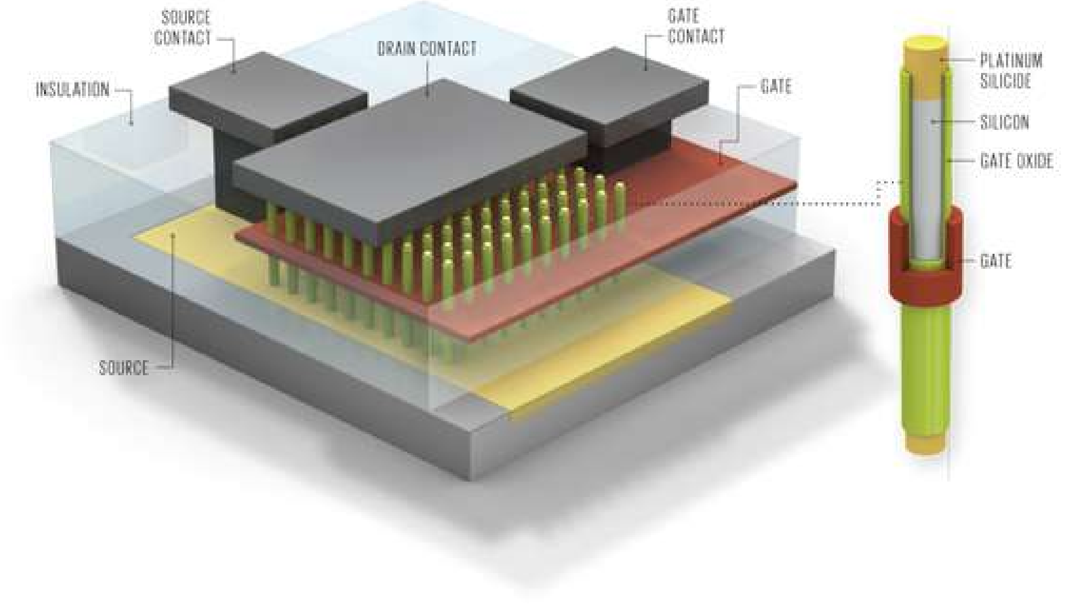

Figure 4.7: Diagram of a NWFET and network architecture with grid, insulators and common contacts taken from the "Nanowire Gate All Around Transistors" article of the nextBIGFuture site and inspired by [75].

critical because the intermediate alloy phases are unfavorable to the creation of metal contacts.

In the case of a bulk substrate, the parameters and mechanisms of platinum silicidation are known and, in the case of horizontal nanowire structures, have been recently investigated [77, 78, 79]. However, these studies do not make it possible to apprehend the impact of the "ultimate" size reduction on the silicidation reaction.

The observations made by [80] revealed a non-negligible variation in the kinetics of reaction of the platinum-silicon system when the dimensions involved are reduced to the extreme. Indeed, the idea of this work was to achieve and characterize the metal contacts of vertical nanowires transistors with a progressively decreasing diameter (from 60 down to 12 nm). In particular, we wanted to achieve a better phenomenological understanding of the silicidation reaction. For that, electron microscopy has been used to investigate the existence of several phases in the nanowires. In order to validate the results, TEM-EDX analysis has been coupled with HRTEM crystallographic analysis.

4.2.2 Electron microscopy characterization

Vertical silicided nanowires are manufactured in several stages (see figure 4.8). Firstly, the silicon nanowires are created by Reactive Ion-etching (a), then an anisotropic platinum layer of 15nm is deposited by electron beam evaporation (PLASSYS MEB 550S) (b) and finally, the silicidation reaction is thermally activated by rapid annealing under hydrogenated nitrogen N2: H2 (95: 5) (c).

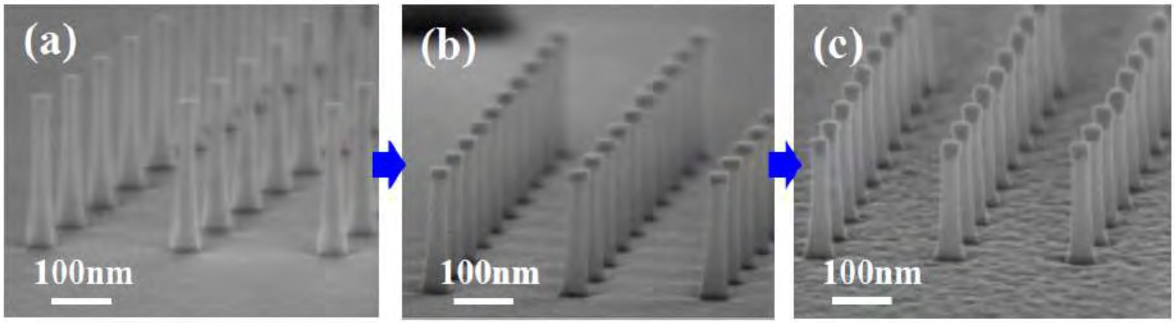

Figure 4.8: Process for producing platinum silicides on a network of vertical silicon nanowires with a diameter of 32 nm and a height of 215 nm. (a) RIE etching, (b) deposition of a platinum layer, (c) after RTA at 350 °C for 3 minutes under H_2N_2 from [80].

In order to remove the unreacted metal from the walls of the nanowires, a final step of chemical etching with aqua regia is necessary. Two samples annealed at two different temperature (500°C and 350°C) have been used for this study. Each sample contained several series of nanowires with different diameters (see figure 4.9) in order to verify the impact of the nanowire size on the final silicide structure and composition.

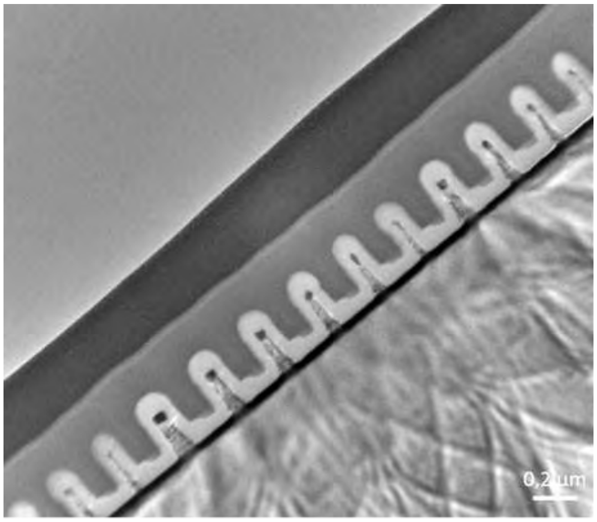

Figure 4.9: Schematic showing different thicknesses of the nanowires.

For TEM observations, the specimens have been prepared by FIB. HRTEM coupled with Fourier analysis has been used to study the nanowire structure. Lattice plane distances and angles have been extracted using the Fast Fourier Transform method and compared to the silicided phases data. This has allowed us to isolate the silicide structures compatible with HRTEM observations in various nanowire regions. Then, these results have been compared to the EDX quantification of the STEM/EDX images in order to confirm the composition of the samples.

The crystallographic analysis was carried out by using Digital Micrograph and Carine Crystallography. The observed Fourier patterns have been compared with the theoretical patterns of PtSi, Pt_2Si and Si structure obtained using the kinematic approximation [3].

The crystalline structure of the the PtSi phases are reported in table 4.1.

Alloy	**Space Group**	**Lattice Parameters (A)**	**Atomic Positions**
Pt Si	Pbnm	a=5.932, b=5.595, c=3.603	$Pt\left(0.195, 0.01, \frac{1}{4}\right)$ $Si\left(0.59, 0.195, \frac{1}{4}\right)$
Pt_2Si	I4/m mmm	a=3.948,b=5.936	$\mathrm{Si}(0,0,0)$, $\mathrm{Pt}\left(0, \frac{1}{2}, \frac{1}{4}\right)$

Table 4.1: Crystalline structure of PtSi phases

Figure 4.10 shows an example of the comparison between the experimental Fourier pattern obtained from a HRTEM image and the theoretical diffraction pattern obtained by the software Carine. The image was obtained on a nanowire annealed at 500°C for 3 minutes.

The Fourier transform analysis allowed us to confirm that this nanowire structure is compatible with that of a PtSi crystal imaged through a triclinic <0 1 0> zone axis. It can also be shown that PtSi this is the only structure compatible with the observed pattern.

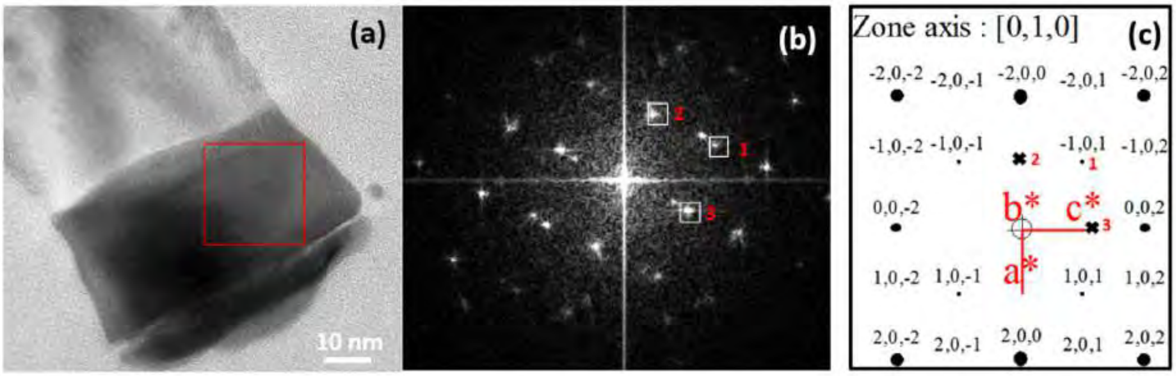

Figure 4.10: HRTEM of the 53nm Nanowire annealed at 500°C (a), Fourier transform obtained using Digital Micrograph in the selected region and theoretical diffraction pattern obtained with the software Carine (c). The spot represented by a cross, corresponds to double diffraction spots.

The EDX quantification results obtain on the same nanowire are shown in figure 4.11. We can see that, within the experimental errors, the ratio between the Pt ans the Si atomic concentrations is close to unity, confirming the formation of the PtSi structure in several regions of the nanowire (see figure 4.12).

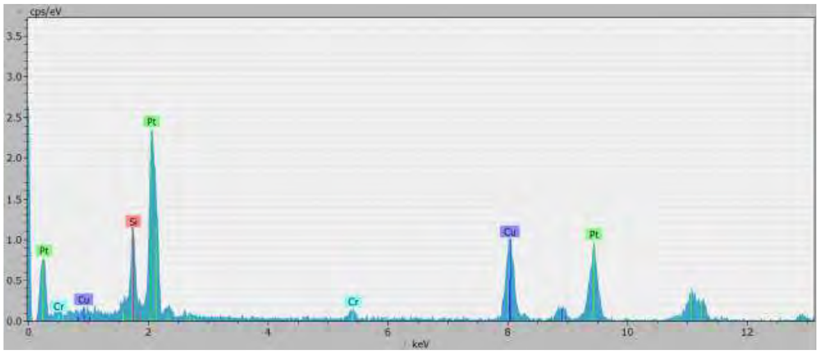

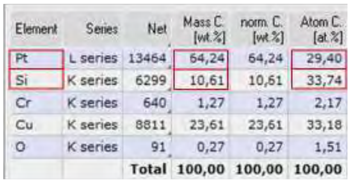

Element	Series	Net	Mass C. [wt.%]	norm. C. [wt.%]	Atom C. [at.%]
Pt	L series	13464	64,24	64,24	29,40
Si	K series	6299	10,61	10,61	33,74
Cr	K series	640	1,27	1,27	2,17
Cu	K series	8811	23,61	23,61	33,18
O	K series	91	0,27	0,27	1,51
		Total	**100,00**	**100,00**	**100,00**

Figure 4.11: EDX spectrum obtained in the zone shown in figure 4.10(a) and corresponding quantification results.

The combination of HRTEM and STEM/EDX measurements has been used to characterize the formation of different phases in the nanowires contact obtained using 350°C annealing.

Specimen annealed at 350°C

To study the impact of nanowire size on the silicidation kinetics, the structure of the silicide regions has been studied in wires of different sizes. The results obtained for a 50 nm wire are shown in figure 4.13. The analysis show that the whole contact region has a PtSi structure.

The results obtained on a thinner nanowire with a 13 nm diameter are shown in figure 4.14 and figure 4.15).

In this case a PtSi region (see figure 4.14) as well as a Pt_2Si region through a tetragonal <1 1 0> zone axis (see figure 4.15) can be identified by HRTEM and STEM/EDX. The combined analysis has allowed us to obtain the dimensions of the regions associated to each different phase.

A summary of the results obtained on nanowires of different diameter is reported in figure 4.16. It can be observed that in larger nanowires, PtSi regions are larger than Pt_2Si regions while the opposite situation is found in smaller nanowires. Moreover, the Pt_2Si phase is always found in the region closer to the nanowire tip. This results can be interpreted assuming that Pt diffuses sufficiently fast in large nanowires to allow the formation of a uniform PtSi phase in the whole silicide region. In contrast, if Pt diffusion is reduced in smaller nanowires the diffusion is slower, only the region close to the interface with the Si substrate can go through the entire reaction sequence and form the PtSi phase, while the region close to the nanowire the tip (where the initial Pt "reservoir" is located) remains richer in Pt, resulting in the formation of the intermediate Pt-rich Pt_2Si phase.

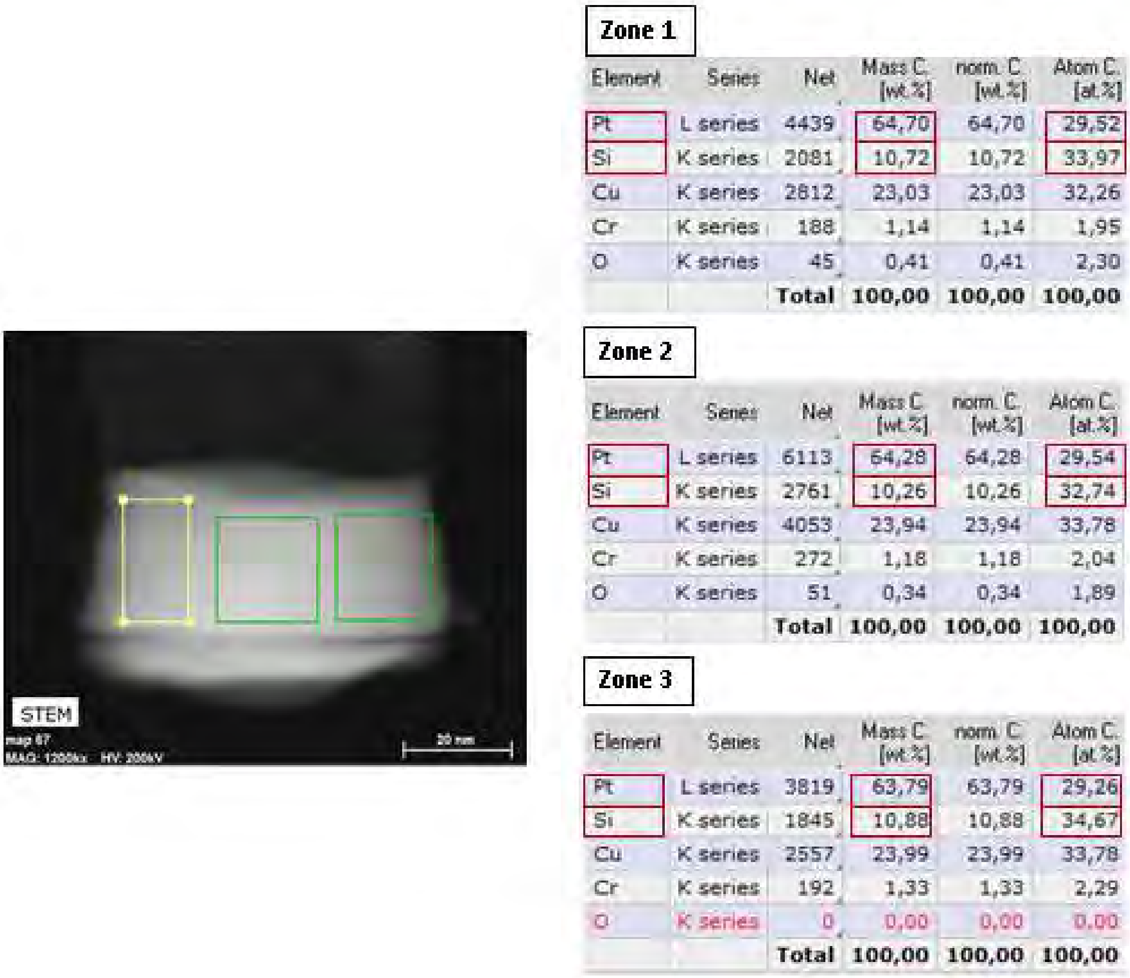

Zone 1

Element	Series	Net	Mass C. [wt.%]	norm. C. [wt.%]	Atom C. [at.%]
Pt	L series	4439	64,70	64,70	29,52
Si	K series	2081	10,72	10,72	33,97
Cu	K series	2812	23,03	23,03	32,26
Cr	K series	188	1,14	1,14	1,95
O	K series	45	0,41	0,41	2,30
		Total	100,00	100,00	100,00

Zone 2

Element	Series	Net	Mass C. [wt.%]	norm. C. [wt.%]	Atom C. [at.%]
Pt	L series	6113	64,28	64,28	29,54
Si	K series	2761	10,26	10,26	32,74
Cu	K series	4053	23,94	23,94	33,78
Cr	K series	272	1,18	1,18	2,04
O	K series	51	0,34	0,34	1,89
		Total	100,00	100,00	100,00

Zone 3

Element	Series	Net	Mass C. [wt.%]	norm. C. [wt.%]	Atom C. [at.%]
Pt	L series	3819	63,79	63,79	29,26
Si	K series	1845	10,88	10,88	34,67
Cu	K series	2557	23,99	23,99	33,78
Cr	K series	192	1,33	1,33	2,29
O	K series	0	0,00	0,00	0,00
		Total	100,00	100,00	100,00

Figure 4.12: Diagram showing the quantification results for different zones on the 53 nm Nanowire annealed at 500°C.

In summary, combined HREM and STEM/EDX analysis has allowed us to show that, during silicidation, Pt diffusion in Si nanowires depends on the nanowire size. Diffusion is faster in nanowires with a larger diameter and decreases with the nanowire size. The reason beyond this variation is currently unclear and will be the object of further studies.

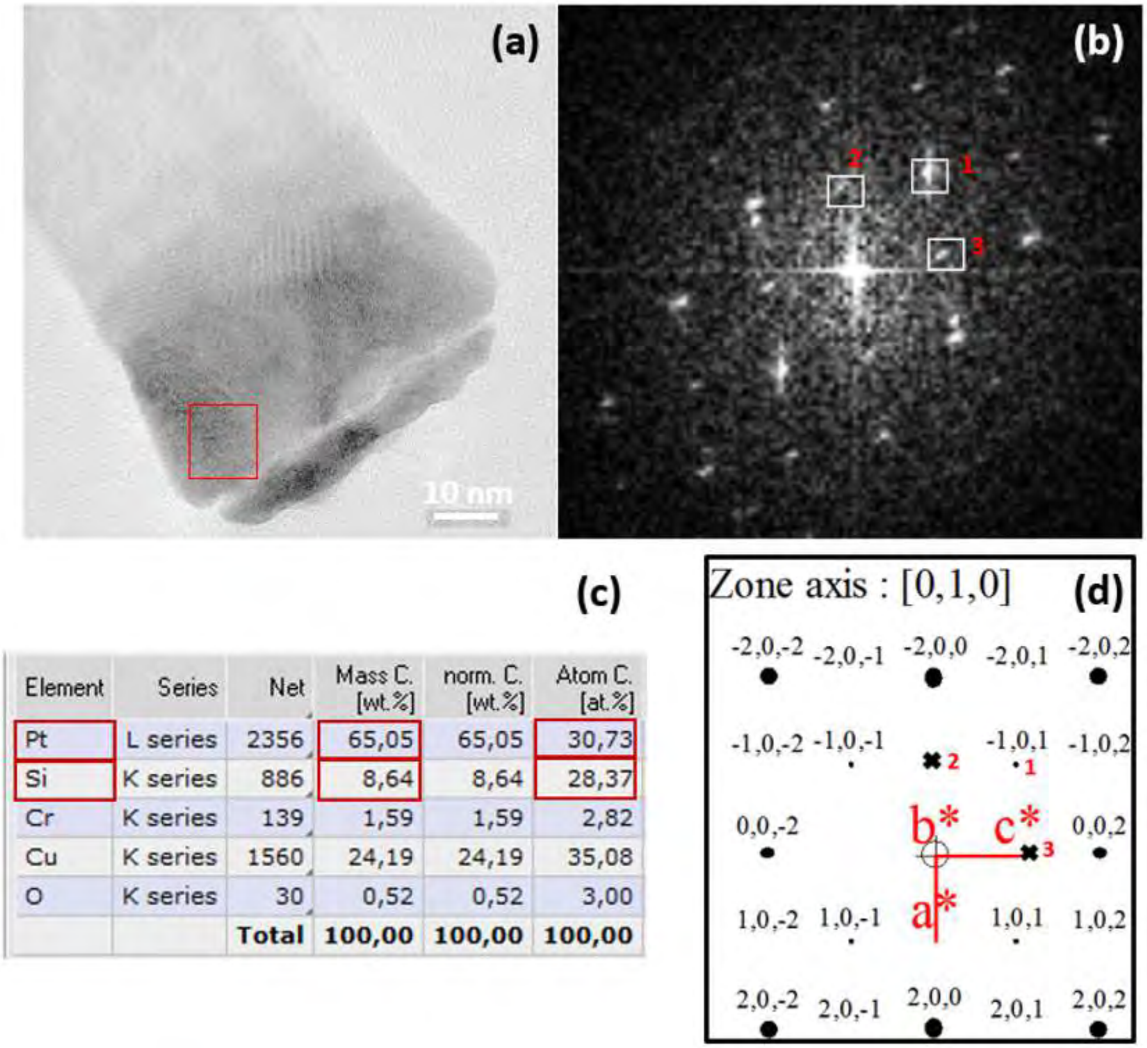

Element	Series	Net	Mass C. [wt.%]	norm. C. [wt.%]	Atom C. [at.%]
Pt	L series	2356	65,05	65,05	30,73
Si	K series	886	8,64	8,64	28,37
Cr	K series	139	1,59	1,59	2,82
Cu	K series	1560	24,19	24,19	35,08
O	K series	30	0,52	0,52	3,00
		Total	**100,00**	**100,00**	**100,00**

Figure 4.13: HRTEM of a 50nm Nanowire annealed at 350°C (a), Fourier transform of the selected region (b), specimen composition obtained by STEM/EDX in the same region (c) and theoretical diffraction pattern corresponding to the Fourier transform (d). The spot represented by a cross, corresponds to double diffraction spots.

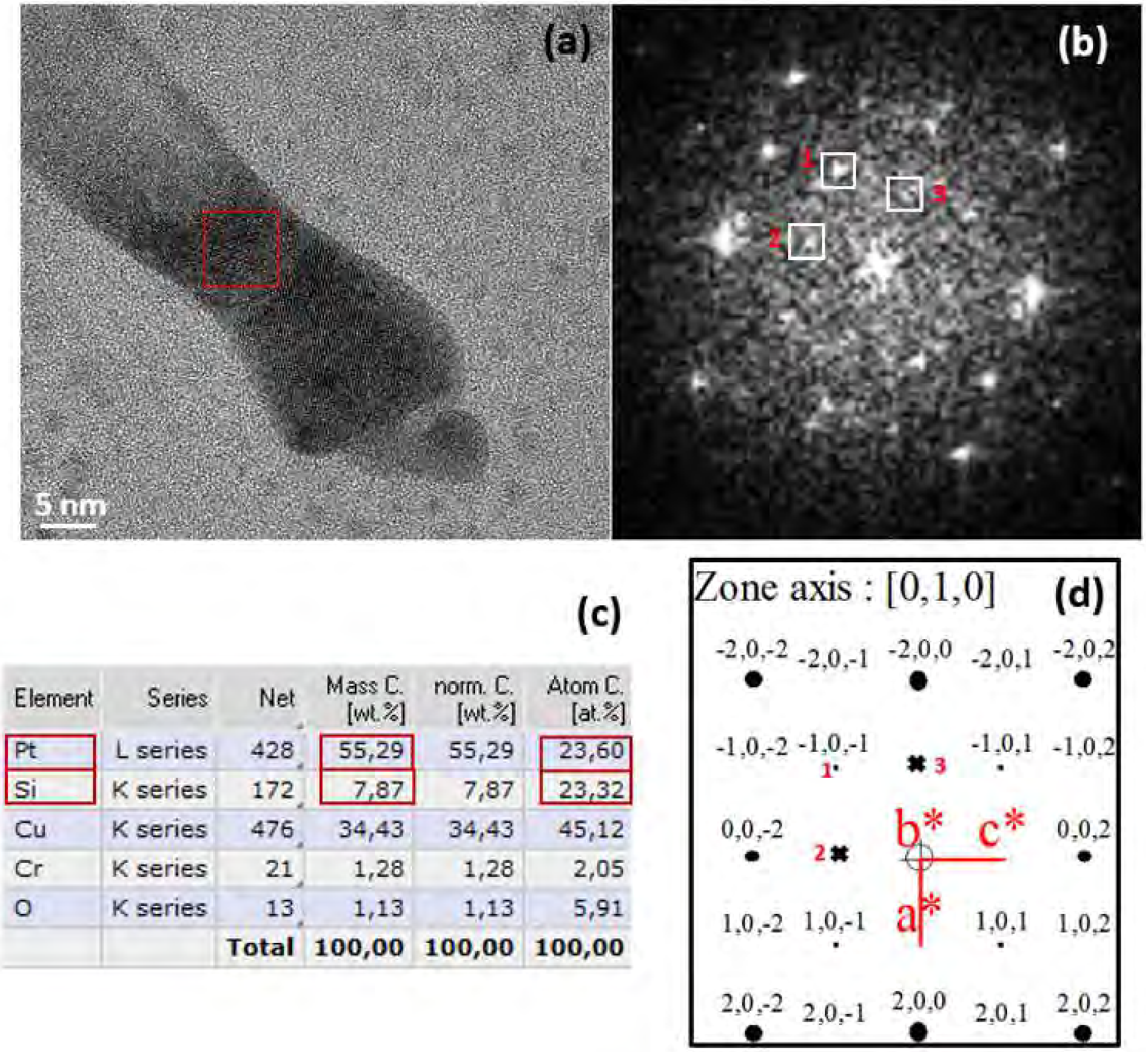

Element	Series	Net	Mass C. [wt.%]	norm. C. [wt.%]	Atom C. [at.%]
Pt	L series	428	55,29	55,29	23,60
Si	K series	172	7,87	7,87	23,32
Cu	K series	476	34,43	34,43	45,12
Cr	K series	21	1,28	1,28	2,05
O	K series	13	1,13	1,13	5,91
		Total	100,00	100,00	100,00

Figure 4.14: HRTEM of a 13 nm Nanowire annealed at 350°C (a), Fourier transform of the selected region (b), specimen composition obtained by STEM/EDX in the same region (c) and theoretical diffraction pattern corresponding to the Fourier transform (d). The spot represented by a cross, corresponds to double diffraction spots.

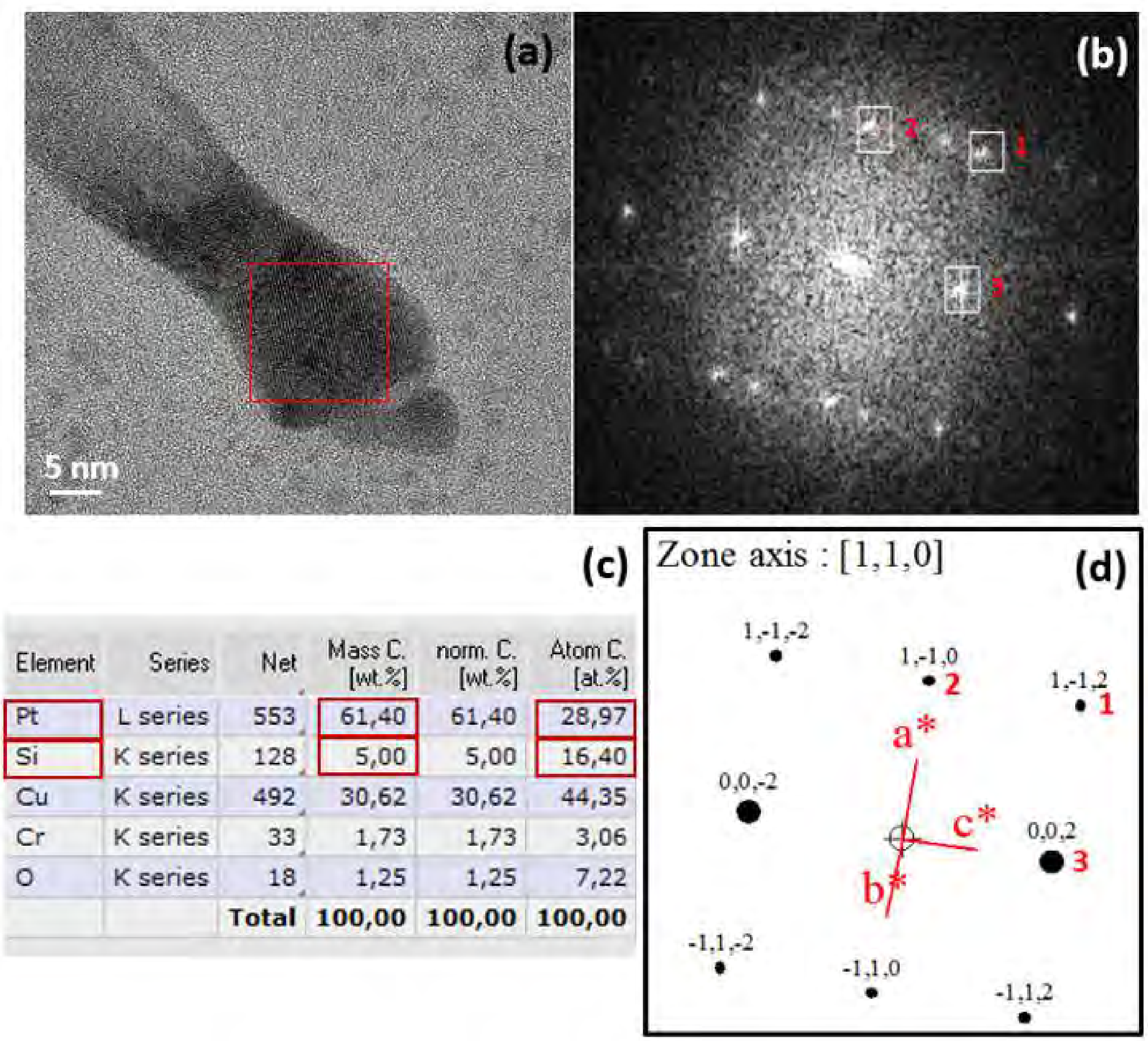

Element	Series	Net	Mass C. [wt.%]	norm. C. [wt.%]	Atom C. [at.%]
Pt	L series	553	61,40	61,40	28,97
Si	K series	128	5,00	5,00	16,40
Cu	K series	492	30,62	30,62	44,35
Cr	K series	33	1,73	1,73	3,06
O	K series	18	1,25	1,25	7,22
		Total	**100,00**	**100,00**	**100,00**

Figure 4.15: HRTEM of a 13 nm Nanowire annealed at 350°C (a), Fourier transform of the selected region (b), specimen composition obtained by STEM/EDX in the same region (c) and theoretical diffraction pattern corresponding to the Fourier transform (d).

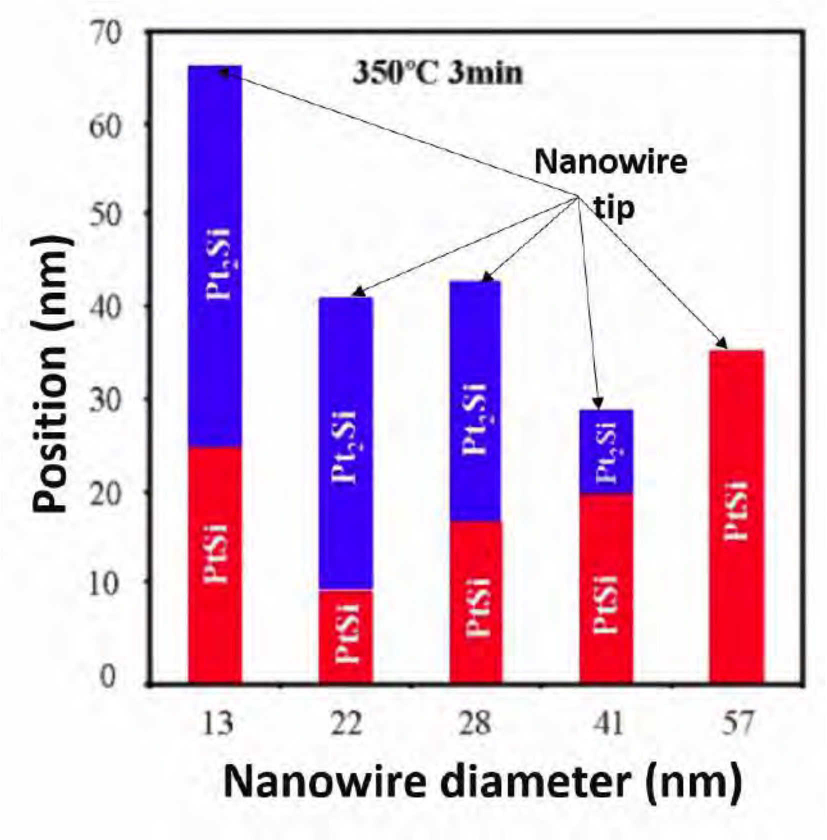

Figure 4.16: Diagram resuming the height of silicide phases for different diameters of nanowire annealed at 350°C.

Conclusion

The main objective of this thesis was to develop an improved Cliff-Lorimer method for the quantification of EDX elemental maps in semiconductor materials, with the specific aim to allow reliable measurements in the case of low concentrations of dopant impurities (below 1 at. %).

For that, different electron microscopy techniques have been presented in the first chapter including their main peculiarities and advantages. In addition, the STEM/EDX technique and the related quantification methods have been discussed in detail. Finally, the quantification procedures available in commercial softwares, and specifically the X-ray absorption correction and the calibration of the C-L factors have been presented, allowing us to identify their main weaknesses.

Our improved model was then presented in the second chapter. The study started with the iterative calculation of the X-ray absorption in the specimen, which depends on the density, the mass absorption coefficient and the specimen thickness. In particular, we showed that there is no universal formula for the expression of the density as a function of the specimen composition. For this reason, we developed an appropriate approximation of the relation between the density and the specimen composition for each investigated materials system. In particular, the cases of amorphous solids and of pseudomorphic alloys were studied. We then detailed the procedure we used for the experimental calibration of C-L factors by comparison with absolute concentration measurements obtained by the RBS technique. Finally, in order to know the precision of our method, the last step was estimation of the total experimental error on the measured specimen concentration using the error propagation procedure.

The new algorithm, with all its modifications compared to the existing commercial softwares, has been tested in the third chapter, first on reference specimens and then applied to samples with unknown composition. A Silicon substrate doped with As by ion implantation has been used as a reference for the quantification of As dopant concentration (based on the "amorphous solid approximation" model), while a SiGe/Si stack was used for the quantification of Germanium (based on the "pseudomorphic alloy approximation"). The Gaussian shape of the Arsenic concentration profile allowed us to demonstrate that the absorption effect is more important on the high concentration region due to the high mass density of the specimen in this region. The calibration of the C-L factors was then performed by comparison with the RBS measurements carried out on the reference samples. The results show that the calibration on the K peak is more accurate than on the L peak. This is due to the L peaks being located in the low energy region of the X-ray spectrum where the intensity of the bremsstrahlung noise is comparable (or even stronger) than the characteristic peak to be analysed. The noise subtraction is therefore more difficult to achieve. Finally, we estimated the total experimental error affecting the EDX measurements. As expected, we found that this error is less important in the high As and Ge concentration regions, where the x-ray count is higher.

In the case of As doping, once the algorithm has been confirmed, we applied the calculation to a 3D FinFET test structure. We could demonstrate the validity of this technique for nanometric scale specimens, where the error is low enough to trust the measurement obtained with the new algorithm, down to concentrations below 1 at. % (the actual detection limit was estimated at 7.7x1019 cm-3). Finally, the exposition times needed to improve the detection limit have been calculated using the measured count rates. The results clearly suggest that, due to instabilities of the experimental setup, the resolution limit cannot be drastically improved by just increasing the measuring time.

In the fourth chapter, I reported the results obtained within some additional research projects carried out at the LPCNO and the LAAS laboratories. In these activities, X-ray quantification techniques (in SEM or STEM mode) are needed to support other TEM-based structural characterisations of nanoelectronics materials of interest in future nanometric MOS or IoT devices.

The first project focused on the fabrication of supercapacitors obtained by laser writing. The EDX measurements in particular the distribution mapping of the different elements in the layer allowed us to identify the phase and the structure of the specimen. That makes the EDX technique one of the important elements to understand the originality of the laser-writing fabrication method.

The second project concerned the fabrication of GAA (gate-all-around) nanowire-based transistors, where the fabrication process includes the formation of low resistivity PtSi silicide contacts obtained by Pt deposition and subsequent annealing. Our results, obtained by HREM and FFT method, evidenced an impact of the nanowire diameter (and the annealing temperature) on the silicide formation mechanism. In particular, for high temperature annealing and large nanowire diameters, the expected PtSi crystallographic structure was found. In contrast, when the nanowire diameter (or the annealing temperature) are decreased, a Pt2Si structure is obtained on the top surface of the nanowire, while the low resistance PtSi phase is obtained at the interface with the Si substrate. These results were further confirmed by EDX analysis carried out on the same structures.

Finally, the following issues should be addressed in future work to achieve further improvements of our quantification method:

- In our model, we considered that the detector size is very small and far from the specimen so that all the X-rays emitted from the specimen are collected in a single point. In fact, a more rigorous description of the X-ray collection mechanism should include the actual geometry of the detector, leading to different collection angles and hence a modification of the total intensity of the collected X-rays.

- We showed that the calibration of the C-L factors based on the K lines is more accurate than the one based on L lines, because of the strong impact of the Bremsstrahlung radiation in the low energy region of the X-ray spectrum. Further efforts should therefore be devoted to the improvement of the Bremsstrahlung subtraction procedure in the low energy region of the spectrum.

- Finally, it would be useful to demonstrate the validity of our quantification method by using the zeta factor technique. For this, the microscope must be equipped by in-situ current measurement device [81].

Traduction Française

Chapitre 2

Développement d'une nouvelle méthode de quantification

Comme expliqué dans le chapitre précédent, les logiciels EDX commerciaux ne fournissent pas une approche rigoureuse pour traiter la correction d'absorption à l'aide de l'équation de Cliff et Lorimer. De plus, il est nécessaire, pour les mesures quantitatives, de disposer d'une estimation de l'erreur de mesure et de la densité minimale mesurable par la technique (limite de détection de la technique). Pour cela, une nouvelle méthode de quantification basée sur l'équation de Cliff-Lorimer a été développée. L'avantage de cette approche par rapport à d'autres méthodes (voir section 1.3.1) est qu'une mesure de courant in situ n'est pas nécessaire. Ce type de mesure nécessite la présence d'une cage de Faraday, et il ne s'agit pas d'un équipement standard dans les microscopes disponibles dans le commerce. En conséquence, la méthode que nous proposons peut être appliquée dans un microscope standard, sans aucun équipement spécial.

Dans ce chapitre, nous décrirons le problème de la correction d'absorption et justifierons le besoin d'une méthode itérative. Ensuite, nous détaillerons la procédure utilisée pour la calibration des facteurs C-L et pour l'estimation de l'erreur de la mesure finale.

2.1 Fractions massiques et calcul de la densité

Comme déjà discuté (voir la section 1.3.1 et l'équation 1.5), l'approche C-L est basée sur une relation de proportionnalité entre les intensités des pics et les fractions massiques des éléments. La constante de proportionnalité $K_{i,j:F_i,F_J}$ est le facteur de Cliff-Lorimer par rapport au i-ème et au j-ème élément. Elle dépend des familles de pics F_i et F_j qui ont été choisies pour chaque élément et, dans la grande majorité des logiciels commerciaux, est extraite d'une base de données de valeurs simulées. On peut montrer que les coefficients C-L peuvent également être écrits de la forme suivante :

$$K_{i,j:F_i,F_J} = \frac{k_{i:F_i,F_{i_0}}}{k_{j:F_j,F_{i_0}}} \tag{2.1}$$

où $k_{i:F_i,F_{i_0}}$est le coefficient C-L relatif à l'élément i et à un élément de référence commun i_0. Il convient de noter que, par définition, l'élément de référence a un coefficient C-L unitaire ($k_{i_0:F_{i_0},F_{i_0}} = 1$) et F_{i_0} indique la famille de pics choisie pour l'élément de référence. Avec cette convention, on peut montrer qu'il existe une formule directe reliant les intensités mesurées et les fractions de masse pour un matériau composé de N_A atomes différentes :

$$f_i^M = \frac{k_{i:F_i,F_{i_0}} I_{i:F_i}}{\sum_{j=1}^{N_A} k_{j:F_j,F_{i_0}} I_{j:F_j}} \tag{2.2}$$

La densité totale $I_{i:F_i}$ de la familleF_i pour un élément spécifique est obtenue en additionnant les intensités des raies de N_{F_i} ($K\alpha$, $K\beta$...) appartenant à la famille choisie pour l'élément i.

$$I_{i:F_i} = \sum_{k=1}^{N_{F_i}} I_{i:F_i,k} \tag{2.3}$$

Suivant cette notation, chaque pic caractéristique a une intensité $I_{i:F_i,k}$ et est associé à l'énergie$E_{i:F_i,k}$ où i identifie l'élément F_i de la famille des pics et k est l'indice identifiant la raie.

Il faut aussi noter que les intensités à utiliser dans la formule correspondent à l'intégrale des pics caractéristiques, à laquelle il faut ajouter l'intensité des rayons X qui sont décalés dans d'autres régions du spectre à cause des artefacts de mesure qui doivent être pris en compte pour l'application de cette formule. De plus, pour une interprétation correcte des résultats, les effets d'absorption dans l'échantillon doivent être pris en compte car ils sont négligés dans le modèle C-L. Enfin, il convient de noter que les coefficients de C-L sont normalement calculés à l'aide de modèles simplifiés et qu'ils doivent être étalonnés si on souhaite connaître la précision des résultats. Ils doivent donc être considérés comme des paramètres empiriques, qui sont aussi affectés par une erreur de mesure.

Même s'il est facile de calculer les fractions massiques à partir de mesures EDX, il peut être utile (c'est le cas dans la plupart de la littérature sur les dopants) d'utiliser des concentrations atomiques (en atomes/cm^3) au lieu des fractions massiques. La conversion des fractions massiques en concentrations atomiques c_i^A peut être obtenue à l'aide de la formule suivante :

$$c_i^A = \frac{\rho^M f_i^M}{m_i} N_{AV} \tag{2.4}$$

où ρ^M est la masse volumique de l'élément i, m_i sa masse atomique et $N_{AV} = 6,02214076 \cdot 10^{23} mol^{-1}$ est le nombre d'Avogadro.
La concentration des éléments dans un matériaux peuvent aussi être indiquées en utilisant les fractions atomiques. La formule chimique d'un alliage binaire composé par les

éléments A et B, par exemple, est normalement exprimée comme $A_{1-x}B_x$ où x est la fraction atomique de l'élément B dans l'alliage. La fraction atomique relative à une série d'éléments (f_i^A) peut être calculée à partir des fractions massiques correspondantes à l'aide de la formule suivante :

$$f_i^A = \frac{f_i^M/m_i}{\sum_{j=1}^{N_{AT}} f_j^M/m_j} \tag{2.5}$$

2.2 Correction de l'absorption

Pour quantifier un spectre EDX, il est nécessaire de mesurer les intensités des différents pics. Mais puisque les rayons X traversent l'échantillon avant d'atteindre le détecteur, l'intensité mesurée des rayons X I^* peut être différente de l'intensité émise I. Cet effet doit être pris en compte pour obtenir des résultats fiables. La formule suivante permet de calculer l'intensité mesurée $I^*(E)$ des rayons X de l'énergie E traversant un matériau homogène d'épaisseur z et de masse volumique ρ^M :([3] p.654) :

$$I^*(E) = I(E)\, e^{-\mu(E)\rho^M z} \tag{2.6}$$

où $\mu(E)$ est le coefficient d'absorption massique du matériau, *I (E)* est l'intensité initiale des rayons X et $I^*(E)$ est l'intensité mesurée par le détecteur après absorption dans l'échantillon.

Cette formule est obtenue dans l'hypothèse que l'émission des rayons X est uniforme en profondeur. Cela signifie que pour un échantillon d'épaisseur t, la densité d'émission est constante en profondeur et elle vaut $\frac{I(E)}{t}$. Tous les rayons X sont émis avec la même probabilité, mais la distance parcourue dans l'échantillon avant d'atteindre le détecteur dépend de la profondeur d'émission. En utilisant l'équation 2.6 on obtient :

$$I^*(E) = \int_0^t \frac{I(E)}{t} e^{-\mu(E)\rho^M z} dz = \frac{1 - e^{-\mu(E)\rho^M t}}{\mu \rho_M t} I(E) \tag{2.7}$$

On peut donc définir un coefficient de transmission liant l'intensité des rayons émis *I (E)* à la densité mesurée $I^*(E)$:

$$T(E, \{f_i^M\}) = \frac{1 - e^{-\mu(E)\rho^M t/\sin(\alpha)}}{\mu \rho_M t/\sin(\alpha)} \tag{2.8}$$

Le coefficient de transmission dépend de l'énergie des rayons X et des fractions de masse $\{f_i^M\}$ des différents éléments, car $\mu(E)$ et ρ^M dépendent de la composition de l'échantillon (pour cette raison, elles seront notées$\mu\left(E, \{f_i^M\}\right)$ et $\rho^M\left(\{f_i^M\}\right)$ dans la suite). α est l'angle d'élévation du détecteur (voir figure 2.1)

La formule liant la densité d'un matériau aux fractions de masse des atomes qui le composent n'est pas universelle, car la densité dépend évidemment de la structure

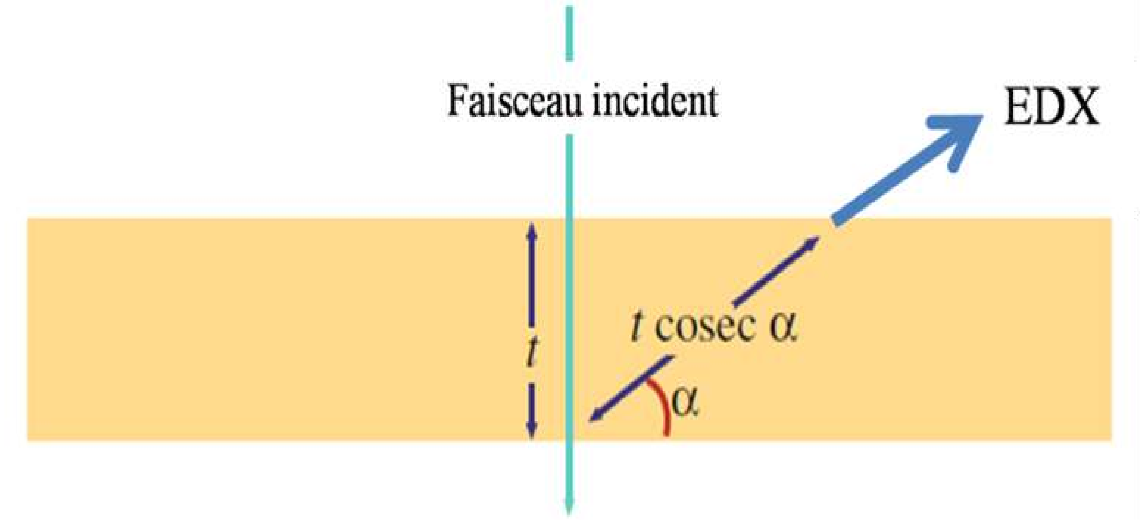

Figure 2.1: Illustration schématique de la géométrie d'absorption dans un matériau homogène.

du matériau. Par conséquent, l'expression analytique de$\rho^M\left(\left\{f_i^M\right\}\right)$ dépend du type d'échantillon.

D'autre part, il existe une formule universelle pour $\mu(E)$ ([3] p.654, [34]) :

$$\mu\left(E,\left\{f_i^M\right\}\right)=\sum_{i=1}^{N_{AT}}\mu_i\left(E\right)f_i^M \tag{2.9}$$

où $\mu_i(E)$ est le coefficient d'absorption massique associé à l'atome i.

Cette relation est normalement citée dans la littérature sans démonstration ou référence bibliographique. Il est donc difficile de déterminer sa limite de validité. Pour cette raison, il est nécessaire de donner une démonstration de cette formule et d'indiquer les approximations nécessaires à son obtention. En utilisant les sections efficaces totales d'interaction $\sigma_i(E)$ pour un rayon X d'énergie E avec un atome d'un élément i, nous pouvons écrire [35] :

$$\mu_i=\frac{\sigma_i}{m_i} \tag{2.10}$$

La formule 2.9 peut alors être obtenue en émettant l'hypothèse que la section efficace d'un mélange d'atomes est la somme des sections efficaces des atomes individuels. Cela signifie que les liaisons entre les atomes n'ont pas d'influence sur l'interaction des atomes avec les rayons X. C'est une bonne approximation, car elle est utilisée dans de nombreux autres calculs (énergies caractéristiques des rayons X et intensités relatives, par exemple). En supposant que les sections efficaces sont additives et que le nombre d'atomes i dans l'alliage est n_i, nous pouvons écrire :

$$\mu(E) = \frac{\sum_{i=1}^{N_{AT}} n_i \sigma_i}{\sum_{j=1}^{N_{AT}} n_j m_j} = \sum_{i=1}^{N_{AT}} \left(\frac{\sigma_i}{m_i} \frac{n_i m_i}{\sum_{j=1}^{N_{AT}} n_j m_j} \right) \tag{2.11}$$

Cette équation est équivalente à l'équation 2.9 puisque $\mu_i = \sigma_i / m_i$ et par définition$f_i^M = n_i m_i / \sum_{j=1}^{N_{AT}} n_j m_j$.

La valeur de $\mu_i(E)$ pour les différents éléments peut être obtenue en utilisant l'un des différents modèles disponibles (voir, par exemple, [36] et [37]). Dans notre cas, elles ont été calculées en utilisant la bibliothèque EPQ qui implémente le modèle proposé par Heinrich [37]. L'accès direct à la bibliothèque EPQ a été effectuée avec Octave en utilisant ses fonctionnalités d'interfaçage avec le code java.

Pour chaque pic caractéristique $E_{i:F_i,k}$, les intensités $I_{i:F_i,k}$ peuvent être calculées à partir des intensités mesurées $I^*_{i:F_i,k}$ en utilisant l'équation 2.8. Si l'échantillon est homogène et $\mu\left(E, \left\{f_i^M\right\}\right)$ et $\rho^M\left(\left\{f_i^M\right\}\right)$ sont connues, l'équation 2.8 et l'équation 2.9 peuvent être utilisées pour calculer les fractions massiques des éléments. C'est l'approche habituellement utilisée par les logiciels commerciaux. En supposant que l'échantillon est homogène, la valeur de la densité de l'échantillon est fournie par l'utilisateur et les coefficients d'absorption massique sont évalués en appliquant l'équation 2.9 aux fractions de masse calculées sans tenir compte des effets d'absorption. Les principales améliorations dans notre approche pour prendre en compte l'absorption des échantillons sont les suivantes :

- Tout d'abord, nous avons développé une approche itérative pour améliorer les algorithmes existants. Des informations supplémentaires sur l'algorithme utilisé sont données dans la section 2.2.

- De plus, nous avons pris en compte le fait que l'échantillon n'est pas homogène. Cette difficulté peut être résolue pour des échantillons de géométrie 1D, tels que ceux observés dans ma thèse, en choisissant soigneusement l'orientation du profil de concentration à l'intérieur du microscope. Si l'échantillon est orienté comme sur la figure 2.2 et que nous considérons que la taille du détecteur est négligeable, nous pouvons considérer que les rayons X passent par une coupe homogène pour atteindre le détecteur. Dans ce cas, l'équation 2.8 est valable pour chaque tranche, mais μ et ρ^M ne peuvent pas être considérés comme constants car leurs valeurs varient d'une tranche à l'autre, c'est à dire ils sont fonction de x (voir à nouveau la figure 2.2). Pour cette raison, à partir de maintenant, nous indiquerons explicitement la dépendance de la coordonnée x des différentes grandeurs ($f_i^M(x)$, $\mu\left(x, E, \left\{f_i^M(x)\right\}\right)$, $\rho^M\left(x, \left\{f_i^M(x)\right\}\right)$ ...).

Pour pouvoir prendre en compte l'absorption des échantillons, une approche itérative est nécessaire. Ceci est évident si nous considérons que pour calculer la fraction de masse $\left\{f_i^M(x)\right\}$ à chaque position x du profil, nous devons calculer le facteur de transmission

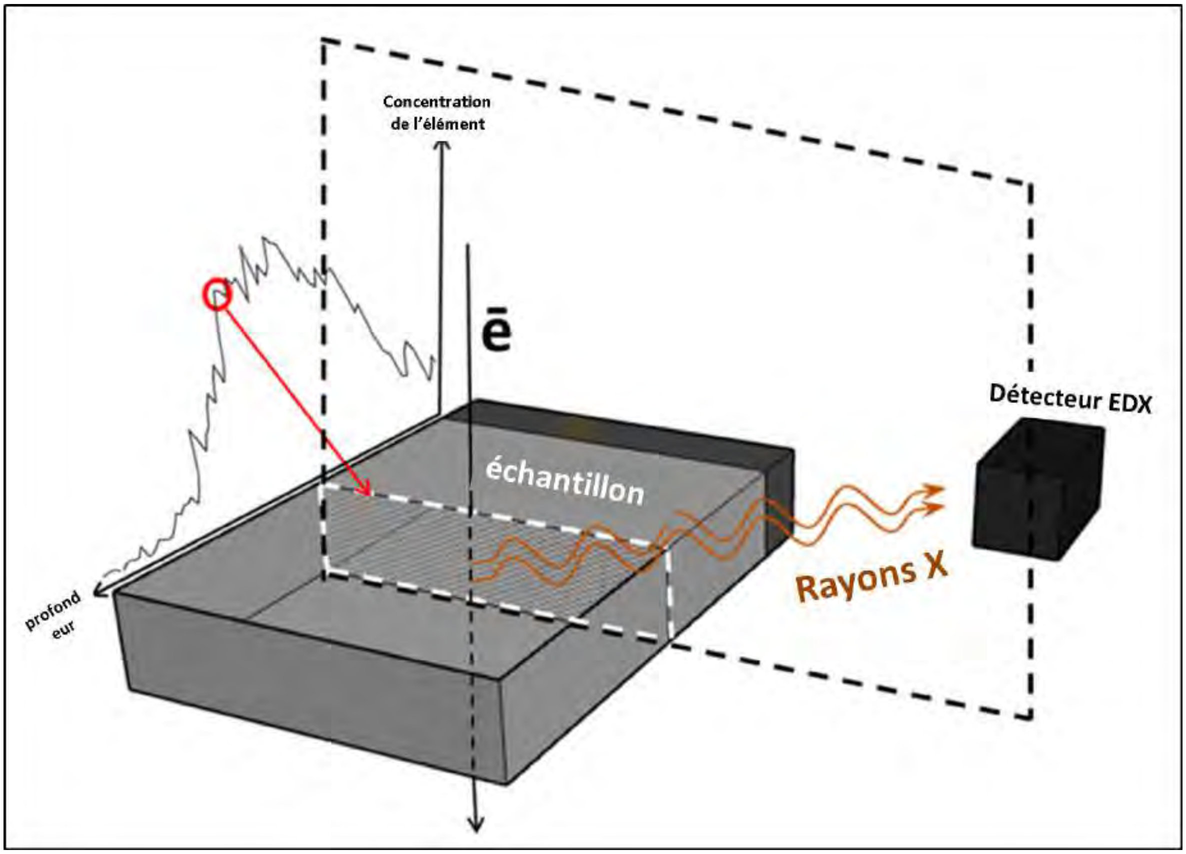

FIGURE 2.2: Illustration schématique de la position du détecteur et du trajet des rayons X, lorsque le détecteur est placé dans un plan perpendiculaire à la direction de variation du profil de dopage.

T qui dépend également de $\left\{f_i^M(x)\right\}$ (voir l'équation 2.8). Pour la procédure itérative, nous utilisons comme point de départ les fractions de masse $\left\{\left[f_i^M(x)\right]_0\right\}$ calculées en négligeant l'absorption (c'est-à-dire en supposant que $I^*_{i:F_i,k}(x) = I_{i:F_i,k}(x)$) pour tous les pics caractéristiques. A chaque itération, un nouvel ensemble de fractions massiques est obtenu en calculant le facteur de transmission à l'aide des fractions massiques obtenues lors de l'itération précédente :

$$\begin{aligned}
\left[T_{i:F_i,k}(x)\right]_n &= T\left(x, E_{i:F_i,k}, \left\{\left[f_i^M(x)\right]_n\right\}\right. \\
&= \frac{1 - e^{-\sum_{j=1}^{N_A} \mu_i\left(E_{j:F_j,k}\right)\left[f_j^M(x)\right]_{n-1} \rho^M\left(x, \left\{\left[f_i^M(x)\right]_{n-1}\right\} t/\sin(\alpha)\right.}}{\sum_{j=1}^{N_A} \mu_j\left(E_{j:F_j,k}\right) f_j^M \rho^M\left(x, \left\{\left[f_i^M(x)\right]_{n-1}\right\} t/\sin\left(\alpha\right)\right.}
\end{aligned} \tag{2.12}$$

Les nouvelles valeurs des intensités absorbées et des fractions de masse corrigées sont évaluées comme suit :

$$\left[I_{i:F_i,k}\right]_n = \frac{I^*_{i:F_i,k}}{\left[T_{i:F_i,k}(x)\right]_n} \tag{2.13}$$

puisque :

$$\left[I_{i:F_i}\right]_n = \sum_{k=1}^{N_{F_i}} \left[I_{i:F_i,k}\right]_n \tag{2.14}$$

on peut écrire :

$$\left[f_i^A\right]_n = k_i \sum_{k=1}^{N_F} \left[I_{i:F_i,k}\right]_n \tag{2.15}$$

Les valeurs finales$\widetilde{I}_{i:F_i,k}(x)$ et $\widetilde{f}_i^A(x)$ sont obtenues après N_I itérations, le critère d'arrêt étant que la variation relative des fractions de masse entre deux itérations ultérieures est inférieure à une tolérance relative fixée ($\frac{\left|\left(f_i^M\right)_n - \left(f_i^M\right)_{n-1}\right|}{\left(f_i^M\right)_n} < \epsilon$).

Comme indiqué plus haut, pour appliquer la procédure itérative, il est nécessaire d'établir, pour chaque matériau, la relation appropriée entre la masse volumique locale de l'échantillon $\rho^M(x)$ et les fractions massiques des éléments locaux $f_A^M(x)$ et $f_B^M(x)$. Ce calcul dépend de la structure de l'échantillon et varie selon les cas (voir section 2.3).

2.3 Calcul de la densité massique

Pour appliquer la procédure itérative, il est nécessaire, pour chaque matériau, d'établir la relation appropriée entre la densité de masse locale du spécimen $\rho^M(x)$ et les fractions de masse locales de silicium et d'arsenic $f_i^M(x)$.
Ce calcul est, dans les cas général, assez compliqué. Dans cette section, nous proposerons des approximations qui peuvent être utilisées dans des cas d'intérêt pour l'étude des semi-conducteurs :

- échantillons cristallins dopés
- alliages amorphes (échantillon cristallin après implantation ionique d'une impureté à haute dose)
- alliages pseudo-morphiques (comme par exemple l'alliage SiGe).

2.3.1 Matériaux cristallins dopés et approximation du «rayon équivalent».

Dans le cas idéal on peut considérer que dans un cristal dopé, des petites fractions d'atomes du substrat (marquées par 1) sont remplacées par des atomes dopants (marqué par 2). Cela revient à dire que tous les atomes dopants sont en substitution. Comme les atomes de dopage sont en faible concentration, la masse volumique peut être facilement calculée à partir de la masse volumique du substrat $\rho_1^M(x)$ en évaluant la différence de masse obtenue lorsque un atome de dopant remplace un atome de substrat.

$$\rho^M(x) = \rho_1^M \left[f_1^A(x) + \frac{m_2}{m_1} f_2^A(x) \right] = \rho_1^M \left[1 + \left(\frac{m_2}{m_1} - 1 \right) f_2^A(x) \right] \tag{2.16}$$

où $f_i^A(x)$ sont les fractions atomiques des deux éléments, liées, dans un alliage binaire, par l'équation suivante $f_1^A(x) = 1 - f_2^A(x)$.

Les fractions atomiques peuvent être calculées à partir des fractions massique en utilisant la formule 2.5 :

Dans le cas de deux éléments, cette formule se simplifie et on obtient :

$$\begin{aligned} f_1^A(x) &= 1 - f_2^A(x) \qquad (2.17) \\ f_2^A(x) &= \frac{f_2^M(x)}{f_2^M(x) + \frac{m_2}{m_1} f_1^M} = \frac{f_2^M(x)}{f_2^M(x) + \frac{m_2}{m_1}\left(1 - f_2^M(x)\right)} \end{aligned}$$

L'équation2.16 peut donc être ré-écrite :

$$\rho^M(x) = \rho_1^M \left[1 + \frac{(m_1 - m_2) f_2^M(x)}{m_1 - (m_1 - m_2) f_2^M(x)} \right] \tag{2.18}$$

C'est la formule recherchée car elle relie la masse volumique aux fractions massiques. Puisque dans cette approximation, on suppose que l'atome dopant ne provoque aucune déformation, nous l'appellerons «approximation du rayon équivalent» car elle est équivalente à considérer que les atomes du dopage et les atomes du substrat ont exactement le même rayon.

2.3.2 Approximation des solides amorphes

Une meilleure approximation peut être obtenue en utilisant une formule qui a été originalement dérivée pour les solides qui ne présentent aucun type d'ordre (également connu sous le nom de solides amorphes idéaux ou Ideal Amorphous Solids (IAS))[38] :

$$\rho^M = \sum_{i=1}^{N_{AT}} \rho_i^M f_i^V \tag{2.19}$$

où ρ_i^M est la densité de masse du solide amorphe et f_i^V est la fraction volumique de l' élément i dans l'alliage. L'hypothèse principale à la base de cette formule est que l'espace occupé dans le solide par un atome d'un élément spécifique est toujours le même, indépendamment de la concentration de l'alliage. Une autre façon de formuler la même approximation consiste à affirmer que la structure autour d'un type d'atome spécifique dans l'alliage est toujours la même et qu'elle ne dépend donc pas de la concentration. Cette approximation est évidemment correcte pour les IAS car dans ce cas, la distribution atomique est totalement aléatoire et ne dépend pas de la concentration des deux éléments dans l'alliage. L'espace autour d'un atome individuel dépend simplement de la «taille» de l'atome qui peut être estimée à l'aide de son rayon covalent.

L'équation 2.19 peut également être utilisée pour des solides qui ne possèdent pas une structure IAS à condition que les approximations susmentionnées soient respectées. Il n'est pas toujours facile de vérifier la validité des approximations. Un exemple d'application à un solide amorphe non idéal sera donné dans la section 3.1.3.

Pour établir une relation entre la masse volumique de l'alliage et les fractions massiques, on peut utiliser la formule suivante qui lie les fractions volumiques et les fractions massiques (cette formule peut être obtenue en utilisant les mêmes hypothèses de l'équation 2.19) :

$$f_i^V = \frac{\frac{f_i^M}{\rho_i^M}}{\sum_{j=1}^{N_{AT}} \frac{f_j^M}{\rho_j^M}} \tag{2.20}$$

En insérant l'équation 2.20 dans l'équation 2.19 et en considérant que les fractions massiques sont normalisées à 1 ($\sum_{j=1}^{N_{AT}} f_j^M{=}1$) on obtient l'expression de la densité de masse d'un solide amorphe idéal :

$$\rho^M = \frac{1}{\sum_{j=1}^{N_{AT}} \frac{f_j^M}{\rho_j^M}} \tag{2.21}$$

2.3.3 Alliages Pseudo-morphiques

Le calcul de la densité pour les alliages pseudo- morphes constitue également un cas d'intérêt. Les alliages pseudomorphiques sont des alliages binaires composés de deux éléments A et B (Si et Ge par exemple) qui ont exactement la même structure cristalline dans leur forme pure (le Si et le Ge purs ont une structure cubique de type diamant). Si on associe l'indice 1 à l'élément A, l'indice 2 à l'élément B et on indique avec x la fraction atomique f_2^A de B on peut écrire la formule chimique de l'alliage dans la forme $A_{1-x}B_x$. Dans un alliage pseudo-morphique, les deux réseaux ont des paramètres de maille très proches (la différence de paramètre de maille entre Si et Ge est de 0,227 Angström) et l'alliage binaire conserve la même structure des éléments purs (le SiGe a une structure de type diamant). Le paramètre de maille de l'alliage suit la loi de Vegard [39] :

$$a_{A_{1-x}B_x} = a_1(1-x) + a_2 x \tag{2.22}$$

où les coefficients a_i sont les paramètres de réseau des cristaux formés par un élément pur.

En utilisant la loi de Vegard, la masse volumique d'un alliage $A_{1-x}B_x$ peut être calculée en considérant que dans une maille élémentaire , il y a n atomes, dont *n (1-x)* de type A et nx de type B :

$$\rho^M = n\frac{m_1(1-x)+m_2x}{[a_1(1-x)+a_2x]^3} \tag{2.23}$$

L'expression finale peut ensuite être obtenue en transformant les fractions atomiques x et $(1-x)$ en fraction massiques. Nous ne déduirons pas cette formule car il peut être démontré que, dans ce cas, «l'approximation du solide amorphe» peut être utilisée. Cela semble paradoxal puisque dans ce cas l'alliage n'est pas du tout amorphe. Mais en réalité, il est facile de comprendre que, dans ce cas, on peut supposer que le volume occupé par un atome A ou B dans l'alliage $A_{1-x}B_x$ ne dépend pas de x. Cela dérive du fait que dans le cristal pur, un atome de type A occupe un volume $V_1^A = \frac{a_1^3}{n}$ (volume atomique) où n est, encore une fois, le nombre d'atomes par cellule unitaire. De la même manière, $V_2^A = \frac{a_2^3}{n}$, puisque les deux atomes ont exactement la même structure cristalline et que le nombre d'atomes par unité de cellule n est le même dans les deux expressions. Étant donné que l'écart entre a_1 et a_2 est négligeable, on peut considérer que les valeurs deV_1^A et V_2^A sont pratiquement identiques. La variation du volume atomique avec la composition de l'alliage est donc négligeable car dans le cas de l'alliage le volume atomique est compris entre V_1^A et V_2^A qui représentent le deux cas extrêmes. Par conséquent, on peut supposer que les volumes atomiques des deux atomes ne varient pas avec x et que l'approximation du solide amorphe peut être appliquée.

Ceci peut être démontré de manière rigoureuse en comparant le résultat exact (équation 2.23) avec le résultat obtenu avec «l'approximation du solide amorphe». Dans ce cas, le volume occupé par $n(1-x)$ atomes de type A est $V_1 = n(1-x)V_1^A$, le volume occupé par nx atomes de type B est $V_2 = nxV_2^A$ et le volume total est $V = V_1 + V_2$. La densité dans cette approximation est donnée par l'équation 2.19.

Tenant compte du fait que nous avons $f_i^V = V_i/V$, et que pour un solide cristallin avec n atomes par cellule élémentaire $\rho_i^M = \frac{nm_i}{a_i^3}$, nous pouvons écrire :

$$\begin{aligned}\rho^M =& \frac{\rho_1^M n(1-x)V_1^A + \rho_2^M nxV_2^A}{n(1-x)V_1^A + nxV_2^A} \\ =& \frac{\frac{nm_1}{a_1^3}n(1-x)\frac{a_1^3}{n} + \frac{nm_2}{a_2^3}nx\frac{a_2^3}{n}}{n(1-x)\frac{a_1^3}{n} + nx\frac{a_2^3}{n}} \\ =& n\frac{m_1(1-x)+m_2x}{a_1^3 + x(a_2^3 - a_1^3)}\end{aligned} \tag{2.24}$$

Les expressions 2.23 et 2.24sont évidemment différentes, mais on peut montrer que les dénominateurs sont égaux pour un alliage pseudo-morphique. Pour cela, on peut exprimer les deux dénominateurs en utilisant le paramètre $\varepsilon = \frac{a_2-a_1}{a_2}$ qui peut être considéré comme petit ($\epsilon = 4.2\%$ en SiGe). Pour le dénominateur de l'équation 2.23, nous pouvons écrire :

$$\begin{aligned} \left[a_1(1-x)+a_2x\right]^3 &= \\ &= a_1^3\left[1+\epsilon x\right]^3 \\ &= a_1^3\left[1+3\epsilon x+3\left(\epsilon x\right)^2+\left(\epsilon x\right)^3\right] \\ &= a_1^3\left[1+3\epsilon x+O\left(\epsilon^2\right)\right] \end{aligned} \tag{2.25}$$

alors que pour le dénominateur de l'équation 2.24, on peut montrer que :

$$\begin{aligned} a_1^3+x(a_2^3-a_1^3) &= \\ &= a_1^3+x\left[a_1^3(1+\varepsilon)^3-a_1^3\right] \\ &= a_1^3\left[1+3\varepsilon x+3\varepsilon^2x+\varepsilon^3x\right] \\ &= a_1^3\left[1+3\varepsilon x+O\left(\epsilon^2\right)\right] \end{aligned} \tag{2.26}$$

On peut noter que les deux expressions sont égales jusqu'au premier ordre en ϵ et que «l'approximation du solide amorphe» est en effet une bonne approximation pour les alliages pseudo-morphiques. L'équation 2.21 peut donc être utilisée pour calculer la densité massique à partir des fractions massiques.

2.4 Calibration du modèle et estimation d'erreur

Comme indiqué précédemment, pour pouvoir obtenir une mesure fiable, les coefficients C-L doivent être calibrés. De plus, pour obtenir une mesure quantitative, il faut estimer l'erreur sur ces coefficients et calculer l'erreur sur la mesure de la composition finale en combinant toutes les sources d'erreur possibles. La procédure et les formules que nous avons utilisées pour la calibration et l'estimation des erreurs seront abordées dans cette section. Une application directe de ces techniques utilisant la Spectroscopie de rétrodiffusion de Rutherford "RBS" [32] pour la calibration sera discutée dans le chapitre 3.

Dans le cas général d'un alliage composé de N_{AT} atomes, tous les coefficients $k_{i:F_i,F_{i_0}}$ C-L relatifs à l'élément de référencei_0 doivent être étalonnés.

Nous nous concentrerons, dans la suite, sur la technique générale pour la calibration et l'estimation de l'erreur expérimentale sur le coefficient C-L relatif à deux éléments i et i_0 appartenant aux familles F_i et F_{i_0}. Cette procédure peut être appliquée à différents couples de pics de l'ensemble jusqu'à ce que la totalité des coefficients C-L soient obtenus. Plusieurs échantillons peuvent être utilisés pour l'étalonnage à condition de disposer, pour chaque échantillon d'une mesure $\left[f_i^M(x)\right]_{Meas}$ des fractions de masse obtenue avec une autre technique expérimentale.

Pour deux éléments i et i_0, les facteurs C-L relatifs aux familles des pics F_i peuvent être déterminés par régression linéaire à partir de la formule suivante (voir l'équation 1.5 et 2.1) :

$$k_{i:F_i,F_j} \frac{\widetilde{I}_{i:F_i}(x)}{\widetilde{I}_{i0:F_{i_0}}(x)} = \frac{\left[f_i^M(x)\right]_{Meas}}{\left[f_{i0}^M(x)\right]_{Meas}} \tag{2.27}$$

Pour estimer l'erreur $\Delta k_{As:F_{As}}$ sur la valeur calibrée de $k_{As:F_{As},F_{Si}}$, nous avons supposé que la distribution statistique des intensités mesurées obéissait à la loi de Poisson. Dans ce cas, l'erreur sur la mesure de l'intensité I est donnée par $\Delta I(x) = \sqrt{I(x)}$et l'erreur relative s'écrit $\epsilon_I = \frac{\Delta I}{I} = \frac{1}{\sqrt{I}}$. La valeur de $k_{i:F_i,F_j}$ peut être obtenue en utilisant les techniques des moindres carrés pondérées et en minimisant l'expression ([41] p.75) :

$$R = \sum_k \frac{1}{w(x_k)} \left[\frac{\left[f_i^M(x)\right]_{Meas}}{\left[f_{i0}^M(x)\right]_{Meas}} - k_{i:F_i,F_{i0}} \frac{\widetilde{I}_{i:F_i}(x_k)}{\widetilde{I}_{i0:F_{i_0}}(x_k)} \right]^2 \tag{2.28}$$

où $\{x_k\}$ est l'ensemble des positions où les densités ont été mesurées expérimentalement. Afin de privilégier les points les plus précis, on a choisi comme facteur de pondération $w(x_i)$ l'erreur relative associée $\frac{\widetilde{I}_{As:F_{As}}(x_i)}{\widetilde{I}_{Si:F_{Si}}(x_i)}$.

En utilisant les lois de propagation des erreurs, nous pouvons alors écrire $w(x_k) = \sum_{i=1}^{N_{AT}} \frac{1}{\sqrt{\widetilde{I}_{i:F_l}(x_i)}}$.

La valeur de $k_{As:F_{As}}$et l'erreur statistique associée $\Delta k_{As:F_{As}}$ ont été calculées à l'aide de la formule standard pour l'estimation de l'erreur dans un régression pondérée aux moindres carrés ([41],[42]).

Lorsque vous effectuez une mesure quantitative, il est bien sûr important de pouvoir évaluer l'erreur de mesure totale. Dans le cas d'une mesure de concentration effectuée par EDX en utilisant la valeur calibrée des coefficients C-L, trois types d'erreur doivent être pris en compte :

1. L'erreur statistique sur les intensités mesurées $\Delta I(x) = \sqrt{I(x)}$. La contribution de cette erreur à la fraction de masse peut être calculée, à l'aide des techniques de propagation de l'erreur [42] :

$$\begin{aligned} \Delta_I f_i^M(x) \quad = \quad & \frac{k_{i:F_i,F_{i0}}}{\left[\sum_{j=1}^{N_{AT}} k_{j:F_j,F_{i0}} I_{j:F_j}(x)\right]^2} \times \\ & \sum_{j \neq i} \left[k_{j:F_j,F_{i0}} \left(I_{j:F_j}(x) \Delta I_{i:F_i} + I_{i:F_i}(x) \Delta I_{j:F_j}(x)\right)\right] \end{aligned} \tag{2.29}$$

où $\sum_{i \neq j}$ indique la somme sur tous les atomes sauf l'atome i.

2. Les erreurs $\Delta k_{j:F_j,F_{i0}}$ sur la valeur calibrée de la constante C-L. La contribution de cette erreur peut être calculée de la manière suivante :

$$\begin{aligned} \Delta_k f_i^M &= \frac{I_{i:F_i,F_{i0}}}{\left[\sum_{j=1}^{N_{AT}} k_{j:F_j,F_{i0}} I_{j:F_j}(x)\right]^2} \times \\ &\sum_{j \neq i} \left[I_{j:F_j}(x) \left(k_{j:F_j,F_{i0}} \Delta k_{i:F_i,F_{i0}} + k_{i:F_i,F_{i0}} \Delta k_{j:F_j,F_{i0}} \right) \right] \end{aligned} \tag{2.30}$$

3. L'erreur expérimentale sur l'épaisseur de l'échantillon Δt. Dans ce cas, il n'est pas possible d'appliquer la formule de propagation d'erreur pour évaluer l'erreur car la dépendance de $f_j^M(x)$ sur t est liée au calcul itératif présenté précédemment. Dans ce cas, la contribution à l'erreur totale a été estimée en utilisant la formule suivante $\Delta_t f_i^M(x) = \frac{\left|\left[f_i^M(x)\right]_{t+\Delta t} - \left[f_i^M(x)\right]_{t-\Delta t}\right|}{2}$ où $\left[f_i^M(x)\right]_t$ est la densité calculée pour une épaisseur t.

En supposant que l'erreur sur $k_{j:F_j,F_{i0}}$ et l'erreur sur les intensités sont statistiquement interdépendants, (le même détecteur est utilisé pour l'étalonnage et les mesures) et que l'erreur sur l'épaisseur est statistiquement indépendante des autres erreurs, on peut obtenir l'expression de l'erreur totale :

$$\Delta f_i^M(x) = \sqrt{\left[\Delta_I f_i^M(x) + \Delta_k f_i^M(x)\right]^2 + \left[\Delta_t f_i^M(x)\right]^2} \tag{2.31}$$

Comme on l'a déjà noté, même si les fractions de masse sont plus faciles à calculer à partir de mesures EDX, il est parfois préférable d'utiliser la concentration atomique. Pour évaluer l'erreur sur les concentrations atomiques $c_i^A(x)$, l'équation 2.4 peut être utilisée. Le résultat obtenu est :

$$\Delta c_i^A(x) = \frac{N_{AV}}{m_i} \left(\sum_{j=1}^{N_{AT}} \left| \frac{\partial \left(\Delta \rho^M\right)}{\partial f_j^M} \right| \Delta f_j^M + \rho^M \Delta f_i^M \right) \tag{2.32}$$

La formule précise dépend de la formule utilisée pour ρ^M (voir section 2.3).
Pour **l'approximation du rayon constant**, la formule suivante est obtenue pour l'erreur sur la concentration atomique du dopant :

$$\begin{aligned} \Delta c_2^A(x) =& \frac{N_{AV}}{m_j} \rho_1^M \left[1 + \frac{(m_1 - m_2) f_2^M(x)}{m_1 - (m_1 - m_2) f_2^M(x)} \right] \times \\ & \times \left\{ 1 + \frac{m_2(m_2 - m_1)}{\left[m_2 - (m_2 - m_1) f_2^M(x)\right]^2} f_2^M(x) \right\} \Delta f_2^M(x) \end{aligned} \tag{2.33}$$

Alors que pour **l'approximation du solide amorphe**, la formule suivante est obtenue :

$$\Delta c_i^A(x) = \frac{N_{AV}}{m_{As}} \frac{1}{\sum_{k=1}^{N_{AT}} \frac{f_k^M}{\rho_k^M}} \left\{ \Delta f_i^M(x) + \frac{1}{\sum_{k=1}^{N_{AT}} \frac{f_k^M}{\rho_k^M}} \sum_{j=1}^{N_{AT}} \frac{\Delta f_j^M(x)}{\rho_j^M} \right\} \tag{2.34}$$

Comme indiqué précédemment pour les alliages binaires on utilise souvent les fractions atomiques au lieu des fractions massiques. Dans ce cas, l'erreur sur les fractions massiques peut être calculée en appliquant la formule de propagation d'erreur sur l'équation 2.5. L'expression obtenue pour l'erreur sur les fractions atomiques est :

$$\begin{aligned} \Delta f_i^A = & \frac{1/m_i}{\left[\sum_{j=1}^{N_{AT}} f_j^M/m_j\right]^2} \times \\ & \sum_{j \neq i} \left[1/m_j \left(f_j^M \Delta f_i^M + f_i^M \Delta f_j^M\right)\right] \end{aligned} \tag{2.35}$$

Chapitre 3

Cartographie EDX quantitative dans les semi-conducteurs

Comme discuté dans l'introduction, la cartographie élémentaire à l'échelle nanométrique est un problème particulièrement critique pour les dispositifs à semi-conducteurs. L'émergence de dispositifs basés sur des jonctions ultra-minces ou des géométries 3D a créé une demande de nouvelles techniques, car les techniques standards telles que la spectroscopie de masse à ions secondaires ne peuvent pas être utilisées sur des dispositifs de nouvelle génération.
Le modèle de quantification décrit dans le chapitre précédent a été spécifiquement mis au point pour obtenir des mesures de concentration quantitatives par STEM / EDX. Comme indiqué précédemment, l'approche proposée est nécessaire pour résoudre les problèmes posés par le faible rapport signal/bruit obtenu dans les nano-objets et pour estimer l'erreur de mesure. Cela signifie que le nouveau modèle peut être utilisé pour le profilage de composition dans des nanodispositifs à semi-conducteurs.

Dans ce chapitre, deux applications du modèle à des matériaux semi-conducteurs seront décrites :

- La mesure des impuretés de faible concentration dans une structure de nanodispositifs en Si.

- La mesure de la concentration en Ge dans une nanostructure de SiGe.

La discussion inclura, pour chaque application, la motivation, et une description détaillée de l'application du modèle, des échantillons et de la configuration expérimentale utilisée.

3.1 Cartographie du dopage dans les nanodispositifs Si

Il a été souligné dans l'introduction que le profilage des dopants dans les dispositifs à semi-conducteurs modernes est un problème clé. Les nouveaux transistors sont basés sur de nouveaux substrats (tels que le silicium sur isolant) et des architectures 3D (transistors 3D sur substrat, nano-fils ...). La taille caractéristique du dispositif est de l'ordre de quelques nanomètres et les techniques classiques telles que la spectroscopie de masse des ions secondaires ne peuvent pas être utilisées. En revanche de mesure de concentration peuvent être effectuées en utilisant le STEM/EDX grâce au modèle développé dans ce travail de thèse. Dans cette section on montrera comment des mesures STEM / EDX peuvent être utilisée pour mesurer la distribution de dopage dans les régions de drain source d'un dispositif FinFET.

Un dispositif FinFET [45]est un type spécifique de transistor 3D - fabriqué à l'aide de techniques de lithographie standard sur des substrats SOI (Silicon On Insulator). Le substrat SOI consiste en une couche mince de Si cristallin d'épaisseur uniforme située au dessus d'une couche d'oxyde. La couche supérieure peut être utilisée pour créer des "ailettes" horizontales, appelées FIN dans la littérature, à l'aide de techniques de lithographie standard (voir figure 3.1(a)). Un transistor MOSFET, appelé FinFET, peut ensuite être obtenu en utilisant les FIN. Il existe plusieurs types de FinFET. L'idée générale derrière toutes les géométries est d'obtenir un contrôle amélioré du transistor en améliorant la géométrie de la grille. Pour cela, on utilise normalement de petits FIN (quelques dizaines de nanomètres) et la grille présente une structure 3D composée de plusieurs parois. Un dessin schématique d'un FinFET avec une grille à trois parois est montré dans la figure 3.1(b).

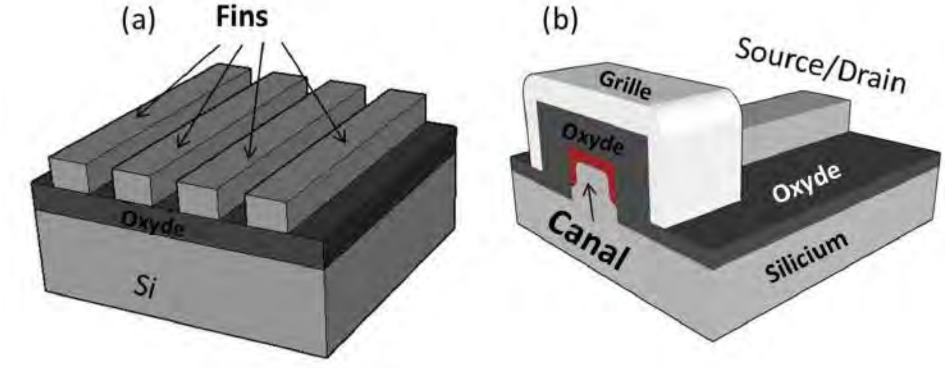

FIGURE 3.1: Illustrations schématique de FIN obtenus à partir de un substrat SOI (a) et d'un FinFet (b).

Lors de la création d'un FinFET, un des principaux problèmes est de répartir de manière symétrique le dopage sur toutes les parois utilisées. Cela signifie que (voir figure 3.1(b)) les trois parois latérales doivent avoir la même concentration de dopage que la paroi supérieure. Une distribution de dopage répondant à cette exigence est appelée distribution «conforme».

Il est facile de comprendre que pour qu'un transistor fonctionne correctement, le dopage source et drain doit également présenter une distribution conforme. Et comme le canal est faiblement dopée dans les dispositifs FinFET (et même intrinsèque dans certains cas) et que les régions source et drain doivent être fortement dopées pour assurer un contact ohmique, le fait d'obtenir une distribution conforme dans les régions source/drain est d'importance capitale. Pour cette raison, nous avons décidé d'appliquer le modèle développé à la mesure d'un dopage conforme d'arsenic à haute concentration dans une structure de test de type FinFET.

Dans la suite, les détails expérimentaux sur l'échantillon observé et les conditions d'observation seront décrits. Dans la section 3.3, la calibration du modèle sera discutée et on montrera que un profil As quantitatif peut être obtenu à l'échelle nanométrique. Enfin, les erreurs de mesure et la limite de détection de dopage seront estimées et la possibilité d'améliorer la limite de détection en modifiant les paramètres d'observation sera discutée.

3.1.1 Description des échantillons

Une structure de test de type FinFET avec un canal de 80 nm de largeur et 100 nm de hauteur ayant reçu une implantation à dose élevée (voir la figure 3.2 (b)) a été utilisée pour les mesures. La structure de test ne présentait aucun oxyde de grille ni contact métallique, car nous souhaitions que l'observation soit focalisée sur la distribution des dopants. Pour la création de la région dopée, un implantation plasma d'arsenic a été utilisé afin d'obtenir une distribution conforme du profil de dopage.

Pour pouvoir mesurer la concentration de dopage en arsenic dans le nanodispositif, nous avons conçu deux échantillon de calibration obtenus par implantation ionique dans un wafer de silicium monocristallin. Afin de pouvoir vérifier la précision de la calibration des cofficients de C-L pour différentes concentrations, deux types d'échantillons ont été utilisés. Les deux ont été implantés avec une tension d'accélération de 21KeV avec une dose différente s'élevant respectivement à $9,4\,10^{15}cm^{-2}$ et $1,8\,10^{15}cm^{-2}$. En raison de la dose élevée utilisée pour l'implantation, les plaquettes implantées sont métamorphisées en surface, après implantation (voir figure 3.3). Les paramètres d'implantation ont été choisis en simulant le profil d'implantation à l'aide du logiciel de simulation Monte Carlo SRIM (Stopping and Range of Ions in Matter) ([46] ch.3). Les résultats de la simulation correspondant aux deux doses différentes sont présentés dans3.2 (a). On peut noter que la valeur du pic de concentration s'élève à $10^{21}cm^{-3}$(équivalent à une concentration atomique de As de 10%) pour l'implant à plus forte dose et à $5\,10^{21}cm^{-3}$ (soit une concentration atomique de As de 2%) pour l'implant à plus faible dose.

Afin d'obtenir une mesure absolue de la concentration en arsenic, des mesures de spectroscopie par rétrodiffusion de Rutherford (RBS) ont été effectuées sur les échantillons de calibration. Pour les mesures RBS des ions He + accélérés à 1,5 MeV ont été

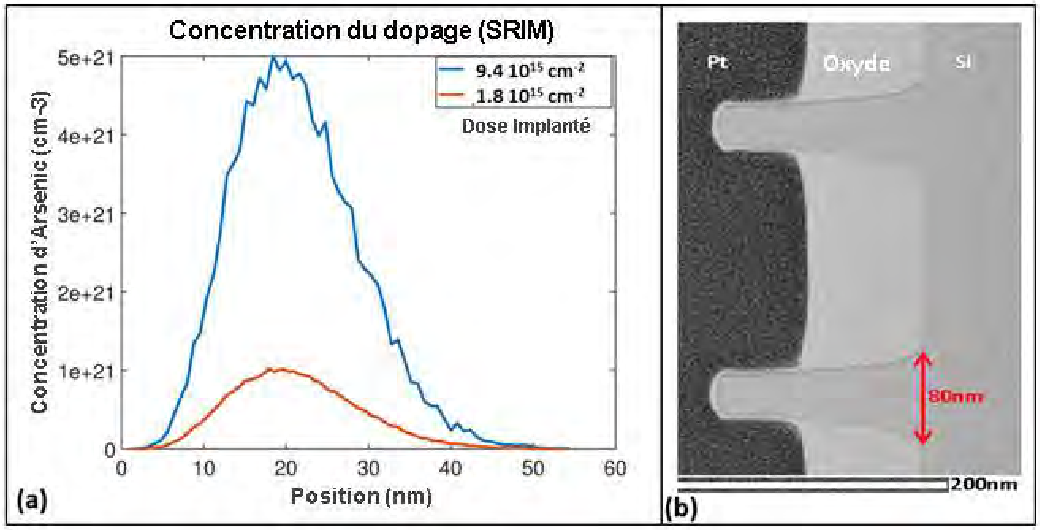

FIGURE 3.2: (a) Simulation de la distribution de dopage implanté obtenue avec SRIM pour une énergie de 21keV ; (b) Image MET de la section transversale de l'échantillon FinFET.

utilisés. La résolution du détecteur et l'angle solide ont été obtenus sur un échantillon de référence de SiO_2 en utilisant un angle de collection du détecteur de 10 °. Pour les mesures de concentration en As, un angle de collection de 60 ° a été utilisé. En utilisant le RBS, les profils de concentration atomique d'arsenic ont été obtenus dans les deux échantillons de calibration. Les résultats ont été utilisés pour calibrer les coefficients C-L, comme expliqué dans la section 2.4.

3.1.2 Préparation des échantillons et observations MET

Pour pouvoir être observé en MET, une lamelle de section transversale a été créée par des techniques de faisceau ionique focalisé (FIB) [47]. Pour cela un FIB à double colonne FEI Helios 600i a été utilisé pour obtenir une lamelle. Une procédure d'extraction de type "lift out" a été utilisée pour transférer la lame FIB sur une grille de support en cuivre (pour l'observation en MET). Pour pouvoir obtenir une lame d'épaisseur uniforme, une couche de platine a été déposée sur la surface de l'échantillon avant la création de la lamelle. Le dépôt de platine a été réalisé en deux étapes consécutives, la première par dépôt induit par faisceau électronique (EBID) et la deuxième par dépôt induit par faisceau ionique (IBID) afin d'éviter tout type de dommage ionique de la surface pendant le dépôt IBID. En plus de permettre l'obtention d'un échantillon d'épaisseur uniforme, l'utilisation du FIB permet de réduire, lors de la mesure, la contribution de rayons X secondaires générés par fluorescence et rétrodiffusion par rapport à des échantillons préparés par des techniques classiques comme l'amincissement mécanique suivi d'un amincissement ionique (voir la figure 3.4). La préparation FIB a

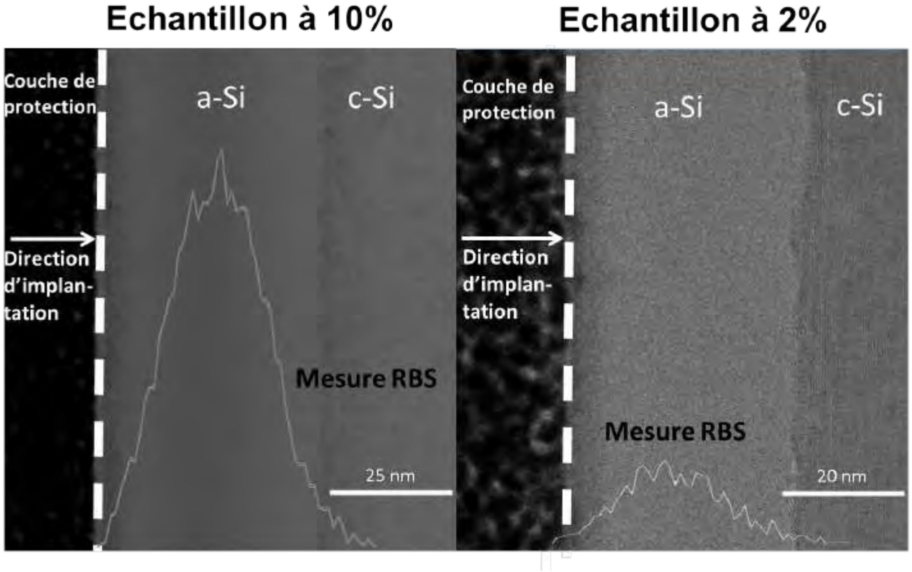

Figure 3.3: Mesure RBS de la densité atomique As superposée à l'image MET obtenue dans le même échantillon. La variation de contraste dans les images MET indique que la région implantée à haute concentration est amorphisée.

également été utilisée dans le cas des FinFET puisque dans ce cas, une région précise de l'échantillon doit être sélectionnée pour pouvoir observer les régions implantées.

Les mesures STEM / EDX ont été effectuées sur un microscope JEOL ARM équipé d'un canon à émission de champ à froid, d'un correcteur d'aberration sphérique pour la sonde et d'un détecteur CENTURIO-X avec un angle d'élévation de 24,3 degrés et un angle de detection de 0,98 stéradians.

Les profils de distribution ont été obtenus à partir de cartographies STEM / EDX puis en créant des spectres cumulatifs en intégrant le signal dans la direction latérale. Le programme JEOL Analysis Station a ensuite été utilisé afin de soustraire la Bremsstrahlung dans les spectres cumulés et de calculer les intensités intégrées des pics caractéristiques pour les différents éléments. Les intensités obtenues ont été utilisées comme point de départ pour la calibration, la correction d'absorption et le calcul de l'erreur.

3.2 Application de la méthode de quantification

La quantification des données a été effectuée à l'aide des méthodes décrites dans le chapitre précédent. Pour pouvoir appliquer la méthode de correction itérative une équation de densité massique a du être choisie pour les échantillons de test, composés de SiAs amorphe (a-SiAs) et pour le FinFET, composé de silicium cristallin implanté (c-SiAs, FinFET).

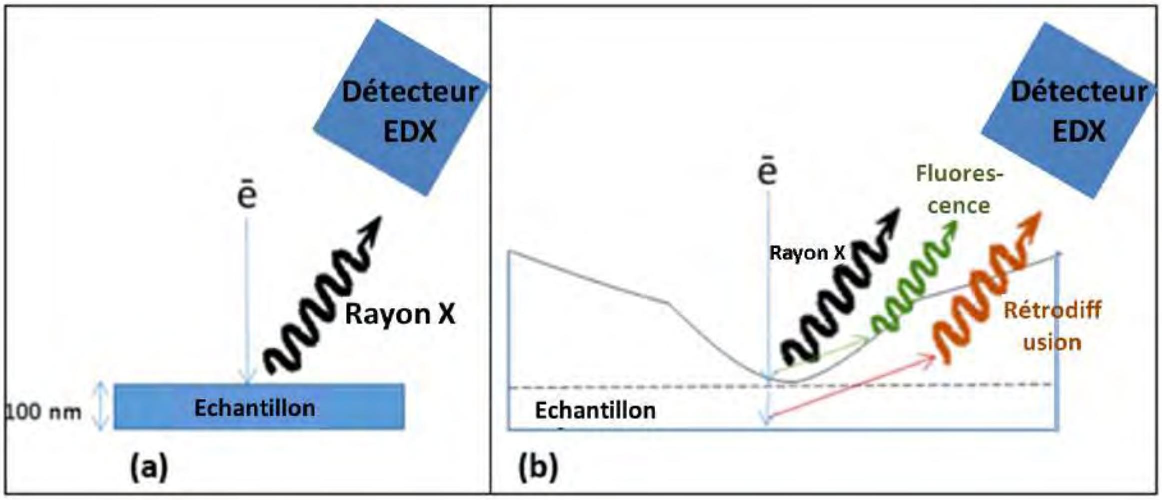

FIGURE 3.4: Illustration schématique de l'influence de la géométrie des échantillons sur les artefacts EDX (rayons X secondaires créés par la fluorescence et les électrons rétro-diffusés) dans les échantillons préparés : a) par FIB. b) par amincissement mécanique+ionique.

Pour les a-SiAs, les approximations du rayon constant et du solide amorphe doivent être considérés car le matériau est amorphe et les valeurs du rayon covalent du silicium et de l'arsenic sont proches $R_{Si} = (111 \pm 2)pm$ et $R_{As} = (119 \pm 4)pm$. L'approximation du rayon constant pourrait en principe être une bonne approximation. Le résultat obtenu en utilisant l'équation 2.16 et les valeurs de masses molaires indiquées en littérature ($m_{Si} = 28.0855\frac{g}{mol}$ et $m_{As} = 74.9216\frac{g}{mol}$) sont montrés en rouge en figure 3.5.

Mais dans la pratique, cette approximation surestime la densité de masse de SiAs amorphe (a-SiAs) pour des concentrations élevées en arsenic par rapport à la valeur de l'arsenic amorphe indiqué dans la littérature ($\rho^{M}_{a-As} = 4.7\frac{g}{cm^3}$ [48]) comme le montre la figure 3.5.

Il pourrait alors être tentant d'utiliser «l'approximation du solide amorphe» (l'équation 2.19) dans ce cas. Mais, comme déjà discuté dans la section 2.3.2, pour justifier ce choix, l'une de ces deux hypothèses doit être satisfaite :

- La structure de l'a-SiAs est compatible avec celle d'une structure IAS.
- La structure de l'alliage est similaire à celle des phases amorphes des éléments purs. Si c'est le cas, le même raisonnement appliqué dans la section 2.3.3 aux alliages pseudomorphes peut être appliqué dans le cas de a-SiAs.

Il est facile de prouver que ni le a-As ni le a-Si sont des solides amorphes idéaux. Pour le a-Si, cela peut être prouvé en notant que la densité prédite par le modèle IAS $\rho^{M}_{a-Si,IAS} = 4.32g/cm^3$[38] est supérieure à la densité du Si cristallin (c-Si) $\rho^{M}_{c-Si} =$

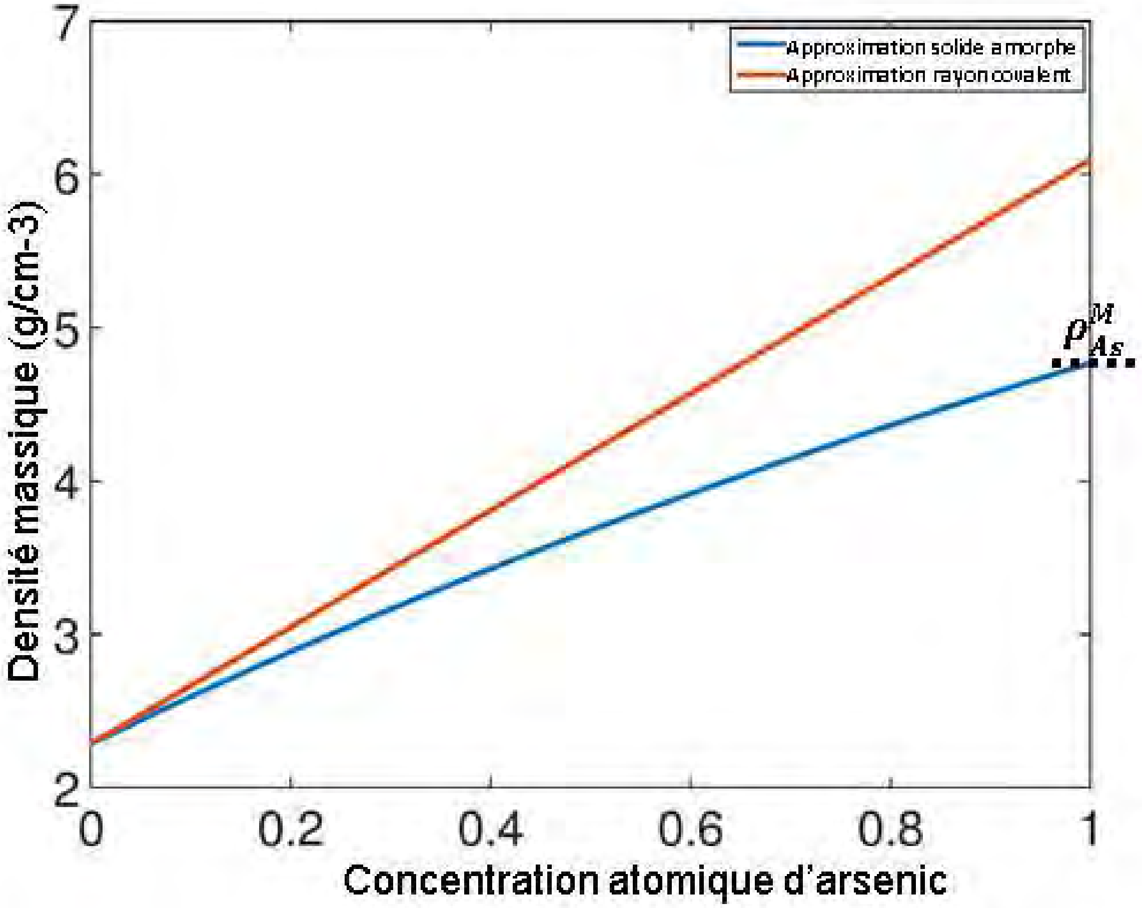

FIGURE 3.5: Densité de masse en fonction de la concentration obtenue avec les différents modelés. La valeur déterminée expérimentalement de la masse volumique ρ^M_{As} de l'arsenic amorphe [48] est aussi indiquée dans le graphique.

$2.32 g/cm^3$. Cette valeur de densité "théorique" ne correspond pas à la valeur la densité de silicium amorphe déterminée expérimentalement $\rho^M_{a-Si} = 2.285\, g/cm^3$[49] qui est légèrement inférieure à ρ^M_{c-Si}. Le même type de raisonnement peut être utilisé pour prouver que la structure de l'amorphe As ($\rho^M_{a-As} = 4.7\, g/cm^3$,$\rho^M_{c-As} = 5.73\, g/cm^3$) n'est pas non plus compatible avec celui d'un IAS. En conclusion, il n'y a aucune raison de penser que l'alliage a-SiAs (dont la structure est une combinaison de la structure de Si amorphe et de As amorphe) présente une structure IAS.

D'autre part, il est facile de montrer que a-Si et a-As ont une structure similaire. On peut alors supposer que cette structure est conservée dans l'alliage SiAs indépendamment de la concentration d'As dans l'alliage, ce qui est précisément l'hypothèse utilisée pour dériver l'équation 2.19. Pour montrer ceci, on peut se servir des fraction $s = \frac{V^S}{V^A}$ entre le volume atomique V^A et la taille de l'atome V^S. Ces fractions sont un bonne estimation du taux de remplissage du solide. Le volume V^A est par définition l'inverse de la densité atomique $\rho^A = \rho^M/m$ du matériau tandis que la taille de l'atome est calculée en utilisant une approximation sphérique ($V^S = \frac{4}{3}\pi r^3$) et le rayon covalent r. Les valeurs de $s = \frac{4}{3}\pi r^3 \rho^A$pour le Si amorphe et le As amorphe peuvent être calculées en utilisant les données précédemment définies pour la densité, le rayon et la masse des deux éléments. Les valeurs obtenues sont assez proches ($s_{Si} = 0.28$,$s_{As} = 0.26$) , ce qui confirme que la structure des deux matériaux purs est presque identique.

La comparaison entre l'approximation du solide amorphe et l'approximation de même rayon est illustrée à la figure 3.5. On peut noter que l'approximation du solide amorphe donne de meilleurs résultats pour des concentrations élevées en arsenic, alors que les deux approximations sont presque équivalentes pour des concentrations en As faibles, comme on peut le voir sur la figure 3.5.

Pour les c-SiAs, il est beaucoup plus simple d'obtenir la formule de la masse volumique puisque celle-ci correspond exactement au cas où l'approximation de rayon constant a été déduite. La densité de masse peut simplement être calculée en utilisant 2.16 avec $m_1 = m_{Si}, m_2 = m_{As}, \rho_1^M = \rho_{Si}^M$.

3.3 Résultats expérimentaux et discussion

Dans cette section, nous présenterons les résultats expérimentaux obtenus sur la structure de test FinFET. Pour cela, les résultats de la calibration des coefficients de C-L seront tout d'abord décrits. Ensuite, les résultats finaux obtenus sur le profilage des dopants seront discutés.

3.3.1 Résultats de Calibration

Afin d'appliquer les techniques de calibration, les concentrations de densité atomique $c_{A/RBS}^A(x)$ mesurées par RBS ont été converties en fractions masiques. Ensuite, les coefficients de C-L ont été obtenus par régression linéaire pondérée comme décrit dans la section 2.4. Les équations 2.4 et 2.21 peuvent être combinées pour obtenir les fractions de masse mesurées par RBS :

$$\left[f_{As}^M(x)\right]_{Meas} = \frac{m_{As} c_{As/RBS}^A(x)}{N_{AV}\rho_{a-Si}^M + m_{As} c_{As/RBS}^A(x)\left(1 - \frac{\rho_{a-Si}^M}{\rho_{a-As}^M}\right)}$$

La technique d'étalonnage décrite dans la section 2.4 a été appliquée aux échantillons de calibration a-SiAs décrits dans la section 3.1.1. Plusieurs spectres EDX (un pour chaque pixel de l'image STEM correspondante) ont été enregistrées (voir la figure 3.6 pour l'échantillon à 2% et la figure 3.7 pour l'échantillon à 10%). Pour l'acquisition, l'échantillon FIB a été orienté comme sur la figure2.2. Les traitements des spectres nous a permit d'obtenir les distribution d'intensité des pics de Si et As dans la zone observée. Ensuite, un profil d'intensité a été obtenu pour chaque pic en intégrant les distributions (voir fig. 3.6(a) et 3.7(a)) dans une direction perpendiculaire à la direction z (définie à la figure 2.2). Les distributions de composition ont été obtenues en appliquant notre modèle à différentes familles de pics caractéristiques : les pics K pour le silicium et les pics K ou L pour l'arsenic (voir figure3.8).

La procédure de correction d'absorption décrite dans la section 2.2 a ainsi été utilisée pour calculer les intensités corrigées par absorption $\widetilde{I}_{Si:K}$, $\widetilde{I}_{As:K}$ et $\widetilde{I}_{As:L}$. L'algorithme d'absorption itérative a montré une convergence rapide et aucune instabilité numérique (voir figure 3.9(a)). La convergence est généralement obtenue après deux itérations. Cela explique pourquoi toutes le courbes ne sont pas visibles : les profils pour les itérations de 2 à 10 sont en fait entièrement superposés.

On peut observer que les effets d'absorption sont plus prononcés dans la région de haute densité (voir figure 3.9(b)). Ceci peut être compris en remarquant que la masse volumique de l'échantillon est plus élevée dans cette région et, par conséquent, les effets d'absorption sont plus importants. Cela démontre clairement qu'il est important d'établir une formule de densité afin de prendre en compte la dépendance de la masse volumique à la concentration locale.

Ensuite, les techniques de régression linéaire ont été utilisées pour la calibration :

- du facteur de C-L $K_{As,Si:K,K} = k_{As:K,K}$ associé à la famille des pics K de l'arsenic lorsque la famille des pics K du silicium est utilisée comme référence.
- du facteur de C-L $K_{As,Si:L,K} = k_{As:L,K}$ associé à la famille des pics L de l'arsenic lorsque la famille des pics K du silicium est utilisée comme référence.

Afin de minimiser l'erreur sur les coefficients C-L, nous avons effectué la calibration sur l'échantillon ayant reçu la dose la plus élevée. La raison de ce choix peut être facilement comprise en observant que dans l'hypothèse que les intensités de rayons X aient une distribution de Poisson, l'erreur relative est minimisée pour les intensités les plus élevées. Cela implique une variance plus faible des valeurs d'intensité et une erreur plus faible sur les coefficients de C-L.

Les concentrations de dopage mesurées par EDX et RBS sont présentés en figure 3.10 avant et après la calibration des coefficients. Les valeurs obtenues sont les suivantes : $K_{As,Si:K,K} = 2.18 \pm 0.03$, $K_{As,Si:L,K} = 1.89 \pm 0.03$.

L'erreur sur les coefficients C-L peut être utilisée pour estimer les erreurs finales sur le profil de densité, comme expliqué à la section 2.4, où les sources d'erreur possibles ont été examinées. Entre les différentes erreurs, l'erreur résultant de l'incertitude sur l'épaisseur de l'éprouvette mérite une discussion particulière. Il est généralement compliqué de mesurer l'épaisseur des échantillons de manière fiable et précise. Même si certaines techniques existent (mesure par SEM, EELS, diffraction électronique en faisceau convergent etc...), il est généralement compliqué d'obtenir une valeur fiable avec une faible erreur. En conséquence, les erreurs de mesure sur l'épaisseur peuvent être de l'ordre de 30%

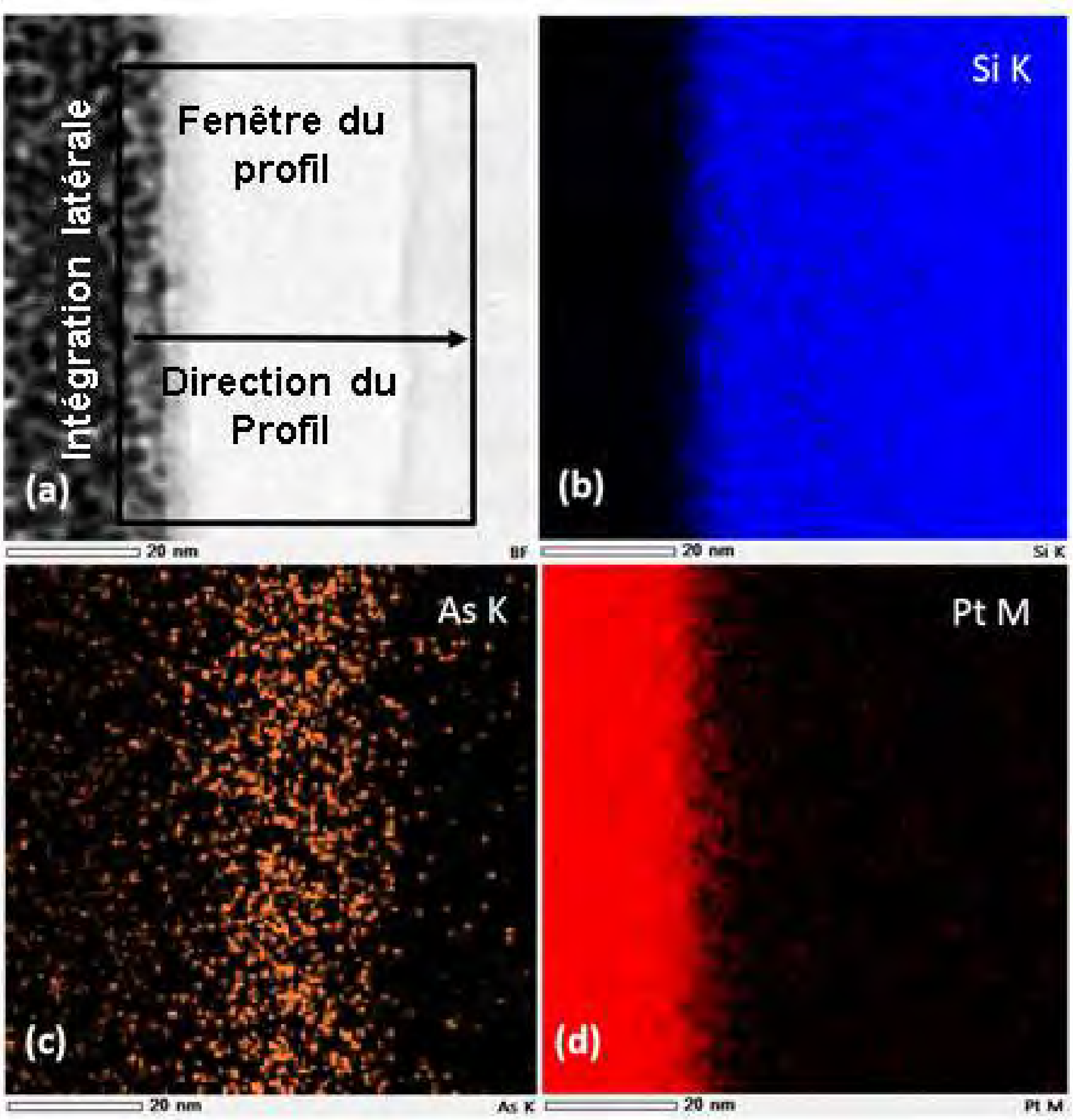

FIGURE 3.6: Distributions d'intensité obtenus dans l'échantillon de calibration avec **un pic de densité atomique de 2%** pour le pic SiK (b) pour AsK(c) et PtM(d). L'image STEM de la région cartographiée ainsi que la géométrie utilisée pour l'extraction du profil est indiquée en (a).

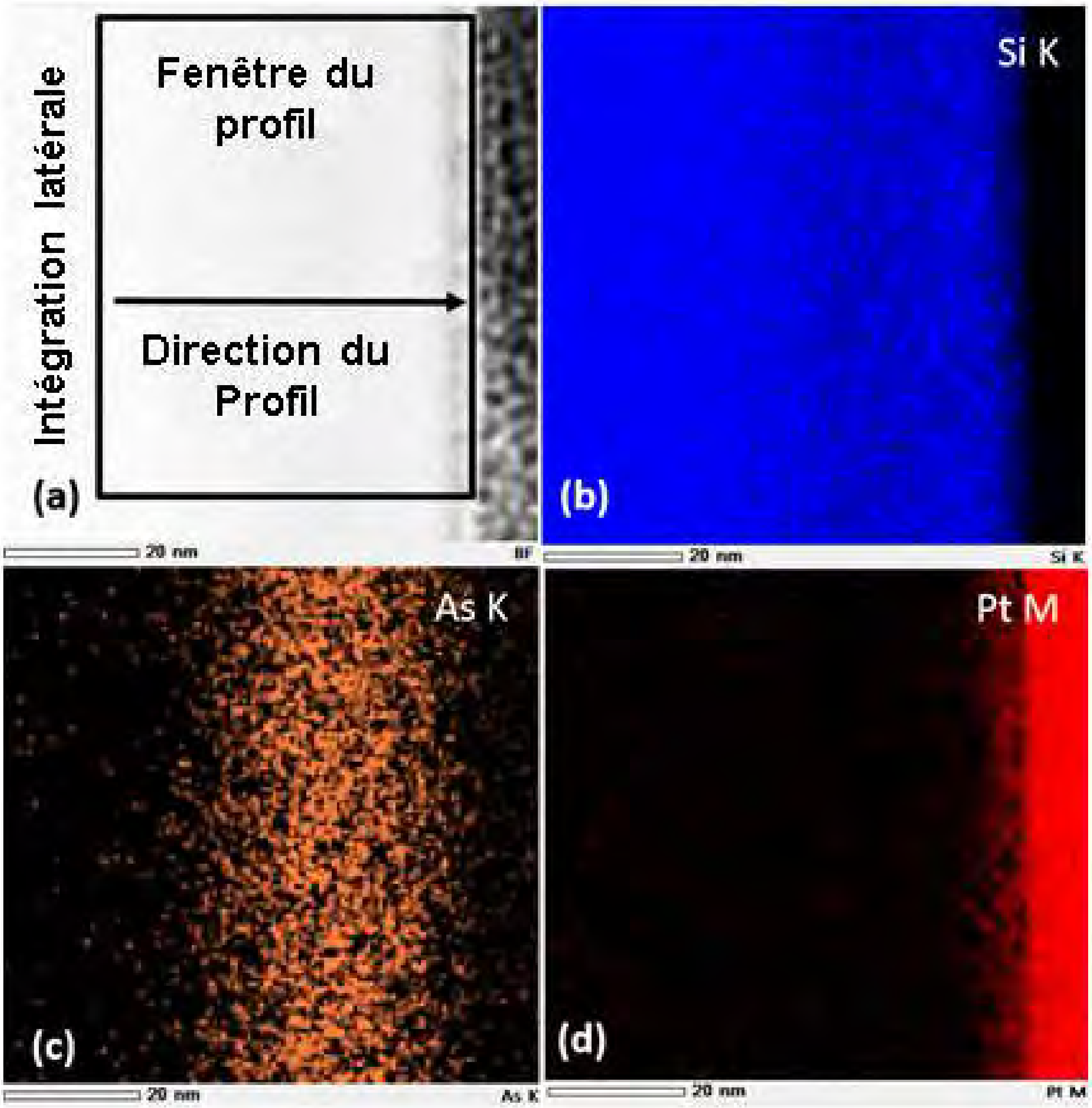

FIGURE 3.7: Distributions d'intensité obtenus dans l'échantillon de calibration avec **un pic de densité atomique de 10%** pour le pic SiK (b) pour AsK(c) et PtM(d). L'image STEM de la région cartographiée ainsi que la géométrie utilisée pour l'extraction du profil est indiquée en (a).

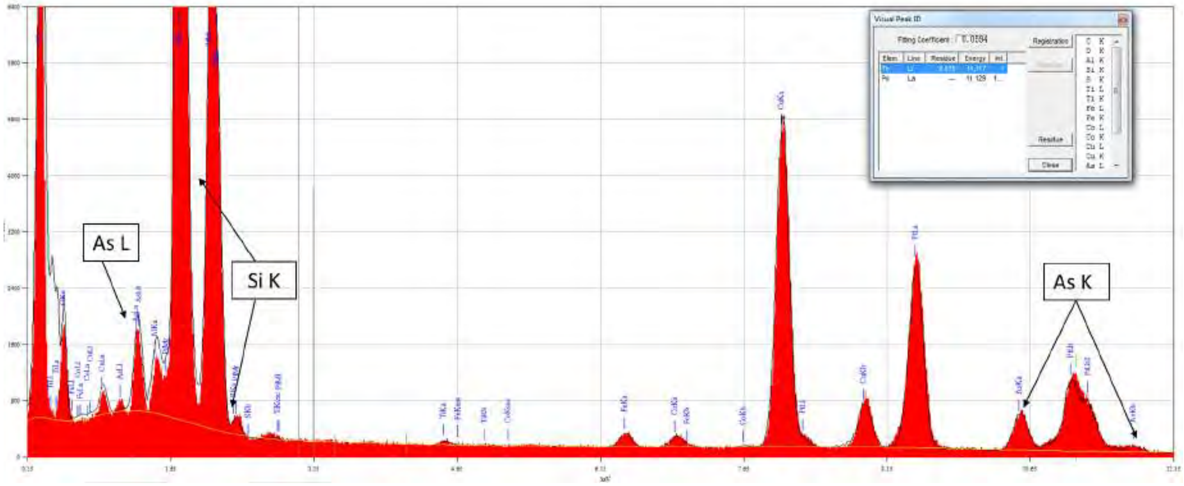

FIGURE 3.8: Spectre EDX obtenu dans l'échantillon de calibration 10% et montrant la position des familles des pics Si et As

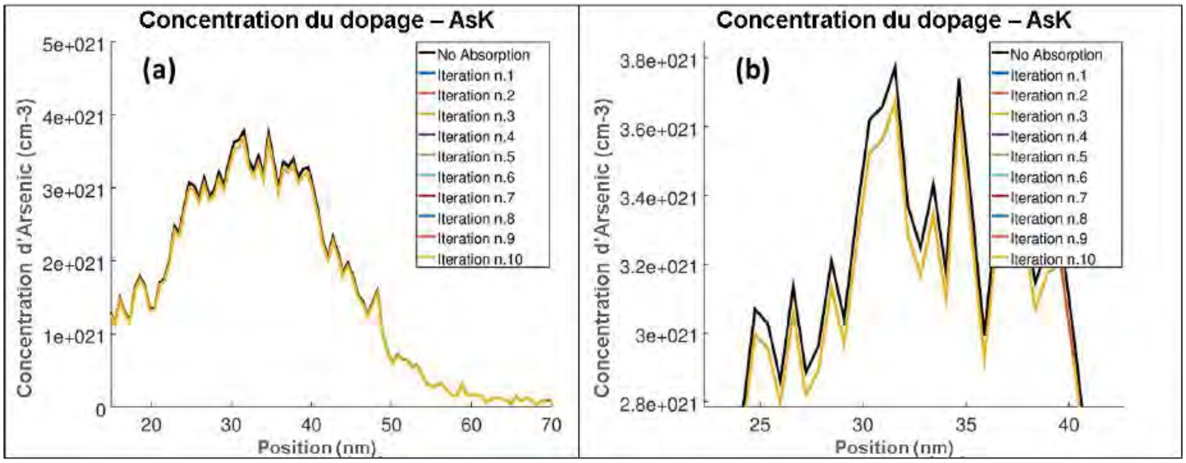

FIGURE 3.9: Résultat de la correction d'absorption pour les 10 premières itérations. Le profil complet est affiché en (a) et la région a haute densité en (b).

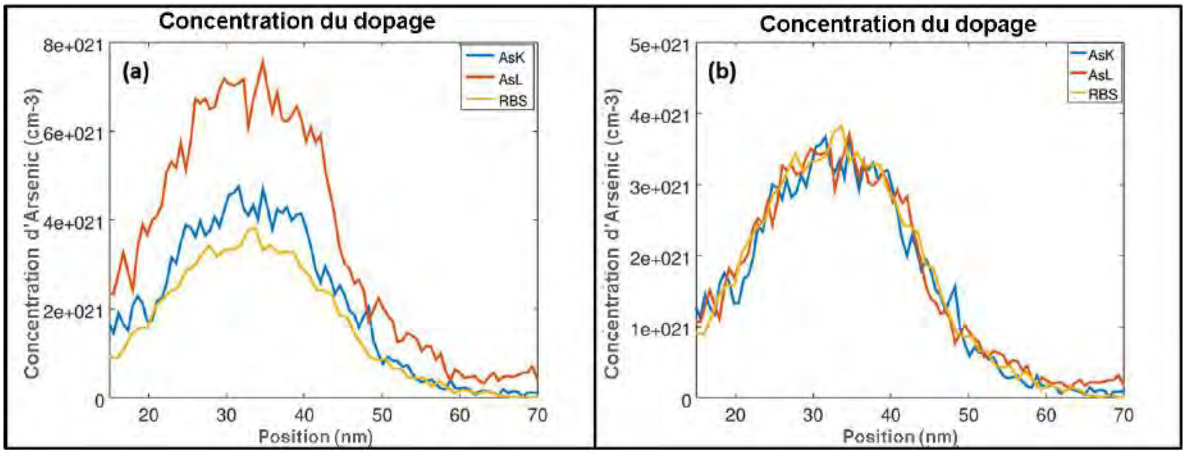

FIGURE 3.10: Profil de la concentration de dopage $\widetilde{c}^{A}_{As}(x)$ avant (a) et après (b), calibration pour les pics $I_{As:K}$(AsK) et $\widetilde{I}_{As:L}$. Les profils RBS sont aussi montrés sur la figure.

ou plus. Il est donc important d'évaluer l'influence de l'erreur d'épaisseur sur la mesure de la densité. Pour cela, la variation de la densité de As mesurée dans les régions à haute densité (qui, on l'a déjà noté, sont les plus affectés par l'absorption) est montrée sur la figure 3.11. On peut facilement constater que la variation de la concentration est faible même pour des variations d'épaisseur importantes. Cela signifie qu'une mesure précise de la concentration de dopage peut être obtenue même si l'erreur sur l'épaisseur de l'échantillon (Δt) est élevée. Ce résultat peut paraître surprenant car l'intensité du pic corrigé est fortement affectée par des variations d'épaisseur importantes. La composition mesurée, en revanche, est moins affectée, car elle dépend de l'intensité du pic de As et du pic de Si, qui subissent des variations comparables à cause des variations d'épaisseur. Ceci peut être résumé en disant que la variation d'épaisseur a une forte influence sur la valeur des pics mais une faible influence faible sur les différences entre les pics. Les profils obtenus ainsi que les erreurs expérimentales totales sur la mesure de la concentration d'EDX As dans l'échantillon à 10% sont montrés dans la figure 3.12.

Afin de vérifier la validité de notre procédure et l'applicabilité de ces coefficients à la distribution d'arsenic avec des concentrations plus faibles, nous avons utilisé les valeurs précédemment obtenues des coefficients de C-L pour mesurer la concentration de dopage dans l'échantillon a-SiAs 2%. Les résultats sont montrés sur la figure 3.13 où les erreurs expérimentales sur les mesures EDX sont également visibles.

Tout d'abord, il faut noter que l'erreur expérimentale est plus grande pour des concentrations plus élevées. Cela est dû au fait que l'erreur absolue sur l'intensité mesurée augmente avec l'intensité alors que l'erreur relative diminue. L'erreur sur la concentration de dopage suit la même tendance puisqu'elle dépend directement de l'erreur sur l'intensité. Cela signifie que, dans le pic de distribution de dopage, la valeur mesurée

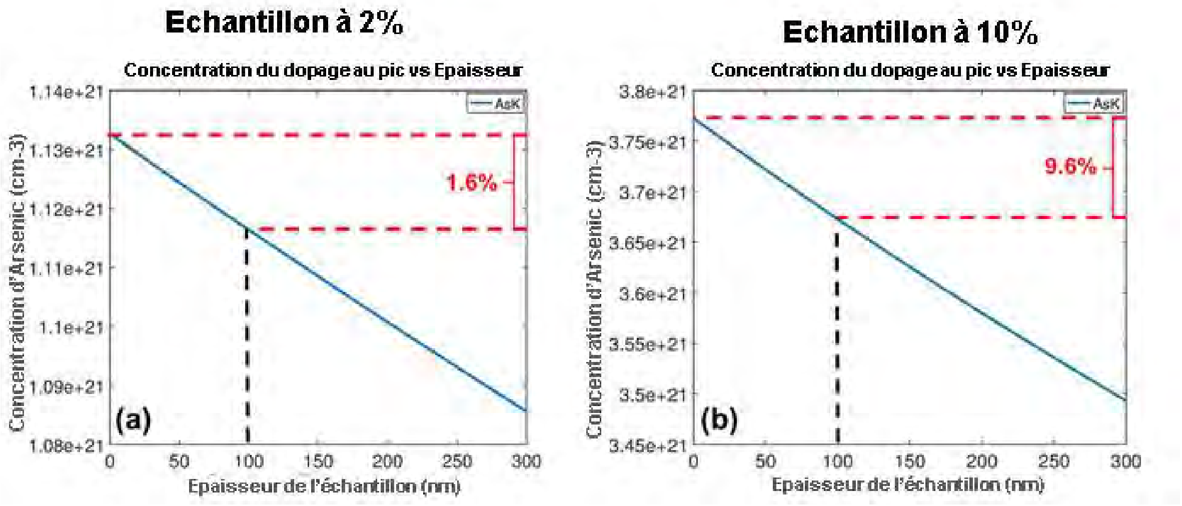

FIGURE 3.11: Variation de la densité de pic corrigée par l'absorption dans les échantillons à 2% (a) et 10% (b). La concentration a été obtenue en utilisant les familles AsK et SiK.

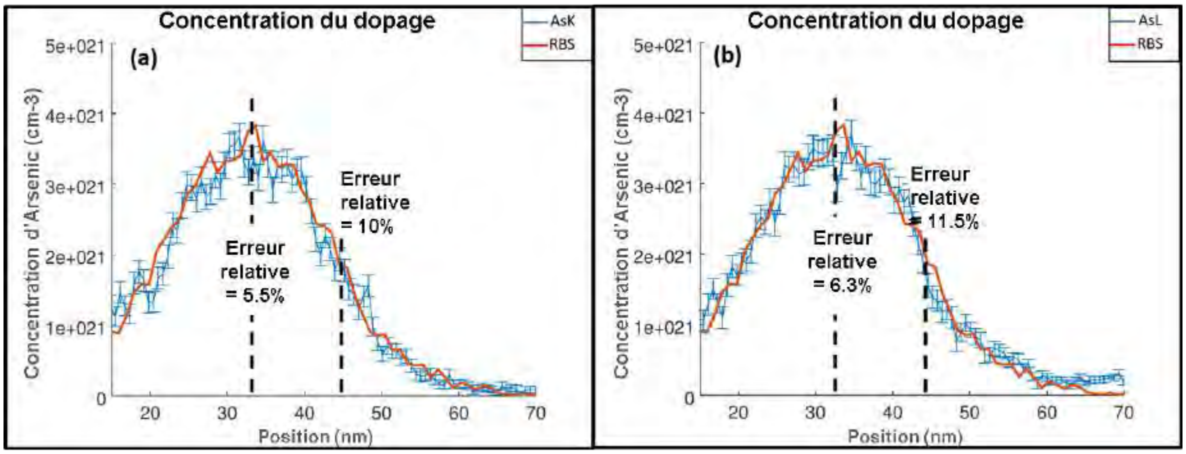

FIGURE 3.12: Concentration atomique de As ($\widetilde{c}^{A}_{As}(x)$) mesurée en utilisant les pics K pour les Si et le as As (a) et les pics K le Si et les pics L pour le As (b). Dans les deux cas, les valeurs obtenues sont comparées aux valeurs obtenues par RBS.

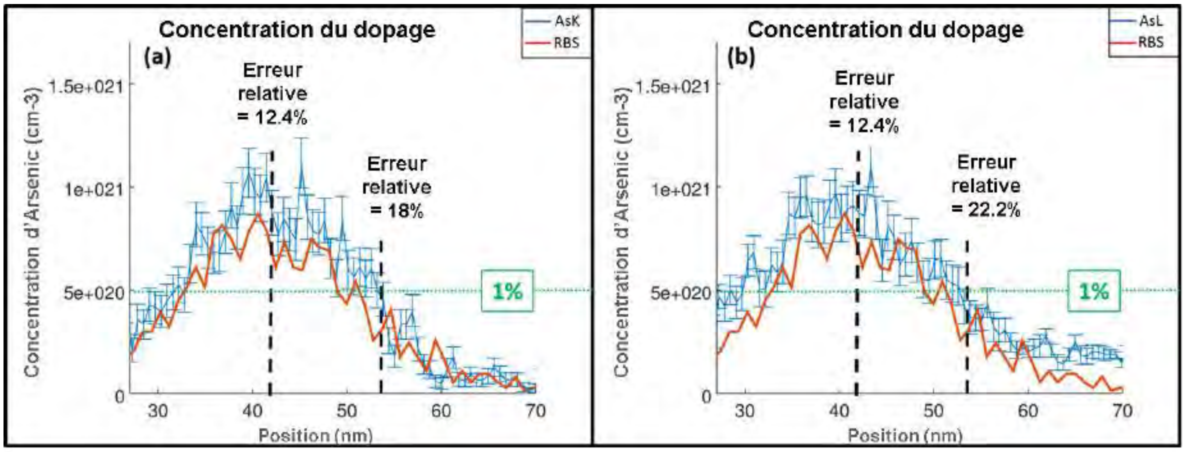

FIGURE 3.13: Concentration atomique de As ($\widetilde{c}^{A}_{As}(x)$) mesurée en utilisant les pics K pour les Si et le as As (a) et les pics K le Si et les pics L pour le As (b). Dans les deux cas, les valeurs obtenues sont comparées aux valeurs obtenues par RBS.

de la concentration de dopage est plus précise (c'est-à-dire qu'elle a une erreur relative plus basse) que les valeurs dans la queue de la distribution, même si des barres d'erreur plus grandes apparaissent sur le graphique.

La figure 3.13 montre clairement que les résultats obtenus avec les pics K d'arsenic sont plus fiables que ceux obtenus avec les pics L. Ceci est encore plus évident pour les faibles concentrations (c'est-à-dire dans la queue à droite du profil de dopage).

Nous pensons que cette différence peut est dûe à un manque de précision dans la mesure de l'intensité des pics L de l'arsenic. Cela est dû à la position des pics L, situés dans la région de basse énergie du spectre. Dans cette région, la soustraction du bruit de Bremsstrahlung est plus difficile car le bruit est plus élevé. De plus, il existe des pics voisins associés à l'oxygène et au carbone. Pour les concentrations faibles, telles que celles que nous mesurons, ce type de problème devient critique car les intensités maximales et le Bremsstrahlung peuvent être du même ordre de grandeur. Cela signifie qu'une petite erreur sur l'interpolation du bruit de fond a un impact important sur la mesure de la concentration en As. Nous avons donc décidé d'utiliser les pics d'arsenic K pour toutes les mesures suivantes.

3.3.2 Mesure du profil dopant

Pour vérifier l'applicabilité de notre méthode à de nano-dispositifs nous avons effectué des mesures sur le dispositif FinFET déjà décrit dans la section 3.1.1. Pour cela, une cartographie d'intensité EDX a été mesurée (voir figure 3.14).

Afin de pouvoir appliquer la même géométrie de mesure illustrée sur la figure 2.2 du chapitre 2 , nous avons décidé d'étudier la distribution de l'une des parois verticales du FinFET. Les échantillons ont été orientés pour l'acquisition comme dans la figure 3.15(a). Notre méthode de quantification a ensuite été appliquée aux profils de pics de

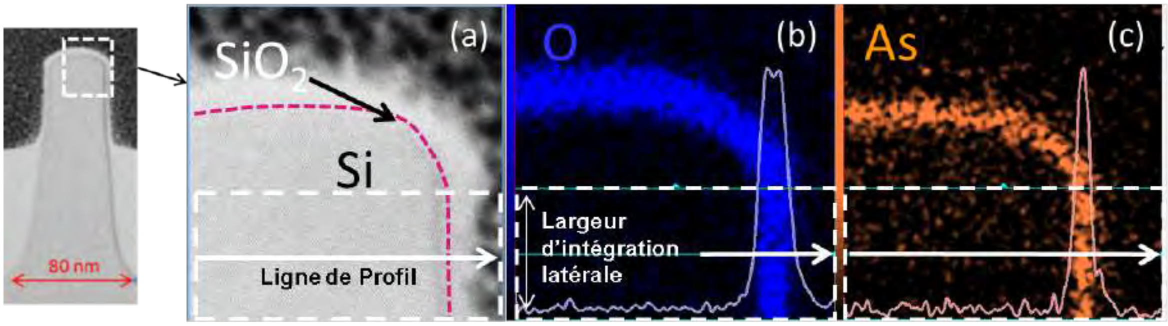

FIGURE 3.14: Images STEM à champ clair (a) et cartographie d'intensité EDX (b-c) obtenues sur la structure de test FinFET. Les pics K ont été utilisés à la fois pour l'oxygène et pour l'arsenic afin d'obtenir les profiles d' intensité montrés en (b) et (c). Les profils d'intensités obtenus par intégration latérale sont superposés aux cartes ((b) et (c)). Les flèches en (a), (b) et (c) indiquent la direction et la position de la direction d'intégration ainsi que la largeur d'intégration latérale.

silicium et d'arsenic. Le résultat final est présenté à la figure 3.15(b) où le profil de dopage sur la paroi latérale et les erreurs correspondantes sont indiqués.

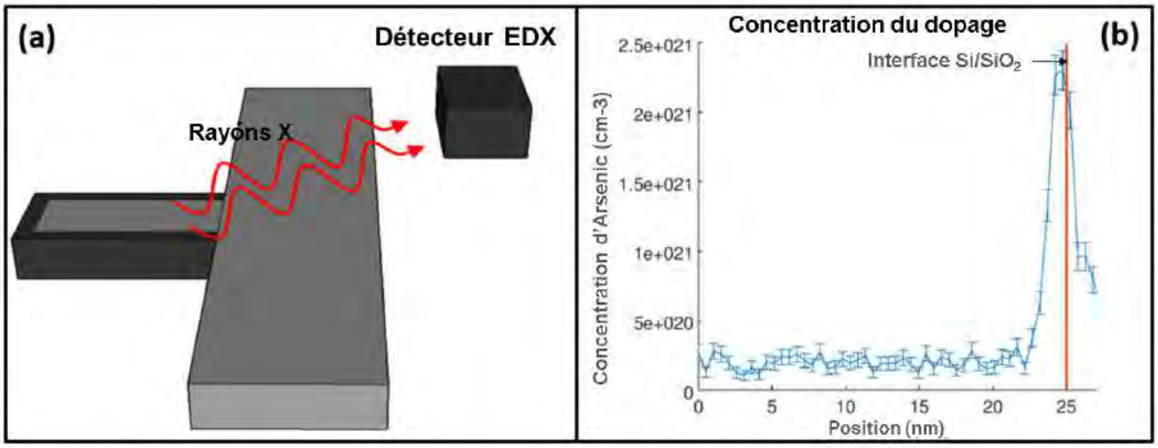

FIGURE 3.15: (a) Image schématique illustrant la géométrie utilisée pour obtenir le profil de dopage et (b) profil de dopage avec erreur expérimentale obtenue en appliquant la méthode de quantification décrite dans le chapitre 2.

Les résultats montrent clairement qu'un profil de dopage peut être obtenu dans un nanodispositif avec cette technique, et que l'erreur expérimentale obtenue est suffisamment faible pour permettre d'apprécier les variations de concentration dans le profil.

3.4 Limite de Détection

Il est intéressant, dans le contexte du profil de dopage de STEM / EDX, d'essayer de comprendre quelle est la limite de détection de la concentration en arsenic dans un nano-dispositif. Pour estimer la plus faible concentration en arsenic mesurable, nous avons utilisé une approche simple basée sur les résultats expérimentaux. Il est facile de comprendre qu'une mesure de densité ne peut pas être distinguée de zéro si l'intervalle de confiance (c'est-à-dire l'intervalle qui se situe entre $c - \Delta c$ et $c + \Delta c$) inclut le zéro. Le résultat obtenu dépend évidemment de intervalle de confiance choisi [42].

L'analyse des profils montrés sur la figure 3.15 montre clairement que la concentration de dopage est toujours supérieure à la limite de détection. Pour obtenir la limite de détection on s'est donc servi des résultats obtenus sur les échantillons de calibration (voir figure3.13 (b)) qui nous ont permis de mesurer une limite de détection de $7.7\,10^{19} cm^{-3}$.

Bien évidemment, la valeur obtenue ne représente pas une estimation absolue, car la valeur de la limite de détection dépend de l'intensité des pics (voir l'équation 2.29 et 2.30) et peut être améliorée en augmentant le temps d'exposition utilisé pour la mesure. Les formules dérivée dans cette thèse, peuvent, d'ailleurs, être utilisées pour calculer l'erreur associée à un temps d'exposition spécifique, mais il est impossible de déduire une limite théorique minimale car le temps d'exposition maximal dépend de nombreux facteurs expérimentaux tels que la stabilité de l'échantillon à la dérive et de sa résistance à l'irradiation électronique.

Pourtant, le temps nécessaire pour obtenir une valeur d'intensité cible peut être estimé. Pour donner un exemple de cette procédure, nous avons estimé les temps d'exposition nécessaires pour obtenir une limite de détection donnée à l'aide des paramètres spécifiques de notre configuration expérimentale. Plus précisément, nous avons utilisé les valeurs du nombre de coups par seconde mesurées dans notre configuration pour calculer le temps de mesure nécessaire pour obtenir différentes valeurs de la limite de détection. Pour les calculs, nous avons supposé que la valeur des comptes par seconde ne changeait pas avec le temps.

En partant de l'équation 2.2, en utilisant l'équation2.31 et 2.34 et en considérant que l'erreur sur l'épaisseur est négligeable et que le pic As a une intensité négligeable par rapport au pic Si nous nous pouvons obtenir la formule suivante :

$$I_{Si:F_{Si}} = \frac{\frac{k_{As:F_{As},F_{Si}} * \widetilde{f}^M_{As}\left(1-\widetilde{f}^M_{As}\right)}{\widetilde{f}^M_{As}(x)} + 1}{\left(\frac{\frac{\Delta\widetilde{c}^A_{As} m_{As}}{N_{AV}\left\{\widetilde{\rho}^M_{a-SiAs} + \widetilde{f}^M_{As}(x)\frac{\widetilde{\rho}^M_{a-Si}\eta}{\left[1-\eta\widetilde{f}^M_{As}\right]^2}\right\}}}{\widetilde{f}^M_{As}\left(1-\widetilde{f}^M_{As}\right)}\right)^2 - \left(\frac{\Delta\widetilde{f}^M_{As}}{k_{As:F_{As},F_{Si}}}\right)^2} \tag{3.1}$$

Cette formule exprime l'intensité$I_{Si:F_{Si}}(x)$ du pic de Si à obtenir si nous voulons obtenir la valeur suivante pour la densité As $\widetilde{f}^M_{As} \pm \Delta\widetilde{f}^M_{As}$. Selon notre définition de la limite de détection, on peut alors obtenir l'intensité I_D nécessaire pour obtenir une limite de détection D en imposant que $\Delta\widetilde{f}^M_{As} = \widetilde{f}^M_{As} = D$ dans l'équation 3.1

Le temps d'exposition nécessaire pour obtenir une intensité mesurée I_D peut être estimé en utilisant les coups par seconde (cps) de la manière suivante (on a aussi supposé que $I_{Si:F_{Si}} = 0$ pour $t_{exp} = 0$) :

$$t_{exp} = \frac{I_{Si:F_{Si}}(x)}{cps} \tag{3.2}$$

Le temps de mesure nécessaire pour obtenir une limite de détection spécifique, peut ainsi être calculé. Les résultats sont présentés dans le tableau 3.1. On peut clairement constater que, dans notre cas, il est difficile d'améliorer considérablement la limite de détection en augmentant simplement les temps de mesure, puisque la présence de la dérive de l'échantillon, des dommages causés par le faisceau et de l'instabilité du courant (dans notre cas, le microscope est équipé avec un canon à émission de champ à froid) limitent le temps de mesure à quelques dizaines de minutes.

Limite de détection de la densité d'As	**Temps d'exposition (temps réel)**
$1\,10^{19} cm^{-3}$	51 minutes
$5\,10^{18} cm^{-3}$	1 heure et 43 minutes
$1\,10^{18} cm^{-3}$	8 heures et 55 minutes

Table 3.1: Temps de mesure estimé nécessaire pour obtenir des limites de détection plus élevées

Remerciements

Je tiens en premier lieu à exprimer ma profonde reconnaissance aux membres du jury pour l'honneur qu'ils m'ont fait en acceptant de juger ce travail : La Présidente, Madame le Docteur Caroline BONAFOS, les rapporteurs, Madame le Docteur Marie-France BEAUFORT, Monsieur le Docteur Alain PORTAVOCE et l'examinateur Monsieur le Docteur Etienne TALBOT.

C'est un véritable plaisir pour moi de pouvoir remercier ici toutes les personnes dont la présence m'a été si précieuse durant ces 5 années d'études en France, même si de simples mots ne suffiront jamais pour exprimer mon immense reconnaissance. Je tiens donc à remercier Monsieur le Professeur Marc RESPAUD. Marc je te remercie pour m'avoir accueilli dans ton équipe, pour le réel intérêt que tu as manifesté pour ce projet au cours de ces trois années, pour tes conseils scientifiques et surtout de m'avoir gentiment pousser pour mieux avancer quand il a fallu le faire.

J'adresse mes plus profonds REMERCIEMENTS à Monsieur le Docteur Pier-Francesco FAZZINI pour m'avoir « plus-que » parfaitement encadré pendant ces 3 ans. Pier je pense que j'ai eu une énorme chance de t'avoir comme encadrant. Je te remercie pour ton optimisme, pour ta disponibilité, pour ton accompagnement au cours de chaque étape de la thèse. Sans toi je n'aurais jamais pu arriver jusqu'au bout ! Je te souhaite une excellente suite autant au plan professionnel qu'au plan familial.

J'adresse aussi mes profonds remerciements à Monsieur le Docteur Fuccio CRISTIANO pour m'avoir encadré pendant ces 3 ans. Je te remercie pour la grande base de connaissance scientifique que tu étais toujours prêt de me la transmettre. Comme Pier, tu m'as appris ce que je sais faire aujourd'hui. Tu étais toujours présent pour me donner autant de la connaissance scientifique que de la motivation et des conseils pour tous les jours. J'ai eu vraiment de la chance de t'avoir comme encadrant. Je te souhaite aussi une excellente suite autant au plan professionnel qu'au plan familial.

Je voudrais exprimer toute ma gratitude et surtout toute mon estime pour les différents membres de l'équipe pour le soutien morale, surtout lors de la rédaction de ce manuscrit.

Je tiens à remercier aussi l'ensemble des membres des plateformes « Castaing » et l' « AIME » pour l'accueil. Merci à Reasmey pour l'accueil et les discussions scientifiques très enrichissantes lors de mon passage au MEB à l'AIME. Armel pour la formation au MET 2100 et tous les conseils scientifiques a Castaing. Tous pleins de merci aussi à tous mes amis du laboratoire pour toutes les discussions motivantes.

Je n'oublierais jamais tous mes anciens profs et encadrants qui m'ont facilité la route et qui étaient derrière ma réussite ! Je remercie spécialement docteur Maher El TAMER de la licence au Liban qui m'a conseillé de continuer mes études supérieures à l'Université Paul Sabatier à Toulouse. Aussi, Docteur Mohamed-Aziz BOUCHENE pour l'encadrement durant le stage du Master 1 ou j'ai fait le premier pas vers la recherche réelle. Et tous les professeurs du Master a Paul Sabatier surtout Docteur Pierre PUJOL, Docteur Timo FLEIG et Docteur Roland CORATGER.

Le début de mon séjour en France n'était pas assez simple mais tout a parfaitement démarré grâce à la générosité de nombreuses personnes qui sont devenues ma deuxième famille « Toulousaine »: Je vous remercie Assem et Rana pour votre accueil chez vous lors de mon arrivé en France et de devoir me supporter une bonne longue durée. Mouin tu étais comme mon grand frère et tu m'a chaleureusement et généreusement pris en charge pour pleines de choses très utiles pour mon séjour et je te suis infiniment reconnaissant. Il n'y a pas de mots suffisants pour décrire à quel point je suis chanceuse de t'avoir comme un ami préféré. Mahmoud merci pour ta gentillesse, ta fidélité et ton amitié. Tu étais toujours présent pour tout le monde et pour moi en particulier. Tu es la personne qui me manque le plus dès son départ. Amar merci pour tous les conseils quelques soit dans la vie professionnelle et privée, tu étais toujours la plus proche de moi à Toulouse. Ali GH tu es la première personne que j'ai rencontré à Toulouse, tu vas toujours rester l'ami fidèle qui prend soin des autres. Bouchra tu vas toujours être l'amie la plus ladin à Toulouse. Hussein merci d'être un grand frère tout le temps et merci pour tous les repas délicieux que tu as préparé. Mariam, merci pour l'effort que tu as fait pour l'amitié avec le groupe.

Je ne veux pas oublier de remercier Alaa, Majida et Nour GH d'être toujours présents pour des conseils et pour des moments inoubliables.

Je remercie de fond de mon cœur l'ensemble de mes amis Alé, Youssef, Wassim, Anwar, Ali Kanso, Dayan, Jana, Younes et Maya pour toutes les belles soirées qu'on a passé. Je ne vais certainement pas oublier de remercier le « couple » le plus apathique dans le monde Mahmoud et Diana : Vous êtes toujours en situation de joie et j'adore passer le temps avec vous et merci d'être toujours présents pour m'aider à prendre soin de Oslo. Rawad et Naim: le temps qu'on a passé ensemble était dans la plupart des cas pour préparer des repas mais ça m'a fait beaucoup de plaisir et merci de pouvoir toujours compter sur vous. Yessine ta personnalité ressemble à celle d'une personne dont j'adore son caractère ce qui te rend l'un de mes préférés. Nadine ton aide et tes coups de mains étaient comme ça venait d'un ange, en toute discrétion et sans aucune hésitation !! Laura et Nadia vous êtes l'exemple parfait d'un couple d'amis dont il faut s'apprendre et j'adore comment vous toujours en situation de rire. Un grand merci à Hassan et Omar, vous êtes jusqu'à maintenant toujours là pour moi, pour me supporter et pour me motiver.

Je laisse le meilleur pour la fin. Ali, tout simplement merci d'être la tout le temps et dans toutes les situations. Tu étais durant toute la durée de la thèse ma motivation et tu m'as toujours poussé à faire le meilleur. Sans toi je ne pouvais pas arriver à avoir un tel résultat. UN GRAND MERCI !!

Je voudrais aussi remercier Anthony, Farid, Rita, Ghazar, Maen, Sami, Soha, Dany, Simona, Chadi et Yolla ». Je vous remercie tous les amis pour votre présence à mes côtés à chaque fois que j'avais besoin de vous. Je ne pourrais pas m'empêcher aussi de remercier des gens qui m'ont longtemps soutenu pour des longues périodes et avec qui j'ai passé de très bons moments : Haifa, tu etais toujours la meilleure. Tu étais toujours présente pour tous les moments les difficiles et les joyeux. Merci pour ta présence tu m'as toujours soutenu du fond de ton cœur. Pareil, Dima, Rim, Rim, Marwa, Rita, Hassan, Marwan, Rashad, Sara, Lama, Lama, Lama ! Malgré toutes les distances qui nous ont séparées vous resterez mes meilleurs amis et toujours très proches !

Et finalement, je voudrais terminer en remerciant les meilleurs et les plus proches, en commençant par mes parents, mes frères (Khaled et Rawad) ma sœur (Khouloud) et ma belle-sœur (Tamara), mes cousins et cousines. Je vous remercie tous d'être toujours source de sécurité et de stabilité, ce que je ressens envers chacun d'entre vous est juste indescriptible mais je pourrais juste vous dire que je vous dois tout l'amour que vous m'avait généreusement donné, et toutes les valeurs que j'ai appris grâce à vous! Et comme chaque fin les meilleurs pour la fin : Merci à mes deux adorables papa et maman et à mes frères et sœur d'avoir sacrifié leurs vies pour le bien être de la plus belle des familles. Ma vie sans vous n'a ni de sens ni de goût !! MERCI pour TOUT car sans VOUS, je n'aurais jamais pu arriver jusqu'au BOUT !

Bibliography

[1] Nicholas W. M. Ritchie, Dale E. Newbury, and Jeffrey M. Davis. EDS measurements of X-ray intensity at WDS precision and accuracy using a silicon drift detector. *Microscopy and Microanalysis: The Official Journal of Microscopy Society of America, Microbeam Analysis Society, Microscopical Society of Canada*, 18(4):892–904, August 2012.

[2] G. Kothleitner, M. J. Neish, N. R. Lugg, S. D. Findlay, W. Grogger, F. Hofer, and L. J. Allen. Quantitative Elemental Mapping at Atomic Resolution Using X-Ray Spectroscopy. *Physical Review Letters*, 112(8):085501, February 2014.

[3] David B. Williams and C. Barry Carter. *Transmission Electron Microscopy: A Textbook for Materials Science*. Springer Science & Business Media, August 2009.

[4] M. Lentzen. The refractive index in electron microscopy and the errors of its approximations. *Ultramicroscopy*, 176:139–145, May 2017.

[5] Louis de Broglie. Recherches sur la théorie des Quanta. November 1924.

[6] H. Seiler. Secondary electron emission in the scanning electron microscope. *Journal of Applied Physics*, 54:R1–R18, November 1983.

[7] Joseph I. Goldstein, Dale E. Newbury, Joseph R. Michael, Nicholas W. M. Ritchie, John Henry J. Scott, and David C. Joy. *Scanning Electron Microscopy and X-Ray Microanalysis*. Springer-Verlag, New York, 4 edition, 2018.

[8] R. F. Egerton. *Electron Energy-Loss Spectroscopy in the Electron Microscope*. Springer Science & Business Media, March 2013.

[9] Brent Fultz and James Howe. *Transmission Electron Microscopy and Diffractometry of Materials*. January 2002.

[10] W. T. Cochran, J. W. Cooley, D. L. Favin, H. D. Helms, R. A. Kaenel, W. W. Lang, G. C. Maling, D. E. Nelson, C. M. Rader, and P. D. Welch. What is the fast Fourier transform? *Proceedings of the IEEE*, 55(10):1664–1674, October 1967.

[11] Peter D. Nellist. The Principles of STEM Imaging. In Stephen J. Pennycook and Peter D. Nellist, editors, *Scanning Transmission Electron Microscopy: Imaging and Analysis*, pages 91–115. Springer New York, New York, NY, 2011.

[12] Curt Suplee. X-Ray Transition Energies Database, July 2009.

[13] Charles G. Barkla M. Sc B.A. LXXV. Secondary radiation from gases subject to X-rays. *The London, Edinburgh, and Dublin Philosophical Magazine and Journal of Science*, 5(30):685–698, June 1903.

[14] Jorge Trincavelli, Silvina Limandri, and Rita Bonetto. Standardless quantification methods in electron probe microanalysis. *Spectrochimica Acta Part B: Atomic Spectroscopy*, 101:76–85, November 2014.

[15] H. C. Manjunatha, B. M. Chandrika, B. Rudraswamy, and B. M. Sankarshan. Beta Bremsstrahlung dose in concrete shielding. *Nuclear Instruments and Methods in Physics Research Section A: Accelerators, Spectrometers, Detectors and Associated Equipment*, 674:74–78, May 2012.

[16] P. van Espen, H. Nullens, and F. Adams. A computer analysis of X-ray fluorescence spectra. *Nuclear Instruments and Methods*, 142(1-2):243–250, April 1977.

[17] Jorge Trincavelli, Gustavo Castellano, and J. Alberto Riveros. Model for the bremsstrahlung spectrum in EPMA. Application to standardless quantification. *X-Ray Spectrometry*, 27(2):81–86, 1998.

[18] Catalina Curceanu, Aidin Amirkhani, Ata Baniahmad, Massimiliano Bazzi, Giovanni Bellotti, Carolina Berucci, Damir Bosnar, Mario Bragadireanu, Michael Cargnelli, Alberto Clozza, R. Grande, Carlo Fiorini, F. Ghio, Carlo Guaraldo, Mihail Iliescu, Masaiko Iwasaki, P. Levi Sandri, Johann Marton, Marco Miliucci, and Johann Zmeskal. X-ray Detectors for Kaonic Atoms Research at DAΦNE. *Condensed Matter*, 4:42, April 2019.

[19] Ulrich Gernert. Comparing the Si(Li)-detector and the silicon drift detector (SDD) using EDX in SEM. January 2008.

[20] Andreas Garmannslund. Refinement of the ζ-factor Method for Quantitative Energy-Dispersive X-ray Spectroscopy in Scanning Transmission Electron Microscopy. *103*, 2016.

[21] M. Watanabe and D. B. Williams. The quantitative analysis of thin specimens: a review of progress from the Cliff-Lorimer to the new ζ-factor methods. *Journal of Microscopy*, 221(2):89–109, 2006.

[22] Katherine E. MacArthur, Thomas J. A. Slater, Sarah J. Haigh, Dogan Ozkaya, Peter D. Nellist, and Sergio Lozano-Perez. Quantitative Energy-Dispersive X-Ray Analysis of Catalyst Nanoparticles Using a Partial Cross Section Approach. *Microscopy and Microanalysis*, 22(1):71–81, February 2016.

[23] F. Eggert. Automated element identification for EDS spectra evaluation using quantification and integrated spectra simulation approaches. *IOP Conference Series: Materials Science and Engineering*, 7(1):012007, 2010.

[24] Dale E. Newbury. Mistakes encountered during automatic peak identification of minor and trace constituents in electron-excited energy dispersive X-ray microanalysis. *Scanning*, 31(3):91–101, May 2009.

[25] E. Lifshin. 1973.

[26] N. G. Ware and S. J. B. Reed. Background corrections for quantitative electron microprobe analysis using a lithium drifted silicon X-ray detector. *Journal of Physics E: Scientific Instruments*, 6(3):286, 1973.

[27] John A. Small, Stefan D. Leigh, Dale E. Newbury, and Robert L. Myklebust. Modeling of the bremsstrahlung radiation produced in pure-element targets by 10–40 keV electrons. *Journal of Applied Physics*, 61(2):459–469, January 1987.

[28] Curt Suplee. XCOM: Photon Cross Sections Database, September 2009.

[29] F. Eggert and W. Scholz. A rapid deconvolution method based on the Bayes theorem applied to energy dispersive X-ray emission analysis - improvements and error influences. *physica status solidi (a)*, 97(1):K9–K13, 1986.

[30] David Rossouw, Pierre Burdet, Francisco de la Peña, Caterina Ducati, Benjamin R. Knappett, Andrew E. H. Wheatley, and Paul A. Midgley. Multicomponent Signal Unmixing from Nanoheterostructures: Overcoming the Traditional Challenges of Nanoscale X-ray Analysis via Machine Learning. *Nano Letters*, 15(4):2716–2720, April 2015.

[31] Fred Stevie. *Secondary Ion Mass Spectrometry: Applications for Depth Profiling and Surface Characterization*. Momentum Press, September 2015.

[32] Wei-Kan Chu. *Backscattering Spectrometry, Wei-Kan Chu, James W. Mayer, and Marc-A. Nicolet, Academic Press, 1978*. January 1978.

[33] Atom Probe Tomography - 1st Edition.

[34] O. Eibl. New method for absorption correction in high-accuracy, quantitative EDX microanalysis in the TEM including low-energy x-ray lines. *Ultramicroscopy*, 50(2):179–188, July 1993.

[35] J. H. Hubbell and S.M. Seltzer. Tables of X-Ray Mass Attenuation Coefficients and Mass Energy-Absorption Coefficients. 2014.

[36] C. T. Chantler. Atomic form factors and photoelectric absorption cross-sections near absorption edges in the soft X-ray region. *AIP Conference Proceedings*, 652(1):370–377, January 2003.

[37] K. F. J. Heinrich. Mass absorption coefficients for electron probe microanalysis. *Proc. 11th Int. Congr. on X-Ray Optics and Microanalysis*, pages 67–119, 1986.

[38] Zbigniew Stachurski. *Fundamentals of Amorphous Solids: Structure and Properties.* 2015.

[39] L. Vegard. Die Konstitution der Mischkristalle und die Raumfüllung der Atome. *Zeitschrift für Physik*, 5(1):17–26, January 1921.

[40] E. Kasper, A. Schuh, G. Bauer, B. Holländer, and H. Kibbel. Test of Vegard's law in thin epitaxial SiGe layers. *Journal of Crystal Growth*, 157(1):68–72, December 1995.

[41] Larry Wasserman. *All of Nonparametric Statistics.* Springer Texts in Statistics. Springer-Verlag, New York, 2006.

[42] John R. Taylor. *Introduction To Error Analysis: The Study of Uncertainties in Physical Measurements.* University Science Books, July 1997. Google-Books-ID: giFQcZub80oC.

[43] P L Morris, M Ball, and P Statham. In *EMAG'79 Brighton.UK*, volume 52 of *Inst. Phys. Conf. Ser.*, page 413.

[44] Y. Qiu, V. H. Nguyen, A. Dobbie, M. Myronov, and T. Walther. Calibration of thickness-dependentk-factors for germanium X-ray lines to improve energy-dispersive X-ray spectroscopy of SiGe layers in analytical transmission electron microscopy. *Journal of Physics: Conference Series*, 471:012031, November 2013. Publisher: IOP Publishing.

[45] J.-P. Colinge, editor. *FinFETs and Other Multi-Gate Transistors.* Integrated Circuits and Systems. Springer US, 2008.

[46] James F. Ziegler and Jochen P. Biersack. The Stopping and Range of Ions in Matter. In D. Allan Bromley, editor, *Treatise on Heavy-Ion Science: Volume 6: Astrophysics, Chemistry, and Condensed Matter*, pages 93–129. Springer US, Boston, MA, 1985.

[47] Xiaoxing Ke, Sara Bals, Ainhoa Romo Negreira, Thomas Hantschel, Hugo Bender, and Gustaaf Van Tendeloo. TEM sample preparation by FIB for carbon nanotube interconnects. *Ultramicroscopy*, 109(11):1353–1359, October 2009.

[48] G. N. Greaves, S. R. Elliott, and E. A. Davis. Amorphous arsenic. *Advances in Physics*, 28(1):49–141, February 1979.

[49] J. S. Custer, Michael O. Thompson, D. C. Jacobson, J. M. Poate, S. Roorda, W. C. Sinke, and F. Spaepen. Density of amorphous Si. *Applied Physics Letters*, 64(4):437–439, 1994.

[50] Els Parton and Peter Verheyen. Strained silicon — the key to sub-45 nm CMOS. *III-Vs Review*, 19(3):28–31, April 2006.

[51] Maryam Shayesteh, Dan O' Connell, Farzan Gity, Philip Murphy-Armando, Ran Yu, Karim Huet, Ines Toqué-Tresonne, Fuccio Cristiano, Simona Boninelli, Henrik Hartmann Henrichsen, Peter Folmer Nielsen, Dirch Hjorth Petersen, and Ray Duffy. Optimized Laser Thermal Annealing on Germanium for High Dopant Activation and Low Leakage Current. *I E E E Transactions on Electron Devices*, 61(12):4047–4055, 2014.

[52] Biljana L. Risteska Stojkoska and Kire V. Trivodaliev. A review of Internet of Things for smart home: Challenges and solutions. *Journal of Cleaner Production*, 140:1454–1464, January 2017.

[53] Christophe Lethien, Jean Le Bideau, and Thierry Brousse. Challenges and prospects of 3d micro-supercapacitors for powering the internet of things. *Energy & Environmental Science*, 12(1):96–115, January 2019.

[54] A. Chana, Daniel Estèvea, Jean-Yves Fourniolsa, Christophe Escribaa, and Eric Campoa. mart wearable systems : Current status and future challenges. 2012.

[55] John R. Miller. Valuing Reversible Energy Storage. *Science*, 335(6074):1312–1313, March 2012.

[56] Jimin Maeng, Chuizhou Meng, and Pedro Irazoqui. Wafer-scale integrated micro-supercapacitors on an ultrathin and highly flexible biomedical platform. *Biomedical Microdevices*, 17, February 2015.

[57] Patrice Simon and Yury Gogotsi. Materials for electrochemical capacitors. In *Nanoscience and Technology*, pages 320–329. Co-Published with Macmillan Publishers Ltd, UK, August 2009.

[58] Kristy Jost, Genevieve Dion, and Yury Gogotsi. Textile energy storage in perspective. *Journal of Materials Chemistry A*, 2(28):10776–10787, June 2014.

[59] Wei Liu, Min-Sang Song, Biao Kong, and Yi Cui. Flexible and Stretchable Energy Storage: Recent Advances and Future Perspectives. *Advanced Materials*, 29(1):1603436, 2017.

[60] Kristy Jost, Carlos R. Perez, John K. McDonough, Volker Presser, Min Heon, Genevieve Dion, and Yury Gogotsi. Carbon coated textiles for flexible energy storage. *Energy & Environmental Science*, 4(12):5060–5067, November 2011.

[61] Huihui Zhang, Yan Qiao, and Zhisong Lu. Fully Printed Ultraflexible Supercapacitor Supported by a Single-Textile Substrate. *ACS Applied Materials & Interfaces*, 8(47):32317–32323, November 2016.

[62] Chuanfang (John) Zhang, Matthias P. Kremer, Andrés Seral-Ascaso, Sang-Hoon Park, Niall McEvoy, Babak Anasori, Yury Gogotsi, and Valeria Nicolosi. Stamping of Flexible, Coplanar Micro-Supercapacitors Using MXene Inks. *Advanced Functional Materials*, 28(9):1705506, 2018.

[63] Wenping Si, Chenglin Yan, Yao Chen, Steffen Oswald, Luyang Han, and Oliver G. Schmidt. On chip, all solid-state and flexible micro-supercapacitors with high performance based on MnOx/Au multilayers. *Energy & Environmental Science*, 6(11):3218–3223, October 2013.

[64] Xingyou Lang, Akihiko Hirata, Takeshi Fujita, and Mingwei Chen. Nanoporous metal/oxide hybrid electrodes for electrochemical supercapacitors. *Nature Nanotechnology*, 6(4):232–236, April 2011.

[65] J. M. Sieben, E. Morallón, and D. Cazorla-Amorós. Flexible ruthenium oxide-activated carbon cloth composites prepared by simple electrodeposition methods. *Energy*, 58(C):519–526, 2013.

[66] Chuizhou Meng, Jimin Maeng, Simon W. M. John, and Pedro P. Irazoqui. Ultrasmall Integrated 3d Micro-Supercapacitors Solve Energy Storage for Miniature Devices. *Advanced Energy Materials*, 4(7):1301269, 2014.

[67] Craig B. Arnold, Ryan C. Wartena, Karen Swider-Lyons, and Alberto Pique. Direct-Write Planar Microultracapacitors by Laser Engineering. *Journal of The Electrochemical Society - J ELECTROCHEM SOC*, 150, May 2003.

[68] Maher F. El-Kady, Veronica Strong, Sergey Dubin, and Richard B. Kaner. Laser scribing of high-performance and flexible graphene-based electrochemical capacitors. *Science (New York, N.Y.)*, 335(6074):1326–1330, March 2012.

[69] Jian Lin, Zhiwei Peng, Yuanyue Liu, Francisco Ruiz-Zepeda, Ruquan Ye, Errol L. G. Samuel, Miguel Jose Yacaman, Boris I. Yakobson, and James M. Tour. Laser-induced porous graphene films from commercial polymers. *Nature Communications*, 5:5714, December 2014.

[70] Zhiwei Peng, Ruquan Ye, Jason A. Mann, Dante Zakhidov, Yilun Li, Preston R. Smalley, Jian Lin, and James M. Tour. Flexible Boron-Doped Laser-Induced Graphene Microsupercapacitors. *ACS Nano*, 9(6):5868–5875, June 2015.

[71] Zhiwei Peng, Jian Lin, Ruquan Ye, Errol L. G. Samuel, and James M. Tour. Flexible and Stackable Laser-Induced Graphene Supercapacitors. *ACS Applied Materials & Interfaces*, 7(5):3414–3419, February 2015.

[72] O. Barbieri, M. Hahn, A. Foelske, and R. Kötz. Effect of Electronic Resistance and Water Content on the Performance of RuO2 for Supercapacitors. *Journal of The Electrochemical Society*, 153(11):A2049–A2054, January 2006.

[73] Ty Mai Dinh, Amine Achour, Sorin Vizireanu, Gheorghe Dinescu, Leona Nistor, Kevin Armstrong, Daniel Guay, and David Pech. Hydrous RuO 2 /carbon nanowalls hierarchical structures for all-solid-state ultrahigh-energy-density micro-supercapacitors. *Nano Energy*, 10:288–294, November 2014.

[74] Jee Y. Hwang, Maher F. El-Kady, Yue Wang, Lisa Wang, Yuanlong Shao, Kristofer Marsh, Jang M. Ko, and Richard B. Kaner. Direct preparation and processing of graphene/RuO2 nanocomposite electrodes for high-performance capacitive energy storage. *Nano Energy*, 18:57–70.

[75] G. Larrieu and X.-L. Han. Vertical nanowire array-based field effect transistors for ultimate scaling. *Nanoscale*, 5(6):2437–2441, March 2013.

[76] P. Gas and F. M. d'Heurle. Formation of silicide thin films by solid state reaction. *Applied Surface Science*, 73:153–161, November 1993.

[77] Yu Chen, Yung-Chen Lin, Xing Zhong, Hung-Chieh Cheng, Xiangfeng Duan, and Yu Huang. Kinetic Manipulation of Silicide Phase Formation in Si Nanowire Templates. *Nano Letters*, 13(8):3703–3708, August 2013.

[78] Yung-Chen Lin, Kuo-Chang Lu, Wen-Wei Wu, Jingwei Bai, Lih J. Chen, K. N. Tu, and Yu Huang. Single Crystalline PtSi Nanowires, PtSi/Si/PtSi Nanowire Heterostructures, and Nanodevices. *Nano Letters*, 8(3):913–918, March 2008.

[79] Bangzhi Liu, Yanfeng Wang, Sarah Dilts, Theresa S. Mayer, and Suzanne E. Mohney. Silicidation of Silicon Nanowires by Platinum. *Nano Letters*, 7(3):818–824, March 2007.

[80] Xiang-Lei Han. *Réalisation et caractérisation de dispositifs MOSFET nanométriques à base de réseaux denses de nanofils verticaux en silicium.* PhD thesis, Ecole doctorale Micro et Nano Technologies, Acoustique et Télécommunications, Université de Lille 1, January 2011.

[81] W. a. P. Nicholson. Electron beam current measurement in the electron microscope. *Journal of Microscopy*, 121(2):141–147, 1981.

List of Figures

Abstract One of the key issues for the miniaturization of semiconductor nanodevices is the precise control of their doping. In new generation devices, the doping spatial distribution must be controlled with a precision higher than 1nm while atomic concentrations below 1% have to be measured. This calls for the use of high resolution techniques. Scanning transmission electron microscopy (STEM) associated with Energy Dispersive X-ray spectroscopy (EDX) is an excellent candidate due to its versatility (almost all elements of the periodic table canbe mapped) and its high spatial resolution. On the other hand, quantitative analysis of doping by STEM/EDX is complicated by the presence of measurement artifacts that can safely be ignored for high concentrations impurities but become critical for low concentration impurities. In this thesis a modified Cliff-Lorimer (C-L) method has been developed to obtain quantitative dopant profiling in a nanoscale device structure. The method has been applied on specimens prepared by Focused Ion Beam, in order to reduce the influence of secondary X-rays produced by fluorescence or back scattered electrons, and is based on the iterative correction of X-rays absorption effects in the specimen. In order to obtain reliable results the C-L coefficients have been calibrated using Rutherford Back Scattering (RBS) measurement and the total experimental error has been calculated using standard error propagation techniques. The results obtained on a FinFET test structure and on a laser annealed SiGe substrate show the applicability of this technique to devices on the nanometer scale and with low concentration impurities.

Résumé L'un des problèmes clés pour la miniaturisation des nanodispositifs à semi - conducteurs est le contrôle précis de leur dopage. Dans les dispositifs de nouvelle génération, la distribution spatiale du dopage doit être contrôlée avec une précision supérieure à 1 nm, tandis que les concentrations atomiques inférieures à 1% doivent être mesurées. Cela nécessite l'utilisation de techniques de haute résolution. La microscopie électronique à balayage en transmission (STEM) associée à la spectroscopie par rayons X à dispersion d'énergie (EDX) est un excellent candidat en raison de sa polyvalence (presque tous les éléments du tableau périodique peuvent être cartographiés) et de sa haute résolution spatiale. D'autre part, l'analyse quantitative du dopage par STEM/EDX est compliquée par la présence d'artefacts de mesure qui peuvent être ignorés sans risque pour les impuretés à haute concentration, mais deviennent critiques pour les impuretés à faible concentration.Dans cette thèse, une nouvelle méthode basée sur la méthode de de Cliff-Lorimer(C-L) a été développée pour la mesure quantitative de la distribution de dopant dans un dispositif à l'échelle nanométrique. La méthode a été appliquée sur des échantillons préparés par faisceau ionique focalisé, afin de réduire l'influence des rayons X secondaires produits par fluorescence ou par électrons rétrodiffusés, et est basée sur la correction itérative des effets d'absorption des rayons X dans l'échantillon. Afin d'obtenir des résultats fiables, les coefficients de C-L ont été étalonnés à l'aide de la mesure de Rutherford Back Scattering (RBS) et l'erreur expérimentale totale a été calculée à l'aide de techniques de propagation d'erreur standard. Les résultats obtenus sur une structure de test FinFET et sur un substrat de SiGe ayant subi des recuits laser montrent l'applicabilité de cette technique aux dispositifs à l'échelle nanométrique et avec des impuretés à faible concentration.